# Fluid-structure interaction problems in linear and nonlinear engineering applications: theory and experiments

Department of Mechanics, Mathematics and Management

MECHANICAL AND MANAGEMENT ENGINEERING
Ph.D. Program

SSD: ING-IND/13-APPLIED MECHANICS

**Final Dissertation**

---

# "Fluid-structure interaction problems in linear and nonlinear engineering applications: theory and experiments"

---

by
**Campanale Angelo**

Academic Supervisors:
**Prof. Carbone Giuseppe**
**Prof. Putignano Carmine**
**Prof. Soria Leonardo**
**Prof. Spagnolo Vincenzo**

Coordinator of Ph.D. Program:
**Prof. Demelio Pompeo Giuseppe**

---

Course n° 33, 1/11/2017-31/12/2020

Department of Mechanics, Mathematics and Management
MECHANICAL AND MANAGEMENT ENGINEERING
Ph.D. Program
SSD: ING-IND/13-APPLIED MECHANICS

**Final Dissertation**

# "Fluid-structure interaction problems in linear and nonlinear engineering applications: theory and experiments"

by
**Campanale Angelo**

Referees:
**Prof. Aureli Matteo**
**Prof. Dimitriadis Grigorios**

Academic Supervisors:
**Prof. Carbone Giuseppe**
**Prof. Putignano Carmine**
**Prof. Soria Leonardo**
**Prof. Spagnolo Vincenzo**

Coordinator of Ph.D. Program:
**Prof. Demelio Pompeo Giuseppe**

Course n° 33, 1/11/2017-31/12/2020

# Contents

**Introduction** **4**

## I FSI linear problem: QEPAS tuning fork device immersed in a fluid medium 8

**I.1 Introduction** **9**

**I.2 Mathematical model formulation** **13**
I.2.1 Dynamics equations . . . 13
I.2.2 Fluid-Structure Interaction . . . 14
I.2.3 Dynamics equations in the frequency domain . . . 17
I.2.4 Computation of the linear response . . . 18
I.2.5 Details of the solution scheme for the fundamental problem . . . 21
I.2.6 Analysis of the excitation sources . . . 25

**I.3 Experimental setup** **27**

**I.4 Results and discussion** **29**
I.4.1 Estimation of the hydrodynamic function's coefficients by computational fluid dynamics finite element simulations. . . . 35
I.4.2 Estimation of the system modal parameters by operational modal analysis . . . 38

**I.5 Conclusions** **46**

## II FSI nonlinear problem: Nonlinear inextensible plate in low speed airflow 48

**II.1 Introduction** **49**

**II.2 Mathematical model formulation** **54**
II.2.1 Structural modelling . . . 54
II.2.2 Aerodynamic modelling . . . 60
II.2.3 Implementation and validation of linear model . . . 64

**II.3 Nonlinear results** **70**

**II.4 Conclusions** **72**

**Final remarks** **73**

**List of figures** **75**

**List of tables** **78**

**Bibliography** **79**

# Abstract

In this dissertation, two fluid-structure interaction problems, related to different engineering applications, are analysed. In the first linear case, an analytical but effective model is formulated in order to correctly estimate the dynamic response of a quartz tuning fork (QTF) device immersed in a fluid environment. This kind of resonator is widely used for gas sensing applications. In the second nonlinear case, a numerical model is developed to get the aeroelastic response of thin cantilever flat plate, with a particular emphasis on the applicability of the inextensible plate theory to the structural modelling of the problem. Specifically, the main goal is to numerically predict flutter conditions and limit cycle oscillations (LCO) closer to experimental outcomes, since earlier model that makes use of Von Kármán thin plate theory overpredicts the LCO amplitude.

In the first part, the linear fluid-structure interaction problem is analysed: the mathematical model concerning the dynamics of the resonator and its interaction with the surrounding fluid is presented, the experimental setup, used to asses the model, is described, the theoretical response is fitted on the experimental data and, finally, a discussion on how each parameter of the mathematical model can affect the overall system dynamics is provided.

In the second part, where the nonlinear fluid-structure interaction case is studied, the mathematical model concerning the inextensible plate vibrating in low speed airflow is derived, the flutter condition and the limit cycle, in terms of amplitude and period, are calculated, and a comparison with Von Kármán plate structural model is provided with needed remarks on the obtained numerical results.

# Introduction

In recent years, the interest in the development of sophisticated engineering systems based on the fluid-structure interaction has been gaining great momentum. Basically, fluid-structure interaction (FSI) refers to the interaction experienced between a flexible structure and the fluid surrounding the structure [3–5]. This type of interaction is very interesting from the standpoint of engineering applications including, for example, modelling and design of aircraft wing structures [5], components of turbomachines [6, 7], design and construction of bridges [8–10], blood flow analysis through the arteries [11], scanning of biological materials and organic coatings [12, 13], gas and liquid sensing applications [1, 14, 15] and so on.
The presence of a fluid can strongly influence the dynamic behaviour of a deformable elastic body: for example, a static encompassing fluid can modify eigenfrequencies and relative damping ratios of a vibrating structure, as it happens for micromechanical oscillators and actuators vibrating in fluid environments [16–19], or a flowing fluid may exert pressure and/or thermal loads on the structure; these loads may cause structural deformation whose amplitude is large enough to cause a change in the fluid flow itself, which leads to further change in pressure on the structure. A positive feedback loop process takes place: the fluid flowing past the air plane wings causes their deformation, which modifies the airflow pattern [5, 20]. Fluid-structure interaction can generate not only a change in the motion of elastic structures but also undesired phenomena, such as fatigue [21, 22] or galloping [5, 23, 24], and eventually catastrophic structure failure.
In all this scenarios, the development and application of corresponding analytical and numerical methodologies have received wide attention over the past decades and several research studies pertaining to a variety of modelling and computational techniques, dedicated to explore the underlying physics of the phenomena related to fluid-structure interaction, have been developed [3, 5, 16, 25–29].
In this doctoral dissertation, emphasis is made on two examples of extremely different fluid-structure interaction problems that are studied and solved with different methods and techniques. In a first linear case, regarding the small amplitude oscillation in a quiescent fluid medium of a quartz tuning fork, deployed in gas sensing applications, the problem is solved by a Green's function based analytical approach. For a second case in the field of nonlinear aeroelasticity, where the main goal is to study the limit cycle oscillations (LCOs) of a thin cantilever flat plate in low speed airflow, a specialised mathematical model is developed, based on a combination of the inextensible thin plate theory and the Vortex Lattice aerodynamic modelling method.

In the first fluid structure-interaction problem, the dynamic response of a tuning fork device, used in the Quartz-enhanced photoacoustic spectroscopy (QEPAS), is studied by accounting for the effects due to interaction with the surrounding fluid. QEPAS is a trace gas sensing technique that employs a designed high-quality factor quartz tuning fork (QTF) as acousto-electric transducer [15,30–40]. The first in-plane skew-symmetric flexural mode of the QTF is excited when weak resonant sound waves are generated between the QTF prongs. Thus, the performance of a QEPAS sensor strongly depends on the resonance properties of the QTF, namely the determination of flexural eigenfrequencies and air damping loss [41,42].
The problem of forced vibrations of flexible slender structures vibrating in quiescent fluid media has recently gained a considerable interest from the research community in view of potential scientific and technological applications, such as atomic force microscopy [16,43–45], sensors and actuators based on micromechanical oscillators [17,18], like the QEPAS device presented in this thesis [30–40], cooling devices [19,46,47], smart materials [48–51] and so on. Therefore, design, analysis, and control of these devices rely on the detailed knowledge of dynamical aspects of the fluid-structure interaction and, specifically, on the estimation of the hydrodynamic actions exerted on the submerged structure by the encompassing fluid. In this regard, the scientific literature is full of interesting contributions on theoretical, experimental and numerical aspects of hydrodynamic actions between slender bodies and fluids [12,16,28,29,43,44,52–58].
In this dissertation, a mixed theoretical-experimental framework to study the dynamic response of a QTF while vibrating in a fluid environment is presented [1]. Due to the system linearity, the dynamic response of the resonator immersed in a fluid medium is obtained by employing a Boundary Element formulation [59] based on an *ad hoc* calculated Green's function. The boundary element methods (BEMs) allow to solve linear partial differential equations formulated in a boundary integral form. The BEMs have a great advantage over other numerical methods, such as finite element methods (FEMs) or finite differences: they reduce a bulk problem into a boundary problem, with all the resulting benefits in terms of computational cost. For this reason, boundary element methods are widely used in many fields such as fluid mechanics [60, 61], acoustics [62, 63], electromagnetism [64,65], fracture mechanics [66,67], contact mechanics [68–70] and so on. However, BEMs are applicable to linear problems for which Green's function or fundamental solutions can be analytically or numerically calculated, placing considerable restrictions on the range and generality of problems to which boundary elements can usefully be applied. Nonlinearities can also be included in the formulation such as in the Analog Equivalent Method (AEM) [71,72], where the nonlinear governing equation is replaced by an equivalent nonhomogeneous linear one with known fundamental solution and under the same boundary conditions or other advanced techniques.
In particular, in the presented model the QTF structure is described as constituted by a pair of two Euler-Bernoulli cantilevers partially coupled by a distributed linear spring. With regards to the forces exerted by the fluid on QTF structure, the so-called complex hydrodynamic function, which gives the hydrodynamic actions exerted by the encompassing fluid on the vibrating slender struc-

ture, has been derived by adopting a novel heuristic approach.

Fluid inertia and viscosity as well as an additional diffusivity term, whose influence is crucial for the correct evaluation of the system response, have been taken into account in the proposed hydrodynamic function, which needs to be fitted on experimental response [1, 14]. Then, following the canonical framework of BEM, the problem can be expressed with an integral equation between forces and displacements. By corroborating the theoretical analysis with the experimental outcomes obtained by means of a vibro-acoustic setup, the dynamics of the QTF immersed in a fluid environment is fully determined.

In the second fluid-structure interaction problem, the nonlinear aeroelastic response of a thin cantilever flat plate is studied. The emphasis is on predicting flutter conditions (speed and frequency) and Limit Cycle Oscillations (LCOs), in terms both amplitudes and frequencies. Aeroelastic flutter, defined as an unstable, self-excited structural oscillation at a definite frequency where energy is extracted from the airstream by the motion of the structure [5], is ubiquitous in a wide range of engineering fields, especially in applications which involve flexible and slender structures like bridges and buildings [8–10] or airplane wings [73, 74]. In nonlinear systems, flutter usually leads to a kind of periodic oscillations with limited or unlimited amplitude, known as Limit Cycle Oscillations (LCOs) that can lead to fatigue [21, 22] or failure of the structure. Therefore, in applications that rely on the structural integrity of flexible bodies, flutter phenomenon is a significant cause for concern due to its role in driving the dynamics of the structure and eventually in a catastrophic failure of the system. While being detrimental in a wide range of such applications, flutter is, on the other hand, seen as a possible method of harvesting energy from naturally occurring flow fields [75, 76], such as tidal currents, due to its ability to extract energy from the surrounding flow. Hence, the ability to suppress as well as enhance this flow-induced motion is a problem of broad relevance. It is worth pointing out that the flutter instability is due to an energy exchange between fluid and structure and flutter or LCOs can never occur without a fluid stream [5]. Thus, over the past decades, numerous analytical, computational, and experimental works have been proposed in order to predict flutter speed and LCOs accurately [77–87].

In this thesis, the aeroelastic response of a plate in low speed airflow is derived using a combination of the linearised continuous time vortex lattice method (VLM) [78, 79, 86], as aerodynamic model, and the inextensible thin plate theory [91], concerning the structure.

VLM approach has already been demonstrated to yield good predictions of the instability onset conditions (flutter speed and frequency) [86–88] and to be a good compromise between accuracy and computational cost for modelling the aerodynamic loads on slender bodies [83].

The inextensible thin plate theory has been recently developed with the specific goal of capturing the large out-of-plane deflections of thin plates or wings during limit cycle oscillations that have been observed in experiments [90]. Indeed this new theory has been developed with an higher order accuracy on the bending energy than other nonlinear plate models, such as Von Kármán thin plate theory [92].

The model is solved for the amplitude and period of the limit cycle of the flat plate using numerical integration [5]. The resulting predictions are compared to theoretical predictions obtained using Von Kármán thin plate theory for an identical flat plate. It is shown that the aeroelastic model predicts the linear flutter conditions of the plate with reasonable accuracy and the limit cycle amplitude, calculated from the inextensible plate theory, has a shape of the LCO amplitude curve very similar to the one obtained during of experimental test on similar plates [87], contrary to the amplitude predictions of the Von Kármán model. This striking feature is very encouraging for future experimental and numerical work. Thus the improved accuracy of inextensible plate theory will not only yield estimates that are closer to the experimental measurements but will also shed light on the nature of the nonlinearity present in the wings and the type of bifurcation that causes the LCOs.
Ultimately, it is worth mentioning that the solution and results of the two fluid-structure interaction problems analysed in this dissertation, presented, specifically, in parts I and II, have been published, respectively, in A. Campanale, C. Putignano, S. D. Carolis, P. Patimisco, M. Giglio, L. Soria, *A theoretical-experimental framework for the analysis of the dynamic response of a QEPAS tuning fork device immersed in a fluid medium*, appeared on *Mechanical Systems and Signal Processing*, 149, 107298, 2021, doi: 10.1016/j.ymssp.2020.107298 [1] and in A. Campanale, L. Soria, G. Kerschen, G. Dimitriadis, *Modelling the limit cycle oscillations of flat plate wings using inextensible plate theory and the vortex lattice method*, presented at the International Conference on Noise and Vibration Engineering ISMA 2020 [2].

# Part I

# FSI linear problem: QEPAS tuning fork device immersed in a fluid medium

# Chapter I.1

# Introduction

The sensitive and selective detection of trace gas concentrations has found widespread applications [15], and includes several fields, such as environmental monitoring [93], industrial process control [94], rural and urban emission studies [95], chemical analysis and control of manufacturing processes [96]. Numerous analytical instruments based on optical and non-optical techniques have been developed with the aim to offer high sensitivity and selectivity, multicomponent detection capability, room temperature operation, fast response time, large dynamic range, and ease of use [97].
Optical techniques based on tunable laser absorption spectroscopy (TDLAS) for trace gas sensing are not far from being able to meet these requirements. Among them, photoacoustic spectroscopy (PAS) has established as a very attractive technique for sensitive trace gas detection [97]. It is based on the photoacoustic effect [30, 31], i.e. on the generation of sound waves as a consequence of the absorption of modulated light by a target gas. PAS uses resonant cells to enhance the acoustic wave and sensitive microphones to detect and transduce it into an electric signal [32, 33]. Thus, PAS does not require an optical detector and the detection scheme is wavelength-insensitive.
Since 2002 [34,35], Quartz-Enhanced PAS (QEPAS) has been proposed as a variant of traditional PAS: the acoustic cells are, in this case, replaced by small quartz tuning forks (QTFs), acting as sharply resonant acoustic transducers to detect weak photoacoustic excitation. The employment of a QTF allowed size reduction of the acoustic detection unit as well as high immunity, during operation, to environmental noise caused by external excitation sources, owing to the reduction of the detection bandwidth due to the high quality factor of the QTF resonance. Therefore, QEPAS technology is competitive with and, in many cases, preferred to other trace gas sensing methods [36–40].
Looking at its mechanical structure, a QTF can be considered as two cantilevers (prongs) joined at a common base. The in-plane flexural modes of vibrations of the QTFs can be classified into two groups: symmetrical modes, where the prongs moves along the same direction, and anti-symmetrical modes, where the two prongs oscillate along opposite directions [98, 99]. The in-plane anti-symmetrical modes are the predominant ones when a sound source is positioned between the prongs, forcing them to move in the opposite directions. In QEPAS sensors, as

shown in the schematic in Figure 1, the light source is focused between the QTF prongs and the sound waves produced by the modulated absorption of the gas are generated between the QTF prongs, forcing them to vibrate anti-symmetrically back and forth. A schematic of the core of a QEPAS sensor is sketched in Figure I.1. Thus, in-plane anti-symmetrical modes of the QTF are excited. When these oscillations occur at one of the resonance frequencies of the QTF, the induced strain field generates surface electric charges due to the quartz piezoelectricity and the total charge is proportional to the intensity of the sound waves incident on the QTF prongs. The generated charges are collected using a transimpedance amplifier and the measured electrical signal is proportional to the concentration of absorbing gas species.

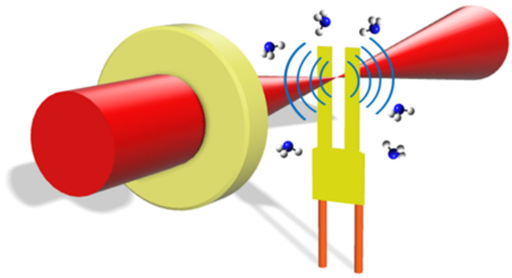

Figure I.1: QEPAS principle of operation. A QTF is immersed in a fluid and laser light is focused between two QTF prongs. Weak sound waves generated by photoacoustic effect deflect the prong in two opposite directions.

As a consequence, the performance of a QEPAS sensor is strongly determined by the resonance properties of the QTF, which is fully immersed in the gas sample. Thus, it is crucial to study the response of the QTF in a fluid medium while it is vibrating, at the in-plane anti-symmetrical flexural mode. Several theoretical models describing the main loss mechanisms, namely the air damping [100–102], support losses [101], [103–105] and thermoelastic damping [106] have been proposed for a single cantilever oscillating in fluid medium or in vacuum. These models have been applied to a QTF to predict dependence of the quality factor on the QTF prong geometry, for both the fundamental and first overtone flexural mode [41, 42]. While the trends are well predicted, QTF overall quality factor values are poorly estimated. Besides, when assuming fixed the base plate and neglecting the coupling between the two prongs, an excellent estimation of the in-plane flexural eigenfrequencies can be obtained only as long as the QTF prongs are slender beams [107]. Conversely, for QTF geometry with squat prongs, neglecting the vibration of the base plate and its coupling effect can lead to incorrect estimation of the eigenfrequencies. For this reason, the effect of the base plate, as vibrating and structural coupling element, has to be considered [108].
In this thesis, a theoretical-experimental model to determine the response of the QTF vibrating in a fluid medium in a relatively simple and phenomenological way is proposed. As a consequence, this approach will provide more control on

the governing parameters of the physical phenomenon: these will be easily recognized, controlled and optimized, and without using computational-demanding fluid-structure interaction numerical simulations [3]. Specifically, the proposed model employs a combined analytical-experimental methodology to analyse the dynamic response of a quartz tuning fork when forced to vibrate to the fundamental anti-symmetrical flexural mode, by accounting for the effects due to the interaction with the surrounding fluid. Due to its linearity, the system response is calculated by using an *ad hoc* Green's function. The system domain includes two Euler-Bernoulli beams partially coupled by a distributed linear spring [109], used to model the plate connecting the two prongs as well as the underlying part. The drag force exerted by the fluid on the QTF is modelled by the so-called hydrodynamic function. Such hydrodynamic actions can be resolved into a mass adding effect, given by the real part of the hydrodynamic function, and a hydrodynamic damping, given by the imaginary part of the hydrodynamic function [12,16,28,29,43,44,52–58]. Consequently, when compared to in-vacuum conditions, structures vibrating within a viscous fluid exhibit comparatively lower resonance frequencies and increased damping [16, 28, 29]. The analytical estimation of the hydrodynamic actions exerted by the encompassing fluid is generally very challenging due to the complexity of the three dimensional (3D) vibrations, however mathematically tractable formulations have been proposed based on the simplifying assumption of small amplitude flexural vibrations of the structure and the fluid loading can be computed by studying a two dimensional (2D) unsteady Stokes' flow described by linearised Navier-Stokes equations, where convective terms are neglected [4, 110–112]. Following this approach, an exact analytical expression of the hydrodynamic function for an infinitely long beam with a cross section transversally vibrating in a viscous fluid can be derived, see for example Ref. [113]. The formulation of an exact analytical solution of the hydrodynamic function for a beam that is rectangular in cross section poses a formidable challenge and an exact analytical solution to the problem was proposed by Kanwal [114], whose formulation is complicated and requires a huge amount of numerical computations.

A pioneering work in the field is the asymptotic investigation proposed by Tuck [28]. In this work is demonstrated that the hydrodynamic function for a circular cylinder and an infinitely thin rectangular beam are approximately identical and possess the same asymptotic forms in the limits as the frequency (or the Reynolds number) goes to 0, where the only hydrodynamic action is given by an infinitely big viscous term, and infinity, where the only hydrodynamic action is given by a constant inertial term. Tuck also proposed a numerical methodology to adapt the exact hydrodynamic function for a circular beam to the hydrodynamic function for a rectangular beam. Recently, Sader [16] applied the work by Tuck to study the frequency response of cantilever beams immersed in viscous fluids with applications to atomic force microscope (AFM) cantilever beams. In Ref. [29] is studied the drag exerted by a viscous fluid on a vibrating beam near a wall and in [52] is exploited the fluctuation-dissipation theorem to capture the Brownian dynamics of the coupled fluid-cantilever system for AFM application, since the micrometric cantilever beam of an AFM is particularly affected by

Brownian noise. Ultimately, of particular interest are also the contributions in Refs. [12,55,56], where the methodology proposed by Tuck is extended beyond the range of validity of the linear theory developed and nonlinear phenomena, such as vortex shedding and convection, are included, in Refs. [57,58], where the coupling hydrodynamic effects between two cantilever beams are investigated, in Ref. [12], where the contact effects between the tip of the AFM beam and the sample in liquid environments are examined and a lot of theoretical, numerical and experimental literature has been developed, in the past years, in order to study the hydrodynamic effects of slender structure in fluid environments [14, 45, 115–117]. In this thesis, an analytical hydrodynamic function, heuristically derived, is proposed for the in-plane vibrations of a QEPAS tuning fork device immersed in a fluid medium [1]. The proposed model taken into account not only for fluid inertia and viscosity but also for a diffusivity vorticity term [4, 111, 112], taking inspiration from the so-called "second Stokes' problem" where the motion of an infinite plane surface vibrating in its own in a viscous fluid is governed by a pure diffusive equation. The cruciality of a diffusive term has been demonstrated in [14] also for out-of-plane vibrations.
Then, as usually done for many applications in solid mechanics [68–70, 118], in the framework of the Boundary Element Methodology (BEM) [59], the problem is reduced to the solution of an integral equation between forces and displacements. Once the theoretical expression of the system response is determined, an experimental test on a specific QTF vibrating in air was performed to fine tune the theoretical response. An acoustic stationary random field generated by two speakers has been used to excite the QTF and the resulting forced vibration time series has been measured and recorded by using a Laser Doppler vibrometer (LDV), while an electronic microphone has been employed to measure the acoustic pressure in a specific point close to the QTF.

# Chapter I.2

# Mathematical model formulation

## I.2.1 Dynamics equations

In this section, the mathematical model describing the in-plane flexural vibration of a quartz tuning fork (QTF) device immersed in a viscous fluid is presented. The structure is split into four parts, each modelled as a one-dimensional (1D), linear Euler-Bernoulli beam with a rectangular cross section of thickness $h$. The underlying two beams are considered coupled by a set of distributed linear springs with constant stiffness per unit length $k$, as represented in Figure I.2. Specifically, the two interconnected beams, labelled as BL (bottom-left) and BR

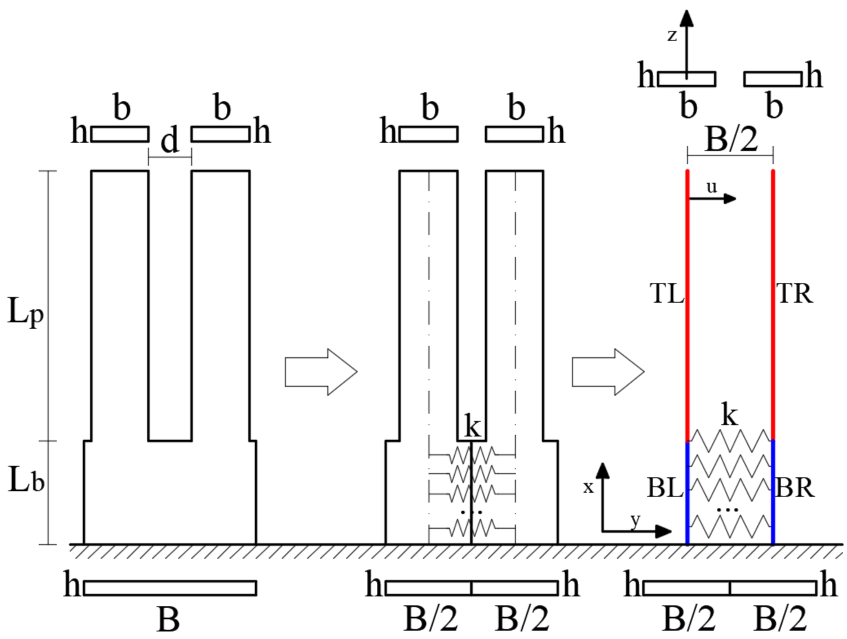


Figure I.2: Reduction of the 3D QTF to a 1D Euler-Bernoulli model.

(bottom-right), having width $B/2$ and length $L_b$, model the base plate of the QTF; the beams labelled as TL (top-left) and TR (top-right), with width $b$ and length $L_p$, model the two prongs of the tuning fork. Beams BL and TL and beams BR and TR are, respectively, segments of two cantilevers with length $L = L_b + L_p$, each having a step discontinuity on the cross section. Their dynamics is governed by the following motion equation

$$EJ(x)\frac{\partial^4 u_i(x,t)}{\partial x^4}+\rho A(x)\frac{\partial^2 u_i(x,t)}{\partial t^2}+k(x)\left(u_i(x,t)-u_j(x,t)\right)=f_i(x,t) \quad \text{(I.1)}$$

where $t$ is the time variable, $x$ is the common coordinate along the beam axes, with $y$ and $z$ the coordinates along the width and thickness directions, respectively. Furthermore, $u_i(x,t)$ and $u_j(x,t)$ indicate the in-plane elastic deflection of the $i$-th and $j$-th cantilever, respectively, with $i, j = 1, 2$ and $i \neq j$; $\rho$ and $E$ are the mass per unit volume and the Young's modulus of the material of the beams, respectively. Finally, we have $A(x) = A_b - \mathcal{H}(x - L_b)(A_b - A_p)$, with $\mathcal{H}(x)$ the Heaviside unit step function, $A_b = hB/2$ and $A_p = hb$ the cross-section areas of the bottom and top segments, respectively, $J(x) = J_b - \mathcal{H}(x - L_b)(J_b - J_p)$, with $J_b = h(B/2)^3/12$ and $J_p = hb^3/12$ the corresponding inertia moments; the coupling stiffness $k(x)$ is equal to $k(1 - \mathcal{H}(x - L_b))$. The forcing term $f_i(x,t)$ is equal to $f_i^{ext}(x,t) + f_i^F(x,t)$, where $f_i^{ext}(x,t)$ is the overall external force per unit length acting on the $i$-th beam, not including the contribution $f_i^F(x,t)$, exerted by the encompassing fluid, that is assumed to be Newtonian and incompressible.

The boundary conditions to be taken into account for each cantilever are the well-known fixed-free boundary conditions, that is $u_i(0,t) = 0$, $\partial u_i(0,t)/\partial x = 0$, $\partial^2 u_i(L,t)/\partial x^2 = 0$, $\partial^3 u_i(L,t)/\partial x^3 = 0$.

## I.2.2 Fluid-Structure Interaction

Assuming small in-plane deflections, the fluid response can be considered linear and the force $f_i^F(x,t)$ can be evaluated by means of the following Green's function approach [14]

$$f_i^F(x,t)=\int_{-\infty}^{t}\int_0^L d\tau dx' G_F(x,x',t-\tau)\frac{\partial u_i^2(x',\tau)}{\partial \tau^2} \quad \text{(I.2)}$$

where the form of $G_F(x,x',t)$ is heuristically derived. Specifically, by assuming $L \gg b$ and $b \gg h$, it is possible to neglect the three-dimensional (3D) phenomena related to variations of the flow physics along the beams' axes, as the beams' cross-sections are assimilated to rigid slender bodies. Thus, the hydrodynamic loading per unit length can be estimated by studying the two-dimensional (2D) flow induced by the small amplitude oscillations of those bodies in the transversal direction [16, 29, 52, 57, 58, 117]. Thus, the fluid response can be modelled as $G_F(x,x',t) = G_F(x,t)\,\delta(x - x')$, rephrasing accordingly Equation (I.2) as

$$f_i^F(x,t)=\int_{-\infty}^{t} d\tau G_F(x,t-\tau)\frac{\partial u_i^2(x,\tau)}{\partial \tau^2} \quad \text{(I.3)}$$

In this way, it is possible to study the unsteady Stokes' flow generated by the linear oscillation of an isolated slender body, governed by the following equations

$$\frac{\partial \mathbf{W}}{\partial t} = \nu \nabla^2 \mathbf{W} \tag{I.4}$$

$$\nabla \cdot \mathbf{v} = 0 \tag{I.5}$$

where $\nabla$ and $\nabla^2$ are the Nabla and Laplace operators. Equation (I.4) represents the linearised momentum equation, expressed in form of vorticity $\mathbf{W} = \nabla \times \mathbf{v}$ [4], while Equation (I.5) is the continuity equation, with $\mathbf{v}$ and $\nu$ the velocity and the kinematic viscosity of the fluid, respectively.

As the vorticity is governed by a diffusive-like equation, it generates a solution in terms of velocity that exponentially decays from the boundary of the body toward the interior fluid. The amplitude of this exponential decays allows the estimation of the thickness $h_f$ of the fluid layer, where the fluid behaves as rotational and the diffusion of the tangential velocity is important. Let us notice that $h_f \approx \sqrt{\nu/\omega}$, where $\omega$ is the characteristic radian frequency of the motion. Outside of the layer, the term $\nu\nabla^2\mathbf{W}$ can be neglected and a potential flow is established.

Since $h_f$ is frequency-dependent, it is very small in the high frequency range, with the fluid response solely governed by inertial effects and, thus, proportional to the acceleration of the moving body. In this case, the Green's function of the fluid has to be proportional to the Dirac Delta function $\delta(t)$ by means of a certain inertia coefficient $\mu(x)$. Conversely, at low frequencies, the Eulerian rate of change $\partial\mathbf{W}/\partial t$ can be neglected and $h_f$ becomes larger than the characteristic dimensions of the moving body. In this case, the fluid response is expected to be linearly proportional to the body velocity, implying a form of the fluid Green's function proportional to a specific damping coefficient $c(x)$. In the mid frequency range, the effects of vorticity diffusion are predominant [4]. Thus, in this latter case, the fluid Green's function has to come inversely proportional to $\sqrt{t}$, by a particular diffusive coefficient $\alpha(x)$.

In conclusion, due to the linearity of the sought fluid response, the overall force exerted by the fluid on the oscillating body has to be the sum of those three contributions

$$\begin{aligned} &G_F(x,t) = -c(x) - \frac{\alpha(x)}{\sqrt{t}} - \mu(x)\delta(t) \quad t \geqslant 0 \\ &G_F(x,t) = 0 \quad t < 0 \end{aligned} \tag{I.6}$$

Equation (I.6), which satisfies the causality principle, clearly is an heuristic approximation of the fluid response. Furthermore, the dependence of the three fluid coefficients on the spatial abscissa $x$ is negligible in the case of an isolated cantilever vibrating in an unbounded fluid [14], as in the case considered in the present study. To estimate the numerical values assumed by the three coefficients in our application, the best fit of the experimental response has to be performed.

By substituting Equation (I.6) in Equation (I.3), the following expression of the exerted fluid force is obtained

$$f_i^F(x,t) = -c\frac{\partial u_i(x,t)}{\partial t} - \alpha \int_{-\infty}^{t} d\tau \frac{1}{\sqrt{t-\tau}} \frac{\partial u_i^2(x,\tau)}{\partial \tau^2} - \mu \frac{\partial u_i^2(x,t)}{\partial t^2} \tag{I.7}$$

Equation (I.7) can be transformed from time to Laplace domain with $s = \mathrm{i}\omega$, where $s$ the Laplace variable, $\mathrm{i} = \sqrt{-1}$, $\omega = 2\pi \mathrm{f}$ with f the time frequency, and, so that, $\hat{u}_i(x, s) = \int_0^{+\infty} dt\, u_i(x, t)\, \mathrm{e}^{-st}$. Ultimately, it is possible to define

$$\hat{f}_i^F(x, \omega) = \omega^2 \Gamma(\omega)\, \hat{u}_i(x, \omega) \tag{I.8}$$

where

$$\Gamma(\omega) = \mu + \alpha\sqrt{\frac{\pi}{2}}\omega^{-1/2} - \mathrm{i}\left(c\omega^{-1} + \alpha\sqrt{\frac{\pi}{2}}\omega^{-1/2}\right) \tag{I.9}$$

is the so-called hydrodynamic function [16, 57, 58, 117], whose real part describes the fluid added mass, while the imaginary part accounts for the hydrodynamic damping.

The diffusive-velocity contribution, proportional to the $\alpha$ coefficient, gives rise to two identical terms appearing symmetrically in the real and imaginary parts of $\Gamma(\omega)$, implying that this contribution equally influences both the added mass and the hydrodynamic damping, and, in turn, both the eigenfrequencies and the quality factors associated to system eigenmodes. The overall mass adding effect can be neglected, as also reported in literature (see Refs. [41,107,119]), in the case of QEPAS applications, and in Refs. [120,121], in the case of the laterally vibrating microcantilevers; while a correct estimation of the hydrodynamic damping is crucial, since the QTF quality factor plays a fundamental role in design and operation of those resonators. Indeed, at atmospheric pressure the fluid damping is the dominant energy dissipation mechanism [41, 42, 107] and any form of internal structural dissipation can be neglected.
Now, it interesting to focus more in detail on the key feature marking the hydrodynamic function $\Gamma(\omega)$, that is, the presence of the diffusive velocity term in the description of the fluid force exerted on the structure. Specifically, by accounting for this term, it is possible to consider the effects of the tangential velocity diffusion, going from the fluid layer, adhering to the skin of each beam, towards the interior part of the fluid region. From a physical point of view, this has a crucial importance as it can be understood by focusing on a very simple model. Indeed, the case of a Newtonian, incompressible and viscous fluid bounded by an infinite plane surface, which executes small oscillation in its own plane, can be considered. This simple but typical example was originally studied by [110] and recently reproposed by [4, 111, 112].
In particular, the solid surface is placed in the $xy$-plane, the fluid region coincides with the half-space for $z > 0$ , the direction of the surface oscillation is taken in the $y$-axis and the time law of the surface velocity is given by an harmonic oscillatory motion. In this specific case, the motion of the fluid is governed by a purely 1D diffusive equation [4]

$$\rho\frac{\partial v_y}{\partial t} = \eta\frac{\partial^2 v_y}{\partial z^2} \tag{I.10}$$

where $v_y$ is the fluid velocity in the $y$-direction and $\eta$ the dynamic viscosity of the fluid.
An explicit solution can also be derived of the problem of a fluid set in motion by

a plane surface moving in its plate according to any law $u = u(t)$. The required solution is formally identical with that of an analogous problem in theory of thermal conduction, whose calculations are explicitly reported in [4]. In particular, the shear stress exerted by the fluid on the surface, for this kind of problem, is given by

$$\sigma_{zy} = -\sqrt{\frac{\eta\rho}{\pi}} \int_{-\infty}^{t} d\tau \frac{1}{\sqrt{t-\tau}} \frac{\partial^2 u(\tau)}{\partial \tau^2} \tag{I.11}$$

where $u$ is the displacement of the plane surface; this expression is formally identical to the diffusive term of the Equation (I.7).

Such an infinite planar surface oscillating in a viscous fluid, fits perfectly the conditions of the device under study in this thesis, i.e. the QTF#S15, whose dimensions are listed in Table I.1. Indeed, each single prong can be approximated to a flat plate moving in a viscous fluid. Furthermore, with the regards to the role of diffusion in Equation (I.9), it is well known in literature that, apart from the added mass constant, terms depending on $\omega^{-1/2}$ of both real and imaginary part of $\Gamma(\omega)$ are arguably, in the frequency range of interest, the leading ones in a series expansion of the hydrodynamic function. This has been demonstrated, for example, in Ref. [16] for the out-of-plane motion in fluid of a single microcantilever and in Ref. [120,121] for its in-plane motion; a similar scaling effect has to be considered in the case of the hydrodynamic coupling of two microcantilevers, as shown in Ref [57].

Ultimately, these considerations suggest that it is possible to neglect the contribution of the viscous term $c$ and obtain a simplified expression of the hydrodynamic function, as

$$\Gamma(\omega) = \mu + (1 - \mathrm{i})\,\alpha\sqrt{\frac{\pi}{2}}\omega^{-1/2} \tag{I.12}$$

A more detailed analysis on the estimation of the hydrodynamic function's coefficients, on the dominance of the diffusive term, and on the negligible effect of mass adding can be found in section I.4.1, where these considerations are corroborated by a CFD analysis. Specifically, there is shown that $c\omega^{-1} \ll \alpha\sqrt{\pi/2\omega}$ and that the whole real part of $\Gamma(\omega)$ can be neglected when compared to the cantilevers' mass per unit length, that is $\mu + \alpha\sqrt{\pi/2\omega} \ll \rho A(x)$.

### I.2.3 Dynamics equations in the frequency domain

By rephrasing the motion equations of the two cantilevers (I.1) in the frequency domain, accounting for Equation (I.8) and adopting a suitable matrix notation, the following compact description of the QTF dynamics can be obtained

$$\frac{\partial^4 \bar{u}(x,\omega)}{\partial x^4} + \bar{\bar{B}}(x,\omega)\,\bar{u}(x,\omega) = \bar{f}^{ext}(x,\omega) \tag{I.13}$$

where $\bar{u}(x,\omega) = \{\hat{u}_1(x,\omega), \hat{u}_2(x,\omega)\}^{\mathrm{T}}$,

| QTF#S15 Dimensions [mm] | |
|---|---|
| Prong Length | $L_p = 9.4$ |
| Base Length | $L_b = 3.6$ |
| Prong Width | $b = 2$ |
| Base Width | $B = 6$ |
| Prong Spacing | $d = 1.5$ |
| QTF Thickness | $h = 0.25$ |

Table I.1: Dimensions of the QTF#S15 device used in this work, the nomenclature refers to Figure I.2.

$\bar{f}^{ext}(x,\omega) = (1/EJ(x))\left\{\hat{f}_1^{ext}(x,\omega), \hat{f}_2^{ext}(x,\omega)\right\}^{\mathrm{T}}$, in which T denotes matrix transposition, and

$$\bar{\bar{B}}(x,\omega) = \begin{bmatrix} B(x,\omega) & -\frac{k(x)}{EJ(x)} \\ -\frac{k(x)}{EJ(x)} & B(x,\omega) \end{bmatrix}$$

with $B(x,\omega) = (1/EJ(x))\left(-\omega^2(\rho A(x) + \Gamma(\omega)) + k(x)\right) \approx$
$\approx (1/EJ(x))\left(-\omega^2\left(\rho A(x) - \mathrm{i}\alpha\sqrt{\pi/2\omega}\right) + k(x)\right)$, since, as anticipated, $c\omega^{-1} \ll$
$\ll \alpha\sqrt{\pi/2\omega}$ and $\mu + \alpha\sqrt{\pi/2\omega} \ll \rho A(x)$.

The fluid coupling between the prongs is neglected in the QTF dynamics modelled by the set of Equations (I.13). In fact, on the one hand, being the QEPAS technique a gas sensing application, the densities of operated fluids are at least 3 order of magnitude lower than the density of the QTF material, i.e. quartz. On the other hand, the prongs' spacing is comparable to the prongs' width and it is several times larger than the prongs' thickness. With QTF#S15, investigate in this work, the spacing-to-width ratio is equal to 0.75, while the spacing-to-thickness ratio is equal to 6 (see Table I.1).

## I.2.4 Computation of the linear response

By relying on the linearity of system's Equations (I.13), a Green's function approach has been adopted to determine the specific solution of the problem. Hence, the system's complex Green's function is calculated, even referred to the susceptibility function, which is the solution of the so-called fundamental problem [14]. Specifically, a concentrated force of unit impulse is supposed to be applied to a generic cross-section $\xi$ of the resonator (Figure I.3), that is, to a certain section $\xi$ of the $j$-th cantilever, when the other remains unloaded. The output of the $i$-th cantilever when the system is subjected to such a loading condition of this kind [122] is denoted with $G_{ij}(x,\xi,\omega)$, as depicted in Figure I.3. Details on the computation are reported in the next section.

Then, the in-plane elastic deflection of each cantilever, caused by a generic load $\bar{f}(x,\omega)$ acting on the system, is calculated by means of the following integral equation

$$\hat{u}_i(x,\omega) = \int_0^L d\xi\, G_{ii}(x,\xi,\omega)\, \hat{f}_i(\xi,\omega) + \int_0^L d\xi\, G_{ij}(x,\xi,\omega)\, \hat{f}_j(\xi,\omega) \qquad \text{(I.14)}$$

where $i, j = 1, 2$ and $i \neq j$.

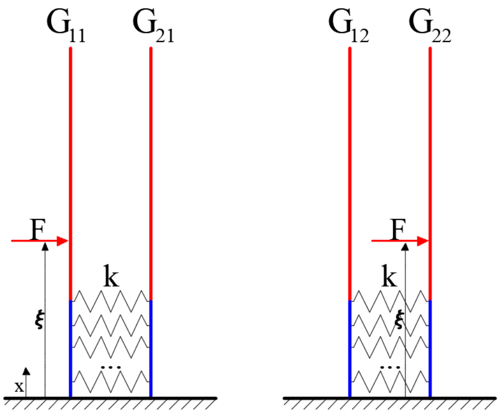


Figure I.3: Susceptibility function adopted notation. The susceptibility function comprises $G_{11}(x,\xi,\omega)$ and $G_{21}(x,\xi,\omega)$ in the case the unit impulse concentrated force is applied to a generic section $\xi$ of the left cantilever while the right one remains unloaded (left panel); $G_{12}(x,\xi,\omega)$ and $G_{22}(x,\xi,\omega)$ in the case the load is exerted on a section $\xi$ of the right cantilever with the left unforced (right panel).

It is worth to observe that the susceptibility function $G_{ij}(x,\xi,\omega)$ is function of the fluid coefficient $\alpha$ as well as of the coupling stiffness $k$, whose numerical values can be found by tuning the model with experimental outcomes. The experimental response will be fitted in correspondence to the first skew-symmetric in-plane flexural mode, which is the piezoelectrically active mode of QTFs typically employed in QEPAS applications. For QTF#S15, it falls at 15.808 kHz. In Figure I.4, the magnitude and the phase angle of the susceptibility functions of both cantilevers are reported, evaluated at their tips $x = L$, while the concentrated force is applied to the half-length of the base $\xi = L_b/2$ of the left cantilever. It possible to notice that the two prongs vibrate out of phase, as expected in the case of the first skew-symmetric in-plane flexural mode.

In order to calculate the susceptibility functions $G_{ij}(x,\xi,\omega)$ accounting for the system boundary conditions, the solution of the fundamental problem is obtained in a discrete form (details are reported in the next section).
Then, these susceptibility functions are stored in a matrix form by adopting the following numerical procedure: (i) discretize the interesting range of frequencies $\omega_k$ with $N_k$ points and the spatial abscissas $x_r$ and $\xi_s$ with $N$ points along the total cantilever length $L$, thus defining the spatial discretizations as $\Delta x = \Delta\xi = L/(N-1)$, (ii) apply, for fixed value of $\omega_k$, a concentrated load at a generic section $\xi_s$ of a single cantilever and compute the quantities $G_{ij}(x_r, \xi_s, \omega_k)$ for $i, j = 1, 2$, by solving the fundamental problem, (iii) repeat the previous step for all the $\omega_k$ values included in the chosen frequency range.

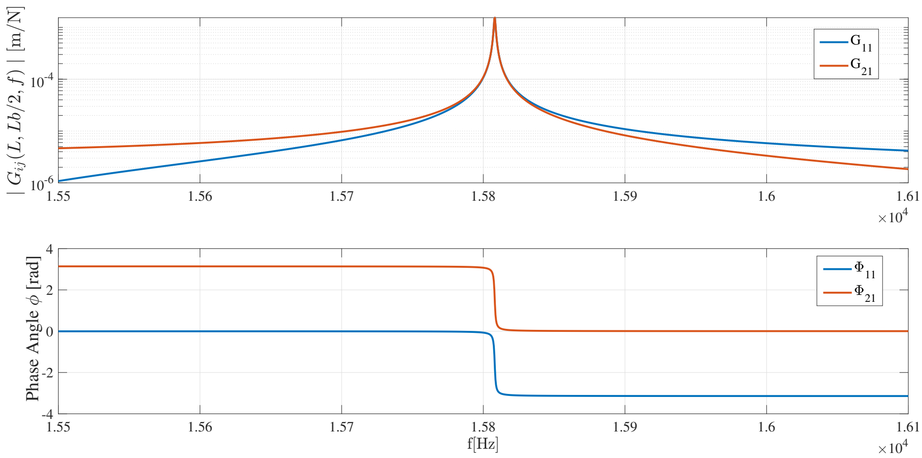


Figure I.4: Magnitudes and phase angles of susceptibility functions $G_{11}(L, L_b/2, \omega)$ (blue curve) and $G_{21}(L, L_b/2, \omega)$ (red curve) of the two cantilevers of QTF#S15, computed by employing as coefficients
$\alpha = 2.341 \times 10^{-5}\,\mathrm{Pa\,s^{3/2}}$ and $k = 1.7865 \times 10^9\,\mathrm{Pa}$.

By following this procedure, the matrices $[\mathbf{G}]_{ij}$ for both cantilevers are obtained

$$[\mathbf{G}]_{ij} = [G_{ij}(x_r, \xi_s, \omega_k)] \tag{I.15}$$

with $i, j = 1, 2$, $r = 1, ..., N$, $s = 1, ..., N$ and $k = 1, ..., N_k$. It is worth noting that, for a fixed frequency, a column of the $[\mathbf{G}]_{ij}$ matrix represent the in-plane elastic deflection of the system when a concentrated load is applied to a generic section.
Now, the global susceptibility matrix $\bar{\bar{\mathbf{G}}}$ can be defined as

$$\bar{\bar{\mathbf{G}}} = \begin{bmatrix} [\mathbf{G}]_{11} & [\mathbf{G}]_{12} \\ [\mathbf{G}]_{21} & [\mathbf{G}]_{22} \end{bmatrix} \tag{I.16}$$

where, due to the symmetry of the problem, $[\mathbf{G}]_{11}$ is equal to $[\mathbf{G}]_{22}$ and $[\mathbf{G}]_{12}$ is equal to $[\mathbf{G}]_{21}$.
The load vector $\bar{\mathbf{F}}$ and the displacement vector $\bar{\mathbf{U}}$ are defined as

$$\bar{\mathbf{F}} = \begin{Bmatrix} \{\mathbf{F}\}_1 \\ \{\mathbf{F}\}_2 \end{Bmatrix} \qquad \bar{\mathbf{U}} = \begin{Bmatrix} \{\mathbf{U}\}_1 \\ \{\mathbf{U}\}_2 \end{Bmatrix} \tag{I.17}$$

with $\{\mathbf{F}\}_i = \left\{ \hat{f}_i(\xi_s, \omega_k)\Delta\xi \right\}$ for $i = 1, 2$, $s = 1, ..., N$, and $k = 1, ..., N_k$; and $\{\mathbf{U}\}_i = \left\{ \hat{U}_i(x_r, \omega_k) \right\}$ for $i = 1, 2$, $r = 1, ..., N$, and $k = 1, ..., N_k$. Therefore, it is possible to describe the in-plane displacement of each cantilever in a convenient matrix form as a canonical BEM formulation for a fixed value of temporal frequency $\omega_k$, as

$$\bar{\mathbf{U}} = \bar{\bar{\mathbf{G}}}\bar{\mathbf{F}} \tag{I.18}$$

Equation (I.18) is the discrete version of integral Equation (I.14) and correlates displacements with loads by means of the global response matrix of the system.

## I.2.5 Details of the solution scheme for the fundamental problem

Here, the fundamental problem, in which an impulsive force is applied to a section $\xi$ of the bottom beam of the left cantilever, while the right one remains unloaded, is solved. Rewriting the set of Equations (I.13) for the fundamental problem, sketched in Figure I.5, left panel, as

$$\frac{\partial^4 \bar{G}(x,\xi,\omega)}{\partial x^4} + \bar{\bar{B}}(x,\omega)\bar{G}(x,\xi,\omega) = \bar{f}(x,\xi,\omega) \tag{I.19}$$

where $\bar{G}(x,\xi,\omega) = \left\{G_{11}(x,\xi,\omega), G_{21}(x,\xi,\omega)\right\}^{\mathrm{T}}$ and $\bar{f}(x,\xi,\omega) = \left\{\delta(x-\xi), 0\right\}^{\mathrm{T}}$.

The $x$-dependence of $\bar{\bar{B}}(x,\omega)$ is due to the step discontinuity on the cross-section of the cantilevers at $x = L_b$ which makes the system of Equations (I.19) nonlinear. However, this problem can be easily overcome by sub-splitting the solution $G_{11}(x,\xi,\omega)$ into $G_{11b}(x,\xi,\omega)$ and $G_{11p}(x,\xi,\omega)$ defined respectively for $0 < x < L_b$, depicted in blue in Figure I.5, and for $L_b \leqslant x < L$, depicted in red; similarly for $G_{21}(x,\xi,\omega)$.
Therefore, the fundamental problem can be rewritten in the following form

$$\frac{\partial^4 \bar{G}(x,\xi,\omega)}{\partial x^4} + \bar{\bar{B}}(\omega)\bar{G}(x,\xi,\omega) = \bar{f}(x,\xi,\omega) \tag{I.20}$$

where $\bar{G}(x,\xi,\omega) = \left\{G_{11b}(x,\xi,\omega), G_{21b}(x,\xi,\omega), G_{11p}(x,\xi,\omega), G_{21p}(x,\xi,\omega)\right\}^{\mathrm{T}}$, $\bar{f}(x,\xi,\omega) = \left\{\delta(x-\xi), 0, 0, 0\right\}^{\mathrm{T}}$ and

$$\bar{\bar{B}}(\omega) = \begin{pmatrix} B_b(\omega) & -\dfrac{k}{EJ_b} & 0 & 0 \\ -\dfrac{k}{EJ_b} & B_b(\omega) & 0 & 0 \\ 0 & 0 & B_p(\omega) & 0 \\ 0 & 0 & 0 & B_p(\omega) \end{pmatrix}$$

with $B_b(\omega) = (1/EJ_b)\left(-\omega^2\left(\rho A_b - \mathrm{i}\alpha\sqrt{\pi/2\omega}\right) + k\right)$ and
$B_p(\omega) = (1/EJ_p)\left(-\omega^2\left(\rho A_p - \mathrm{i}\alpha\sqrt{\pi/2\omega}\right)\right)$.
The set of Equations (I.20) is equivalent to the homogeneous problem depicted in Figure I.5, right panel, that can be written as

$$\frac{\partial^4 \bar{G}(x,\xi,\omega)}{\partial x^4} + \bar{\bar{B}}(\omega)\bar{G}(x,\xi,\omega) = 0 \tag{I.21}$$

with

$$\bar{G}(x,\xi,\omega) = \left\{G^{I}_{11b}(x,\xi,\omega), G^{I}_{21b}(x,\xi,\omega), G^{II}_{11b}(x,\xi,\omega), G^{II}_{21b}(x,\xi,\omega), \right. \tag{I.22}$$

$$\left. G^{II}_{11p}(x,\xi,\omega), G^{II}_{21p}(x,\xi,\omega)\right\}^{\mathrm{T}} \tag{I.23}$$

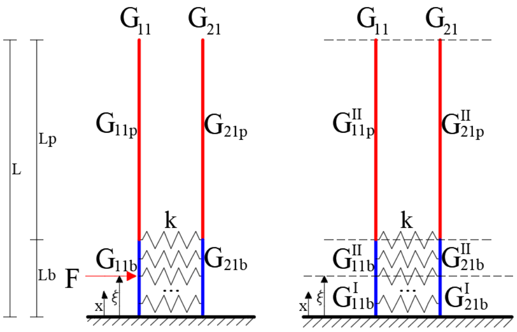

Figure I.5: 1D Euler-Bernoulli model of the fundamental problem. Fundamental problem with an impulsive force applied to a generic section $\xi$ of the left cantilever (left panel), reduction of the fundamental problem to an homogeneous problem (right panel).

and

$$\bar{\bar{B}}(\omega) = \begin{pmatrix} B_b(\omega) & -\dfrac{k}{EJ_b} & 0 & 0 & 0 & 0 \\ -\dfrac{k}{EJ_b} & B_b(\omega) & 0 & 0 & 0 & 0 \\ 0 & 0 & B_b(\omega) & -\dfrac{k}{EJ_b} & 0 & 0 \\ 0 & 0 & -\dfrac{k}{EJ_b} & B_b(\omega) & 0 & 0 \\ 0 & 0 & 0 & 0 & B_p(\omega) & 0 \\ 0 & 0 & 0 & 0 & 0 & B_p(\omega) \end{pmatrix}$$

where the functions $G^I_{11b}(x,\xi,\omega)$ and $G^I_{21b}(x,\xi,\omega)$ are defined for $0 < x < \xi$, the functions $G^{II}_{11b}(x,\xi,\omega)$ and $G^{II}_{21b}(x,\xi,\omega)$ are defined for $\xi \leqslant x < L_b$ and the functions $G^{II}_{11p}(x,\xi,\omega)$ and $G^{II}_{21p}(x,\xi,\omega)$ are defined for $L_b \leqslant x < L$.
The set of Equations (I.21) comprises six coupled differential equations of fourth order needing the following 24 boundary conditions: fixed conditions at $x = 0$, continuity conditions at $x = \xi$ , except for the third derivative of the solutions $G^I_{11b}(x,\xi,\omega)$ and $G^{II}_{11b}(x,\xi,\omega)$ of the bottom-left beam since a concentrated force is applied to section $\xi$ of the left cantilever, continuity conditions at $x = L_b$, and free-end conditions at $x = L$.
All the 24 boundary conditions are reported in detail at the end of this section.

Next, the associated eigenvalues problem [57] for the generic eigenvalue $\lambda$ and the associated eigenvector $\mathbf{v}$ is solved, written as

$$(\bar{\bar{B}}(\omega) - \lambda(\omega)\bar{\bar{I}}_6)\mathbf{v} = 0, \tag{I.24}$$

where $I_6$ is the identity matrix of sixth order; then, the following scaled modal matrix is obtained

$$\bar{\bar{\Psi}} = \begin{pmatrix} \frac{1}{\sqrt{2}} & \frac{1}{\sqrt{2}} & 0 & 0 & 0 & 0 \\ \frac{1}{\sqrt{2}} & -\frac{1}{\sqrt{2}} & 0 & 0 & 0 & 0 \\ 0 & 0 & \frac{1}{\sqrt{2}} & \frac{1}{\sqrt{2}} & 0 & 0 \\ 0 & 0 & \frac{1}{\sqrt{2}} & -\frac{1}{\sqrt{2}} & 0 & 0 \\ 0 & 0 & 0 & 0 & 1 & 0 \\ 0 & 0 & 0 & 0 & 0 & 1 \end{pmatrix} \tag{I.25}$$

It is worth to point out that the eigenvector $\{\frac{1}{\sqrt{2}}, \frac{1}{\sqrt{2}}, 0, 0, 0, 0\}^{\mathrm{T}}$ corresponds to the symmetric vibration mode of the solutions $G^{I}_{11b}(x,\xi,\omega)$ and $G^{I}_{21b}(x,\xi,\omega)$, in which both cantilevers vibrate in phase with the same magnitude, and the eigenvector $\{0, 0, \frac{1}{\sqrt{2}}, \frac{1}{\sqrt{2}}, 0, 0\}^{\mathrm{T}}$ corresponds to the symmetric vibration mode of the solutions $G^{II}_{11b}(x,\xi,\omega)$ and $G^{II}_{21b}(x,\xi,\omega)$, while the eigenvector $\{\frac{1}{\sqrt{2}}, -\frac{1}{\sqrt{2}}, 0, 0, 0, 0\}^{\mathrm{T}}$ corresponds to the skew-symmetric vibration mode of the solutions $G^{I}_{11b}(x,\xi,\omega)$ and $G^{I}_{21b}(x,\xi,\omega)$, in which both cantilevers vibrate out of phase with the same magnitude, and the eigenvector $\{0, 0, \frac{1}{\sqrt{2}}, -\frac{1}{\sqrt{2}}, 0, 0\}^{\mathrm{T}}$ corresponds to the skew-symmetric vibration mode of the solutions $G^{II}_{11b}(x,\xi,\omega)$ and $G^{II}_{21b}(x,\xi,\omega)$.

The modal matrix (I.25) allows for transforming the beam deflection field $\bar{G}$ to the modal coordinates $\bar{q}$, by means of the following relation

$$\bar{G} = \bar{\bar{\Psi}}\bar{q}, \tag{I.26}$$

where $\bar{q} = \left\{q_1, q_2, q_3, q_4, q_5, q_6\right\}^{\mathrm{T}}$ is the vector of the modal coordinates. By substituting (I.26) into (I.20) and premultiplying for $\bar{\Psi}^{\mathrm{T}}$, the Equation (I.20) can be rewritten in modal coordinates, as

$$\frac{\partial^4 \bar{q}(x,\xi,\omega)}{\partial x^4} + \lambda_i(\omega)\bar{\bar{I}}_6\bar{q}(x,\xi,\omega) = 0 \tag{I.27}$$

This is a system of six uncoupled fourth order partial differential equations, whose general solution can be written as

$$\begin{aligned} q_i(x,\xi,\omega) &= a_i \cosh(\sqrt[4]{\lambda_i(\omega)}x) + a_{2i}\sinh(\sqrt[4]{\lambda_i(\omega)}x) + \\ &+ a_{3i}\cos(\sqrt[4]{\lambda_i(\omega)}x) + a_{4i}\sin(\sqrt[4]{\lambda_i(\omega)}x), \end{aligned} \tag{I.28}$$

where $a_i, a_{2i}, a_{3i}$ and $a_{4i}$ for $i = 1, ..., 6$ are integration constants.
Once the solution is known in modal coordinates, it is possible to switch back to the physical coordinates by means of Equation (I.26) and numerically solve the set of 24 boundary conditions for fixed $\xi$ and $\omega$ to obtain the 24 integration constants. The global susceptibility functions of the two cantilevers $G_{11}(x,\xi,\omega)$, for the left loaded cantilever, and $G_{21}(x,\xi,\omega)$, for the right not loaded cantilever, are given by piecewise functions, as

$$G_{11}(x,\xi,\omega) = \begin{cases} G^{I}_{11b}(x,\xi,\omega) & 0 < x < \xi \\ G^{II}_{11b}(x,\xi,\omega) & \xi < x < L_b \\ G^{II}_{11p}(x,\xi,\omega) & L_b < x < L \end{cases} \tag{I.29}$$

$$G_{21}(x,\xi,\omega) = \begin{cases} G^{I}_{21b}(x,\xi,\omega) & 0 < x < \xi \\ G^{II}_{21b}(x,\xi,\omega) & \xi < x < L_b \\ G^{II}_{21p}(x,\xi,\omega) & L_b < x < L \end{cases} \tag{I.30}$$

The fundamental problem can be similarly solved for an impulsive force applied to a different section $\xi$, in order to obtain the 3D matrices $[\mathbf{G}]_{ij}$ for both cantilevers, as explained in section I.2.4.

The boundary conditions for the homogeneous fundamental problem, Equation (I.21), are here reported

- at $x = 0$

$$\begin{aligned} G^{I}_{11b}(0,\xi,\omega) &= \frac{\partial G^{I}_{11b}(x,\xi,\omega)}{\partial x}|_{x=0} = 0 \\ G^{I}_{21b}(0,\xi,\omega) &= \frac{\partial G^{I}_{21b}(x,\xi,\omega)}{\partial x}|_{x=0} = 0 \end{aligned} \tag{A.1}$$

- at $x = \xi$

$$\begin{aligned} G^{I}_{11b}(\xi,\xi,\omega) &= G^{II}_{11b}(\xi,\xi,\omega) \\ \frac{\partial G^{I}_{11b}(x,\xi,\omega)}{\partial x}|_{x=\xi} &= \frac{\partial G^{II}_{11b}(x,\xi,\omega)}{\partial x}|_{x=\xi} \\ \frac{\partial^2 G^{I}_{11b}(x,\xi,\omega)}{\partial x^2}|_{x=\xi} &= \frac{\partial^2 G^{II}_{11b}(x,\xi,\omega)}{\partial x_2}|_{x=\xi} \\ \frac{\partial^3 G^{II}_{11b}(x,\xi,\omega)}{\partial x^3}|_{x=\xi} - \frac{\partial^3 G^{I}_{11b}(x,\xi,\omega)}{\partial x_3}|_{x=\xi} &= 1 \\ G^{I}_{21b}(\xi,\xi,\omega) &= G^{II}_{21b}(\xi,\xi,\omega) \\ \frac{\partial G^{I}_{21b}(x,\xi,\omega)}{\partial x}|_{x=\xi} &= \frac{\partial G^{II}_{21b}(x,\xi,\omega)}{\partial x}|_{x=\xi} \\ \frac{\partial^2 G^{I}_{21b}(x,\xi,\omega)}{\partial x^2}|_{x=\xi} &= \frac{\partial^2 G^{II}_{21b}(x,\xi,\omega)}{\partial x_2}|_{x=\xi} \\ \frac{\partial^3 G^{II}_{21b}(x,\xi,\omega)}{\partial x^3}|_{x=\xi} &= \frac{\partial^3 G^{I}_{21b}(x,\xi,\omega)}{\partial x_3}|_{x=\xi} \end{aligned} \tag{A.2}$$

- at $x = L_b$

$$
\begin{aligned}
G^{II}_{11b}(L_b,\xi,\omega) &= G^{II}_{11p}(L_b,\xi,\omega) \\
\frac{\partial G^{II}_{11b}(x,\xi,\omega)}{\partial x}|_{x=L_b} &= \frac{\partial G^{II}_{11p}(x,\xi,\omega)}{\partial x}|_{x=L_b} \\
EJ_b\frac{\partial^2 G^{II}_{11b}(x,\xi,\omega)}{\partial x^2}|_{x=L_b} &= EJ_p\frac{\partial^2 G^{II}_{11p}(x,\xi,\omega)}{\partial x^2}|_{x=L_b} \\
EJ_b\frac{\partial^3 G^{II}_{11b}(x,\xi,\omega)}{\partial x^3}|_{x=L_b} &= EJ_p\frac{\partial^3 G^{II}_{11p}(x,\xi,\omega)}{\partial x^3}|_{x=L_b} \\
G^{II}_{21b}(L_b,\xi,\omega) &= G^{II}_{21p}(L_b,\xi,\omega), \\
\frac{\partial G^{II}_{21b}(x,\xi,\omega)}{\partial x}|_{x=L_b} &= \frac{\partial G^{II}_{21p}(x,\xi,\omega)}{\partial x}|_{x=L_b} \\
EJ_b\frac{\partial^2 G^{II}_{21b}(x,\xi,\omega)}{\partial x^2}|_{x=L_b} &= EJ_p\frac{\partial^2 G^{II}_{21p}(x,\xi,\omega)}{\partial x^2}|_{x=L_b} \\
EJ_b\frac{\partial^3 G^{II}_{21b}(x,\xi,\omega)}{\partial x^3}|_{x=L_b} &= EJ_p\frac{\partial^3 G^{II}_{21p}(x,\xi,\omega)}{\partial x^3}|_{x=L_b}
\end{aligned}
\tag{A.3}
$$

- at $x = L_b + L_p = L$

$$
\begin{aligned}
\frac{\partial^2 G^{II}_{11p}(x,\xi,\omega)}{\partial x^2}|_{x=L} &= \frac{\partial^3 G^{II}_{11p}(x,\xi,\omega)}{\partial x^3}|_{x=L} = 0 \\
\frac{\partial^2 G^{II}_{21p}(x,\xi,\omega)}{\partial x^2}|_{x=L} &= \frac{\partial^3 G^{II}_{21p}(x,\xi,\omega)}{\partial x^3}|_{x=L} = 0
\end{aligned}
\tag{A.4}
$$

### I.2.6 Analysis of the excitation sources

As final analysis, a study of the QTF dynamic response to distributed forces that are non-deterministic in nature, both in time and space, is presented. In fact, this is the input kind acting on the QTF device during the experiments, in which, as anticipated, two acoustic speakers are used as excitation sources for generating a white, random acoustic field.

The external force per unit length on both the cantilevers have been modelled, in the form of the product of two ergodic, Dirac-Delta-correlated terms, respectively describing the time and space unpredictable behaviour of the external excitation.

The spatial behaviour of the random loading acting on a single cantilever of the QTF can be described, in a discrete form, by the following autocorrelation matrix

$$\bar{\bar{\mathbf{C}}}_{X,i} = \bar{\bar{\mathbf{C}}}_X = S_X^{(0)}\bar{\bar{\mathbf{I}}} \tag{I.31}$$

with $i = 1, 2$, $\bar{\bar{\mathbf{I}}}$ a $N \times N$ identity matrix and the intensity of the spatial part of the stochastic load $S_X^{(0)}$ defined as

$$S_{X,i}(q) = S_X^{(0)} = \frac{< \left|\hat{X}_i(q)\right|^2 >}{L} \tag{I.32}$$

where $q$ indicates the radian spatial frequency, $\hat{X}_i\,(q)$ is the single realization of the spatial stochastic loading acting on each cantilever and is equal to $\sqrt{S_X^{(0)}}\mathrm{e}^{\mathrm{i}\phi_{X,i}(q)}$, with $\phi_{X,i}\,(q)$ random phases uniformly distributed in the range from $-\pi$ to $\pi$. In Equation (I.32), the same intensity of spatial stochastic noise for both cantilevers is assumed, thus $S_{X,1}^{(0)} = S_{X,2}^{(0)} = S_X^{(0)}$.
A unique scalar coefficient $S_T^{(0)}$, indicating the intensity of the temporal part of the stochastic load, is requested to describe the temporal behaviour of the random loading, owing to the simultaneous operation of the excitation sources, equal to

$$S_T\,(\omega) = S_T^{(0)} = \frac{< \left|\hat{T}(\omega)\right|^2 >}{T_p} \tag{I.33}$$

where $T_p$ is the time duration of the stochastic process and $\hat{T}\,(\omega)$ is the single realization of the temporal stochastic loading acting on both cantilevers and is equal to $\sqrt{S_T^{(0)}}\mathrm{e}^{\mathrm{i}\phi_T(\omega)}$, with $\phi_T\,(\omega)$ random phases uniformly distributed in the range from $-\pi$ to $\pi$.
Now, the input power spectral density(PSD) matrix for the entire system can be defined as

$$\bar{\bar{\mathbf{S}}}_{FF} = C_0\bar{\bar{\mathbf{I}}} \tag{I.34}$$

where $\bar{\bar{\mathbf{I}}}$ is a $2N \times 2N$ identity matrix and $C_0$, equal to $S_T^{(0)}S_X^{(0)}$, is only a scaling factor, which does not affect the shape of the system response and the correct evaluation of the quality factor resonator. Therefore, the output power spectral density matrix $\bar{\bar{\mathbf{S}}}_{UU}$ can be obtained as [118]

$$\bar{\bar{\mathbf{S}}}_{UU} = \bar{\bar{\mathbf{G}}}^*\bar{\bar{\mathbf{S}}}_{FF}\bar{\bar{\mathbf{G}}}^T = C_0\bar{\bar{\mathbf{G}}}^*\bar{\bar{\mathbf{I}}}\bar{\bar{\mathbf{G}}}^T \tag{I.35}$$

where

$$\bar{\bar{\mathbf{S}}}_{UU} = \begin{bmatrix} [\mathbf{S}_{U_1U_1}] & [\mathbf{S}_{U_1U_2}] \\ [\mathbf{S}_{U_2U_1}] & [\mathbf{S}_{U_2U_2}] \end{bmatrix}$$

In particular, the matrices of the autoPSD are

$$[\mathbf{S}_{U_1U_1}] = C_0([\mathbf{G}]_{11}^*\,[\mathbf{G}]_{11}^T + [\mathbf{G}]_{12}^*\,[\mathbf{G}]_{12}^T) \tag{I.36}$$

$$[\mathbf{S}_{U_2U_2}] = C_0([\mathbf{G}]_{22}^*\,[\mathbf{G}]_{22}^T + [\mathbf{G}]_{21}^*\,[\mathbf{G}]_{21}^T) \tag{I.37}$$

and, since $[\mathbf{G}]_{11} = [\mathbf{G}]_{22}$ and $[\mathbf{G}]_{12} = [\mathbf{G}]_{21}$ then $[\mathbf{S}_{U_1U_1}]$ is equal to $[\mathbf{S}_{U_2U_2}]$.
By performing the matrix product in Equation (I.35) on the entire chosen temporal frequency range and extracting the discrete autoPSD at the cantilever tip, the following expression is obtained

$$S_{U_iU_i}(L,\omega_k) = C_0\left(\sum_{s=1}^{N}|G_{ii}(L,\xi_s,\omega_k)|^2 + \sum_{s=1}^{N}|G_{ij}(L,\xi_s,\omega_k)|^2\right) \tag{I.38}$$

with $i,j = 1,2$ and $i \neq j$, $k = 1,...,N_k$.

The computed description of the theoretical response requires the estimation of the fluid coefficient $\alpha$ and of the structural coupling stiffness $k$: this can be done by fitting the experimentally measured system response.

# Chapter I.3

# Experimental setup

The experimental setup adopted to completely assess the theoretical model is sketched in Figure I.6. The QTF#S15, used in the experimental test campaign, is a custom QTF having prong length of 9.4 mm, width of 2.0 mm and crystal thickness of 0.25 mm. The prongs are spaced by 1.5 mm, [123, 124], as reported in Table I.1.

The QTF is excited in laboratory air by a stochastic, white acoustic field, generated by two speakers. The QTF response is measured by a LD Vibrometer. The experiments are carried out in static air at ambient temperature and atmospheric pressure: in these thermodynamic conditions the fluid kinematic viscosity is $\nu = 1.48 \times 10^{-5}\,\mathrm{m^2\,s^{-1}}$, while the density $\rho_f = 1.23\,\mathrm{kg\,m^{-3}}$. The setup is composed by: (i) a Polytec OFV-5000 modular LD vibrometer to measure the output response, in several points of the QTF, in terms of displacement and velocity, (ii) two speakers to produce a white acoustic random field for exciting the tuning fork structure, (iii) a Microtech Gefell 1/4" electret-measurement microphone M 370 to measure the acoustic pressure in proximity of the sensor, (iv) a LMS SCADAS Recorder 09 mobile PC based multichannel analyzer platform, running the LMS Test.Lab 14A software suite for generating the input electric signal to drive the speakers, and to acquire and record the time histories of the output responses measured by the vibrometer and the microphone. The adopted speakers' lay-out is sketched in Figure I.6.

The base of the sensor is connected to a stationary frame through two welded tin masses. Therefore, the QTF device is modelled as fixed to the aforementioned frame by a bracket joint positioned on the base cross-section where the welded masses are located. The welded parts of the resonator are excluded from the geometry of the QTF used in the model (see Figure I.7). Being the total length of the base plate equal to 5.1 mm part and excluding the welded part of 1.5 mm, a usable length of the base plate equal to 3.6 mm has been utilized in the calculations and reported as effective dimension in Table I.1.

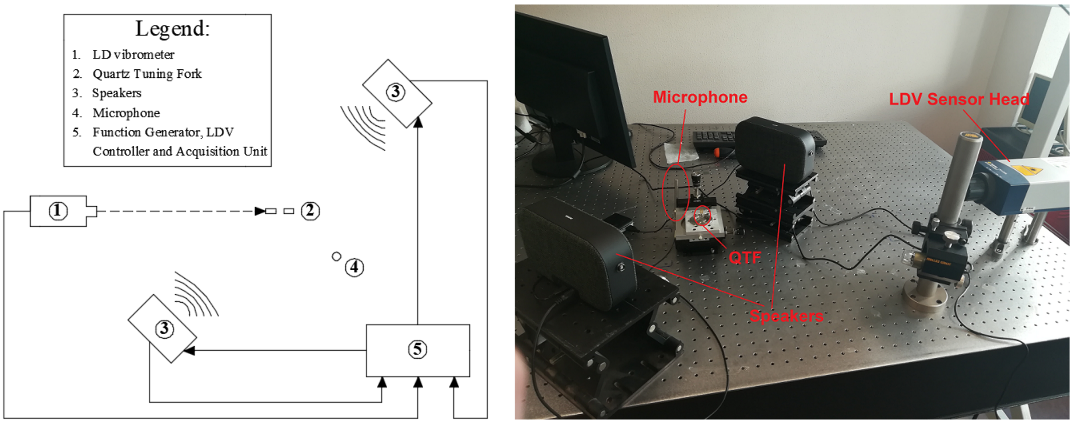


Figure I.6: Schematic representation of the adopted experimental setup (left panel) and the real experimental setup (right panel).

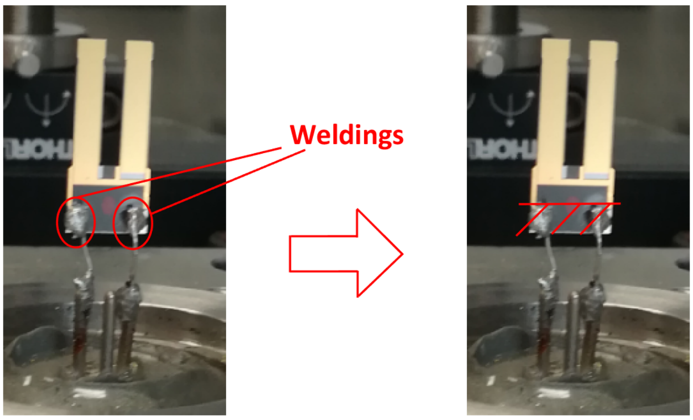


Figure I.7: Real-world constraint of the QTF sensor by two tin weldings (left panel) and adopted constraint by bracket joint (right panel).

# Chapter I.4

# Results and discussion

In Figure I.8, the autoPSD of the tip displacement of one prong is shown, in the frequency range from 14 kHz to 17 kHz, which includes the first in-plane skew-symmetric flexural eigenfrequency of QTF#S15, approximately located at 15.8 kHz [123]. Three different peaks, located at 14.590 kHz, 15.808 kHz and 16.170 kHz were recorded in the experimental response: by performing an in-vacuum 3D finite element (FE) analysis of QTF#S15 by the software COMSOL, the three resonances are related to the first in-plane symmetric flexural mode, the first in-plane skew-symmetric flexural mode (the mode under investigation in this work, named hereafter as QEPAS mode), and to a torsional mode, having even out-of-plane displacement components, respectively. The finite element mode shapes and their relative eigenfrequencies compared with the experimental eigenfrequencies are depicted in the lower part of Figure I.8.

As expected, owing to the adoption of a simple base-frame constraint model and since any fluid-structure interaction in the FE simulation has been considered, a discrepancy between simulated values of FE eigenfrequencies and experimental peak frequencies is achieved. However, such a comparison between experimental outcomes and simplified FE results proves to be useful for identifying the mode type corresponding to each peak frequency included in the considered range. Besides, for the QEPAS mode, the relative error achieves an acceptable value, equal to 4%, due to the pure in-plane nature of such a mode. Such experimental outcomes can be modelled by employing the approach presented in Section I.2 and, thus, performing numerical analyses aimed at computing the PSD of the QTF output response at its cantilever tips. In particular, the Equation (I.38), considering a spectral resolution $\Delta\omega = 2\pi \times 0.4\,\mathrm{rad\,s^{-1}}$, equal to that one used in the experiments, and a spatial discretization $\Delta x = \Delta\xi = 0.31\,\mathrm{mm}$, has been employed. The added mass mainly causes shifts in the flexural in-plane skew-symmetric eigenfrequencies. However, it has been experimentally observed on several QTF geometries operating at very different air pressures (from 750 Torr to 25 Torr), that variations of air pressure surrounding the QTF causes slight shifts of resonance frequency and large variations of the hydrodynamic damping [107]- [119]- [41]. Thus, since the experiment is carried in open air, the added mass can be neglected. In fact, as anticipated, $\mu + \alpha\sqrt{\pi/2\omega} \ll \rho A\,(x)$, where $\mu + \alpha\sqrt{\pi/2\omega}$ is the real part of hydrodynamic function $\Gamma\,(\omega)$.

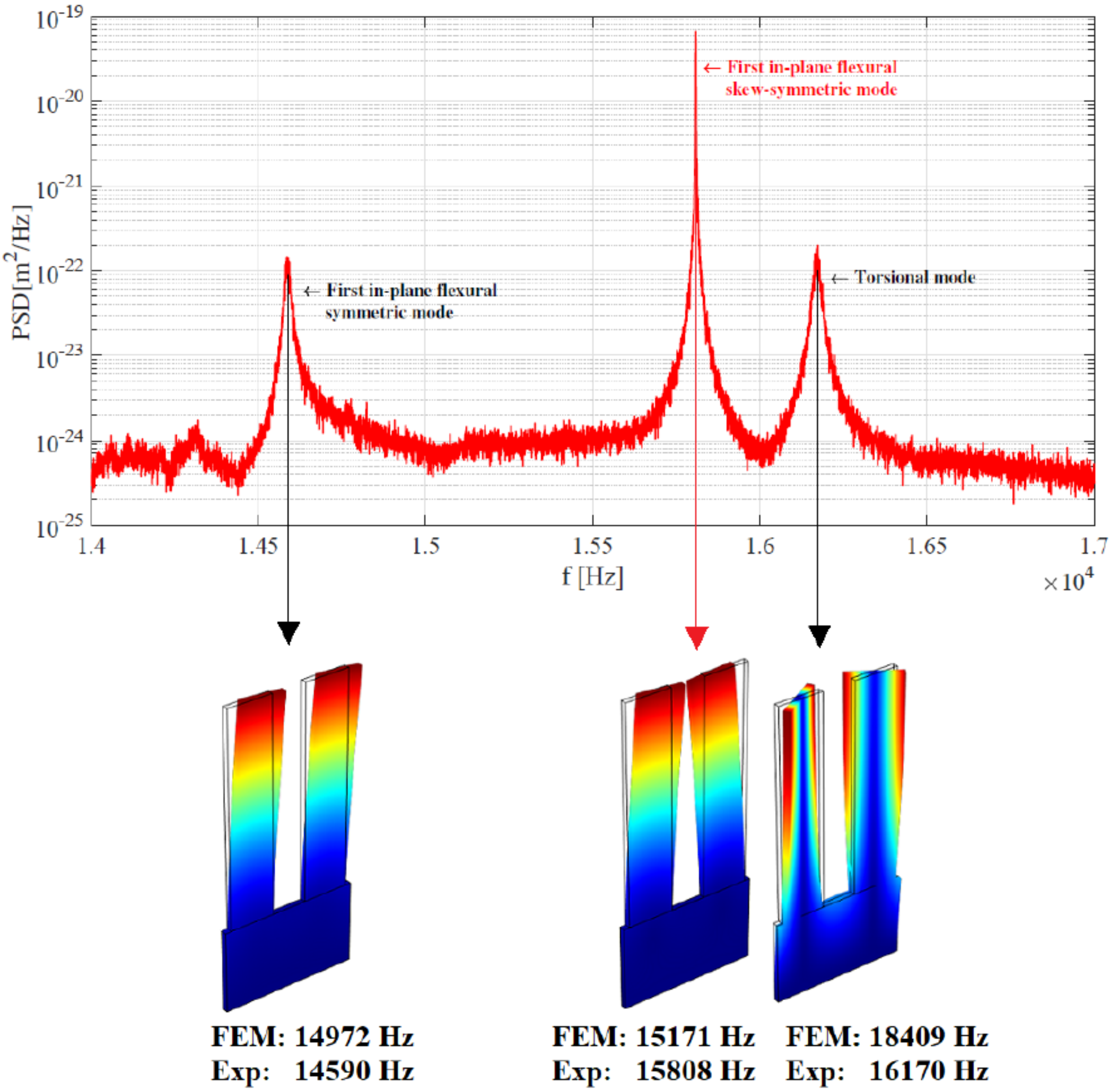


Figure I.8: The experimentally estimated autoPSD of the displacement measured at the tip of one QTF prong and the mode shape of each detected peak.

| Fitting coefficients | $\alpha[\mathrm{Pa\,s}^{3/2}]$ | $k[\mathrm{Pa}]$ |
|---|---|---|
| Values | $2.341 \times 10^{-5}$ | $1.7865 \times 10^{9}$ |

Table I.2: Values of fluid model coefficient and structural coupling stiffness which fit the experimental response.

Then, a least squares fitting for all the remaining parameters can be performed: these include the diffusive-velocity coefficient $\alpha$ and the coupling stiffness $k$; furthermore, the scaling factor $C_0$ for the excitation source has to be properly set. All assumed parameters and fitted values are listed in Table I.2.

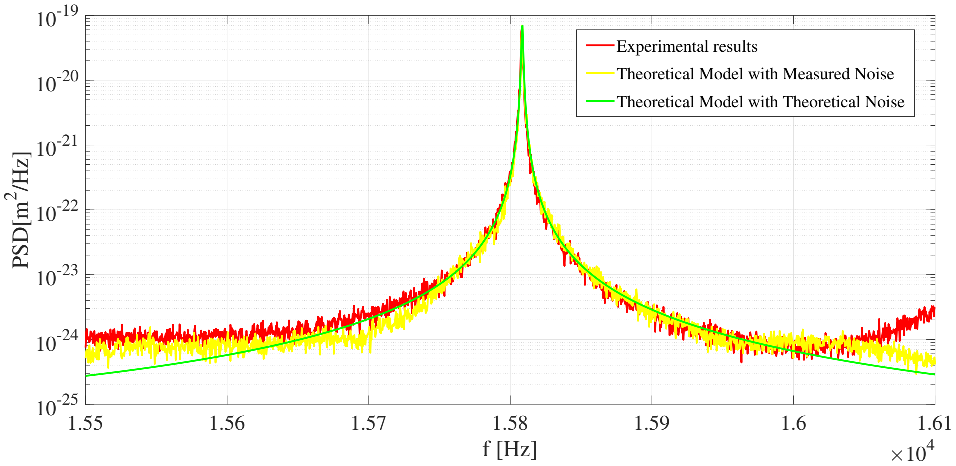


Figure I.9: Comparison between the simulated autoPSD of QTF tip displacement computed by using (i) the theoretically modelled external excitation (green curve) and (ii) the measured noise (yellow curve), and the experimental autoPSD of tip displacement (red curve).

As a result, the theoretical response is reported in Figure I.9. In Figure I.9, in the frequency range from 15.5 kHz to 16.1 kHz, which includes the skew-symmetric eigenfrequency $\omega_{ss}$ of the QEPAS mode, the experimental tip displacement autoPSD (red solid line) is compared to that one resulting from the theoretical model $S_{U_iU_i}(L, \omega)$, computed, by using the Equation (I.38), when accounting for two different descriptions of the external force acting on the QTF cantilevers. In a first case, a perfectly white constant signal (green solid line) has been used as intensity of the temporal part of the external excitation $S_T^{(0)}$ in the Equation (I.38). In a second case, the acoustic pressure signal, measured by the microphone during the tests, has been employed as intensity of the temporal part of the external excitation (yellow solid line).

In Figure I.9, it is possible to conclude that experimental data can be satisfactorily fitted by the proposed theoretical model, with an $R^2$ of the theoretical fitted curve equal to 0.984. The quality factor value can be estimated by measuring the Full Width at Half Maximum (FWHM) value of the resonance curve [118]. As a result, an excellent match between measured and simulated Q-factor values is achieved, with a relative error with respect to the average experimental value, lower than 1%. It is found that

$$Q_{\mathrm{exp}} = \frac{\omega_{ss}}{\Delta\omega} = \frac{15808}{1.205} = 13119 \pm 1182.5$$

$$Q_{\mathrm{th}} = \frac{\omega_{ss}}{\Delta\omega} = \frac{15808}{1.203} = 13140$$

Furthermore, it may be noted that a specific aim of the approach presented in this dissertation is to enhance, in comparison with a traditional fluid-structure interaction FE model, the intelligibility of the physical parameters governing the dynamics of the phenomenon, in order to provide guidelines in designing of QTFs optimized for QEPAS gas sensing application. In particular, the very good agreement between the experimental data and the numerical fitting model confirms that, as assumed when formulating the hydrodynamic function, the system is dominated by a diffusive regime.

Therefore, it is interesting to focus on the analysis of the diffusive-velocity term. To this end, it is worth to point out that for the simple analytical case, shown previously in the Section I.2.2, that is, for a plate vibrating in a viscous fluid in its own plane [4], it is possible to derive the analytical expression of the shear stress $\hat{\tau}_{zy}(x, y, \omega)$, exerted by the fluid on the surface, for a generic time law $u = u(t)$ of the moving surface, as

$$\hat{\tau}_{zy}(x, y, \omega) = (1 - \mathrm{i})\,\tilde{\alpha}\sqrt{\frac{\pi}{2}}\omega^{3/2}\hat{u}(\omega) \tag{I.39}$$

where the coefficient $\tilde{\alpha}$ is equal to $\tilde{\alpha} = \sqrt{\eta_f \rho_f / \pi}$. By applying this result to the case of the QTF#S15, and integrating the shear stress on both sides of the $i$-th cantilever, an analytical estimation $\alpha_L$ for the diffusive-velocity coefficient can be obtained as

$$\alpha_L = 2\tilde{\alpha}\left(\frac{L_b \frac{B}{2} + L_p b}{L}\right) = 1.21 \times 10^{-5}\,\mathrm{Pa\,s^{3/2}} \tag{I.40}$$

This is of the same order of magnitude of the value obtained by the implemented fitting procedure, thus, confirming the consistency of the performed estimation of the value for this parameter. Clearly, on a quantitative level, there exists a discrepancy between the analytical value of the diffusive coefficient $\alpha_L$ and the fitted one, due to edge and 3D effects of the fluid. Employing directly $\alpha_L$ to calculate the quality factor would lead to a potentially poor estimation, but the crucial physical point here is that the fluid dissipation for this case of a very thin tuning fork oscillating asymmetrically is completely characterized by the diffusive regime; identifying the fluid regime is extremely useful as it allows to reduce the number of parameters to fit and, thus, increase the physical intelligibility of the model. A more accurate estimation of $\alpha$ would need a larger analysis on different QTFs geometry in order to understand how this parameter can be related to the shape of the device. This is out of the scope of this thesis, that is, to show the effectiveness of the proposed approach to model the dynamic response.

Now, another important parameter in the proposed model is the coupling stiffness $k$ that is needed to model the structural coupling between the two prongs due to the underlying base plate of QTF device, the latter, in turn, gives rise to the skew-symmetric in-plane flexural QEPAS mode. It is worth pointing out that, by modelling the base plate as infinitely rigid body and studying the bending dynamics of each single fixed-free prong as a single Euler-Bernoulli beam, a single first in-plane flexural mode is obtained instead of a pair of symmetrical and skew-symmetrical ones. To account for both the modes, it is crucial to consider the structural coupling. Specifically, it is worth pointing out that frequency position of the skew-symmetric peak depends on $k$. While the value of $k$ has been previously estimated by fitting the experimentally measured system response, now, in order to enhance the physical intelligibility of the model, an expression to calculate a physical value of $k$ is proposed. The elastic behaviour of the base plate can be modelled as a continuous distribution of beams having infinitely small cross-section. In this case, all the beams will be subjected to only normal stresses, as depicted in Figure I.10 and the axial stiffness of each beam can be calculated as

$$d\kappa = \frac{Eh}{g}dx \tag{I.41}$$

where $g$ is the distance between the two cantilevers' axes, equal to $B/2$, as represented in Figure I.10. Thus, the coupling stiffness per unit length $k = d\kappa/dx$ can be considered expressed by

$$k = \frac{Eh}{g} \tag{I.42}$$

which decreases if the gap between the cantilevers is increased, as also confirmed in [108].

By using Equation (I.42), $k$ is equal to $6 \times 10^9\,\mathrm{N\,m^2}$, which is almost three times larger than the fitted value, as reported in Table I.2. However, it should be considered that the corresponding skew-symmetric mode frequency is located at 16.694 kHz (see Figure I.11), with a relative error of 5.6 % when compared to the actual frequency value equal to 15.808 kHz. This allows to conclude that even a rough estimation of the coupling stiffness $k$ leads only to a small error on the QEPAS mode frequency, implying that the expression (I.42) can be suggested for improving the model predictivity. By using the estimated value of $k$, the frequency peak position slightly increases, but the shape and the FWHM value of the resonance curve remain almost the same, as shown in Figure I.11, leading to a Q-factor characterized by an acceptable relative error of 4.3%, with respect to the experimental value $Q_{\mathrm{exp}} = 13119$, that is

$$Q_{\mathrm{th}}\big|_{k=Eh/g} = \frac{\omega_{ss}}{\Delta\omega} = \frac{16694}{1.22} = 13684 \approx Q_{\mathrm{exp}}$$

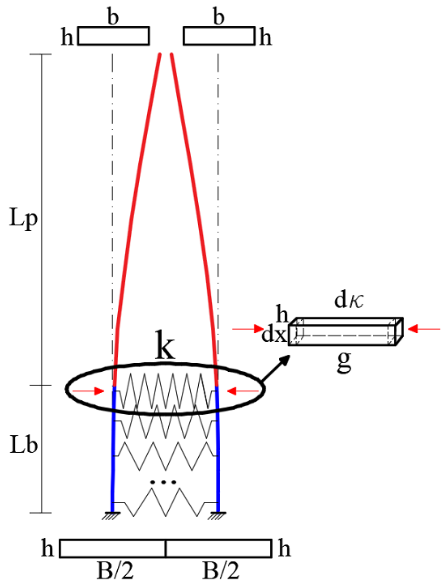


Figure I.10: Modelling of the elastic behaviour of the QTF inferior plate as a distribution of linear springs all subjected to only axial stress.

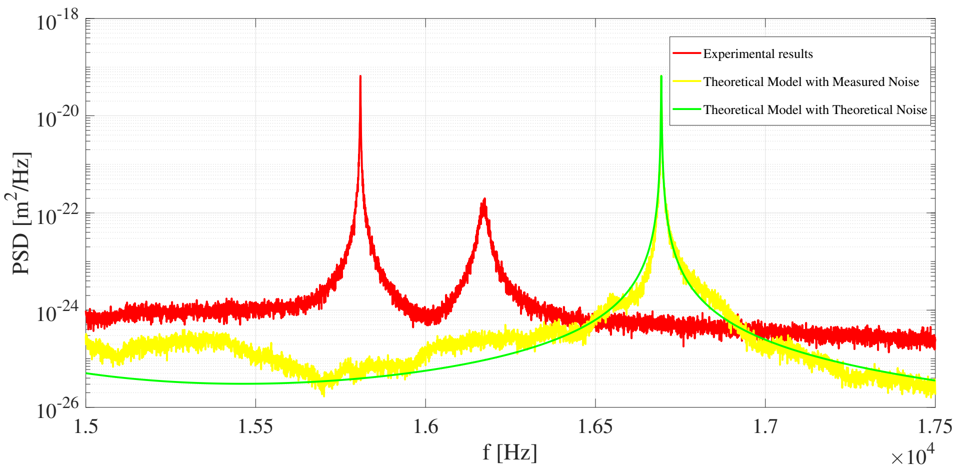


Figure I.11: Comparison between the simulated autoPSD of QTF tip displacement computed, in the case $k = Eh/g$, by using (i) the theoretically modelled external excitation (green curve) and (ii) the measured noise (yellow curve), and the experimental PSD of tip displacement (red curve).

### I.4.1 Estimation of the hydrodynamic function's coefficients by computational fluid dynamics finite element simulations.

Here, the values of coefficients $c$, $\alpha$, and $\mu$ of hydrodynamic function $\Gamma(\omega)$, in Equation (I.9), are estimated by analysing, through computational fluid dynamics (CFD) simulations, the 2D unsteady Stokes' flow induced by the harmonic skew-symmetric oscillation, along the $y$-axis, of two identical rigid bodies, shaped as the prong cross-sections and immersed in an unbounded viscous incompressible medium. Specifically, the fluid flow is considered 2D, since, as anticipated, the motion of cross-sections is hypothesized to occur in their $yz$-plane and the fluid velocity component along the cantilevers' $x$-axes is assumed negligible.

The considered range of time frequencies is $\mathrm{f} \in [10^3, 10^5]$ Hz, in which five simulations per decade are performed. Each simulation is executed until the steady state of periodic regime is reached. The geometry of the computational domain along with the imposed boundary conditions is represented in Figure I.12. By taking into account the geometric symmetry of the problem with respect to the motion $y$-direction and the further fluid dynamic symmetry with respect to the $z$-axis, due to the specific, considered out of phase oscillation, only one quarter of the whole domain is simulated. No-slip boundary conditions at the fluid–body interface and at the right edge of the computational domain are enforced; symmetry conditions are, thus, set along the left and bottom edges, while an open boundary condition is imposed at the top edge, as reported in Figure I.12.

The problem is simulated by the finite element solver COMSOL Multiphysics, adopting a modelling technique based on the Laminar Flow (spf) and Moving Mesh (ale) physics interfaces. In particular, the P2+P1 discretization is used, that is, piecewise quadratic and linear interpolation, respectively, for velocity and pressure, combined with the default streamline diffusion and crosswind diffusion consistent stabilization methods, and with an extremely fine, physics-controlled moving mesh.

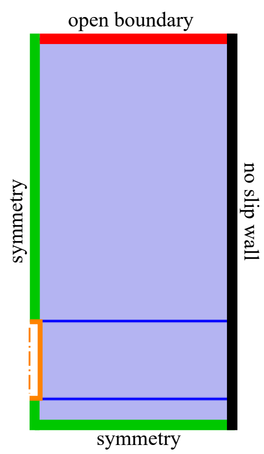


Figure I.12: Computational domain along with moving mesh regions and boundary conditions.

| Fitting coefficients | $c[\mathrm{Pa\,s}]$ | $\alpha[\mathrm{Pa\,s}^{3/2}]$ | $\mu[\mathrm{Pa\,s}^2]$ |
|---|---|---|---|
| Values | $9.88 \times 10^{-5}$ | $1.62 \times 10^{-5}$ | $1.36 \times 10^{-7}$ |

Table I.3: Values of fluid model coefficients which fit the CFD numerical results.

For each considered frequency value, by integration on the fluid–body interface, the time history of the force exerted by the fluid on the moving cross-section is computed. In particular, the $y$-component of these forces allows to extract the amplitude and the phase lag of the hydrodynamic function $\Gamma(\omega)$ with respect to the imposed displacement by Equation (I.8). It is worth pointing out that, in case of unsteady Stokes' flow and, thus, oscillations of small amplitude, owing to the linearity of the problem, the computed force time histories are harmonic signals at the same radian frequency $\omega$ of the imposed movement.

The requisite values of coefficients $c$, $\alpha$, and $\mu$, are collected in Table I.3 and estimated by implementing a specific nonlinear fitting strategy of achieved numerical results, relying on the approximate expression Equation (I.9) of the hydrodynamic function $\Gamma(\omega)$. By adopting a purely diffusive model of the imaginary part of the hydrodynamic function, i. e. by assuming $c = 0\,\mathrm{Pa\,s}$, the sole diffusive-velocity coefficient $\alpha$ is estimated to be equal to $1.70 \times 10^{-5}\,[\mathrm{Pa\,s}^{3/2}]$. The observed discrepancy between the experimental value of the coefficient and that obtained by the numerical procedure here reported can be related to the ensemble of effects which have been neglected, as well as to the measurements' uncertainties.

In Figure I.13, the real and the imaginary parts of the hydrodynamic function $\Gamma(\omega)$ are shown, evaluated by the approximate expression Equation (I.9) and computed by using the fitted values of the coefficients $c$, $\alpha$, and $\mu$, collected in Table I.3. By even representing the single summands $\mu$, $\alpha\sqrt{\pi/(2\omega)}$, and $c/\omega$, and highlighting the QEPAS mode frequency location, it is clearly possible to see, from the analysis of imaginary part, that the linear viscous damping term is basically negligible, with respect to the importance of the diffusive-velocity term, as expected, given the small difference between the $\alpha$ fitted values with $c \neq 0\,\mathrm{Pa\,s}$ or $c = 0\,\mathrm{Pa\,s}$. Given, moreover, the negligible importance of mass adding, as also expected and testified by the experimental results presented in Refs. [107, 119]- [41], it is straightforward to conclude that the two conditions $c\omega^{-1} \ll \alpha\sqrt{\pi/2\omega}$ and $\mu + \alpha\sqrt{\pi/2\omega} \ll \rho A(x)$ describe the purely $\alpha$-driven regime which characterizes the QTF forced vibration at the QEPAS frequency.

It is useful to stress that only one hydrodynamic function is sufficient to describe the hydrodynamic coupling between the two cantilevers vibrating at the QEPAS resonance frequency. In fact, while in Ref. [57], it is proven that two independent hydrodynamic functions are needed to thoroughly identify the system dynamics in each possible coupling condition, in case of skew-symmetric vibration, here under investigation, given the same motion amplitude of the bodies, only one function describes the specific situation, which corresponds to a simple linear combination of the two above recalled independent functions. Therefore, $\alpha$-values here estimated account for the hydrodynamic coupling existing between the two oscillating cantilevers.

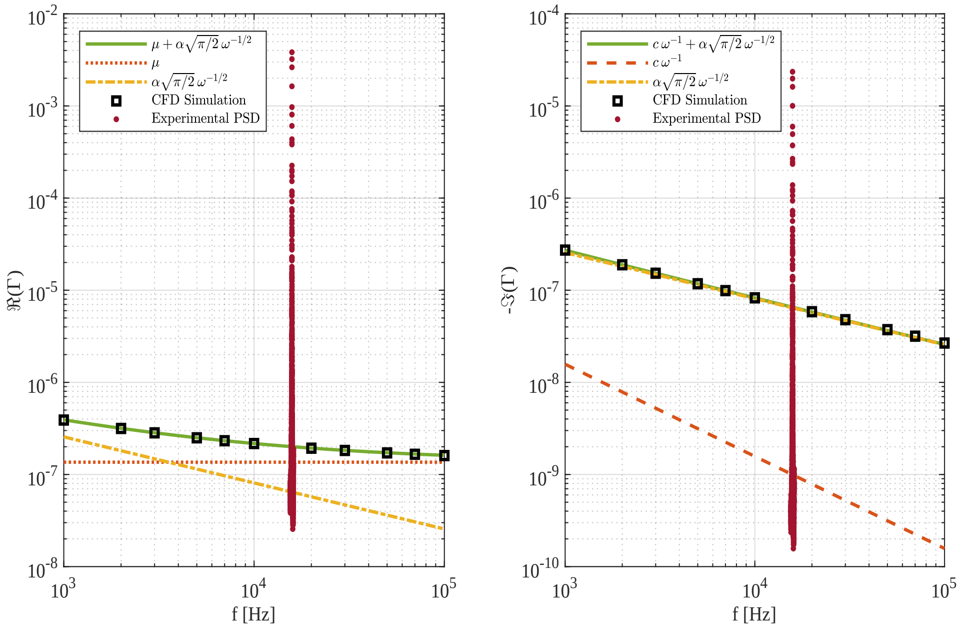


Figure I.13: Real and imaginary parts of hydrodynamic function $\Gamma(\omega)$. Comparison between approximate expression (I.9) evaluated with fitted coefficients collected in Table I.3 (solid line) and CFD numerical results (squared markers). Single summands $\mu$ (dotted line), $\alpha\sqrt{\pi/(2\omega)}$ (dotted-dashed line), and $c/\omega$ (dashed line) of real and imaginary part are represented to elucidate their relative importance. The experimentally estimated PSD (solid dots) is reported to highlight the frequency location of the first QTF skew-symmetric in-plane flexural mode.

## I.4.2 Estimation of the system modal parameters by operational modal analysis

Here, the modal parameters, such as eigenfrequencies, damping ratios and mode shapes, of the in-plane vibrations of the system, are obtained by performing an operational modal analysis (OMA), in order to validate the theoretical model. Modal parameter identification is used to identify those parameters of the model which describe the dynamic properties of a vibration system. Classical modal parameter extractions usually require measurements of both the input force and the resulting response in laboratory conditions. However, cases exist where it is rather difficult to apply a deterministic artificial force, such as the case of a microresonator analysed in this work, or it is very expensive and impracticable to generate and measure actual excitation, such as large structures (for example bridges, offshore platforms, and wind turbines), and where one has to rely upon available ambient excitation sources [125–127]. In this cases, Operational Modal Analysis is generally used, where only the response data need to be measurable, while the actual loadings are not measured. Hence, the system identification is based on output-only data and, for this reason, OMA is also referred to as Output-only Modal Analysis.
Frequency-domain OMA methods require output cross-spectra as primary data. In fact, it is possible to show that, under the assumption of white noise input, the cross-power spectral density functions between responses can be used to estimate modal parameters from output-only data instead of frequency response functions (FRF) in frequency-domain modal identification. It is well known that the modal decomposition of a FRF matrix $\bar{\bar{\mathbf{G}}}(\omega) \in \mathbb{C}^{l\times m}$, indicating with $l$ the number of outputs and $m$ the number of inputs, can be written as [125]

$$\bar{\bar{\mathbf{G}}}(\omega) = \sum_{i=1}^{n} \frac{\{v_i\} < l_i^{\mathrm{T}} >}{\mathrm{i}\omega - \lambda_i} + \frac{\{v_i^*\} < l_i^{\mathrm{H}} >}{\mathrm{i}\omega - \lambda_i^*} \tag{I.43}$$

where $n$ is the number of modes, $*$ indicates complex conjugation of a matrix, H indicates the complex conjugation and transposition (Hermitian) of a matrix, $\{v_i\} \in \mathbb{C}^l$ are the mode shapes, $< l_i^{\mathrm{T}} > \in \mathbb{C}^m$ are the modal participations factors, and $\lambda_i$ are the system poles, which occurr in complex-conjugated pairs and are related to the eigenfrequencies $\omega_i$ and damping ratios $\xi_i$ as

$$\lambda_i, \lambda_i^* = -\xi_i\omega_i \pm \mathrm{i}\sqrt{1-\xi_i^2}\omega_i$$

The input power spectral density matrix $\bar{\bar{\mathbf{S}}}_{FF} \in \mathbb{C}^{m\times m}$ and output power spectral density matrix $\bar{\bar{\mathbf{S}}}_{UU} \in \mathbb{C}^{l\times l}$ of a system represented by the FRF matrix $\bar{\bar{\mathbf{G}}}(\omega)$ are related by the following well-known input-output relationship

$$\bar{\bar{\mathbf{S}}}_{UU} = \bar{\bar{\mathbf{G}}}(\omega)\bar{\bar{\mathbf{S}}}_{FF}\bar{\bar{\mathbf{G}}}^{\mathrm{T}}(\omega) \tag{I.44}$$

In case of operational data, the output spectra represent the only available data. Thus, the knowledge of the input is replaced by the assumption that the inputs are uncorrelated white noise sequences. A property of white noise is that it expresses constant power at each frequency of its spectrum. Hence $\bar{\bar{\mathbf{S}}}_{FF}$ is independent of frequency in Equation (I.44). The modal decomposition of the output spectrum matrix is obtained by inserting Equation (I.43) into Equation (I.44) and converting the result into the partial fraction form

$$\bar{\bar{\mathbf{S}}}_{UU} = \sum_{i=1}^{n} \frac{\{v_i\} < g_i >}{\mathrm{i}\omega - \lambda_i} + \frac{\{v_i^*\} < g_i^* >}{\mathrm{i}\omega - \lambda_i^*} + \frac{\{g_i\} < v_i >}{-\mathrm{i}\omega - \lambda_i} + \frac{\{g_i^*\} < v_i^* >}{-\mathrm{i}\omega - \lambda_i^*} \tag{I.45}$$

where $< g_i > \in \mathbb{C}^l$ are the so-called operational reference factors. Their physical interpretation is not so obvious as they are a function of all modal parameters of the system and the constant input spectrum matrix. Note that the order of the power spectrum model is twice the order of the FRF model. The goal of operational modal analysis is to identify the right hand side terms of Equation (I.45) based on measured output data, pre-processed as output spectra [125, 126]. In this thesis, the so-called weighted correlogram, a non-parametric spectrum estimate, has been used, since it has been proved to have some specific advantages in a modal analysis context [126, 129–131]. First the correlations have to be estimated

$$R_i = \frac{1}{N} \sum_{k=0}^{N-1} u_{k+i} u_k^{\mathrm{T}} \tag{I.46}$$

with $k$ the sample index, $i$ the correlation sample index (also referred to as time lag), $N$ the total number of samples, and $u_k \in \mathbb{R}^l$ the measured output signal. The weighted correlogram is the DFT of the weighted estimated correlation in Equation (I.46)

$$S_{uu}(\omega) = \sum_{k=-L}^{L} w_k R_k \exp^{-\mathrm{i}\omega k \Delta t} \tag{I.47}$$

where $w_k$ denotes the used weighting time window and $L$ is the maximum number of time lags at which the correlations are estimated. This number is typically much smaller than the number of data samples to avoid the greater statistical variance associated with the higher lags of the correlation estimates.
The weighted correlogram has the following advantages:

- It is sufficient to compute the so-called half spectra which are obtained by using only the correlations having a positive time lag in Equation (I.47):

  $$S_{uu}^{+}(\omega) = \frac{w_0 R_0}{2} + \sum_{k=0}^{L} w_k R_k \exp^{-\mathrm{i}\omega k \Delta t} \tag{I.48}$$

  where the relation between the half spectra in Equation (I.48) and the full spectra (I.47) is

  $$S_{uu}(\omega) = S_{uu}^{+}(\omega) + (S_{uu}^{+}(\omega))^{\mathrm{H}} \tag{I.49}$$

  It can be shown (see for instance [129, 131]) that the modal decomposition of these half spectra only consists of the first two terms in Equation (I.45)

  $$S_{UU}^{+} = \sum_{i=1}^{n} \frac{\{v_i\} < g_i >}{\mathrm{i}\omega - \lambda_i} + \frac{\{v_i^*\} < g_i^* >}{\mathrm{i}\omega - \lambda_i^*} \tag{I.50}$$

The advantage in modal analysis is that models of lower order can be fitted without affecting the quality.

- Under the assumption of uncorrelated white noise inputs, the output correlations are equivalent to impulse responses. So, just like in impact testing, it seems logical to apply an exponential window to the correlations before computing the DFT in Equation (I.47). The exponential window reduces the effect of leakage and the influence of the higher time lags, which have a larger variance. Moreover, the application of an exponential window to impulse responses or correlations is compatible with the modal model and the pole estimates can be corrected. This is not the case when a Hanning window is used: such a window always leads to biased damping estimates.

In Figure I.14 and I.15 amplitude and phase of displacement full spectrum and displacement half spectrum are shown, respectively, measured at the tip of the QTF in the frequency range from 15.5kHz to 16.1kHz, which includes the eigenfrequency of the QEPAS mode. The full spectrum, preprocessed as said, has been

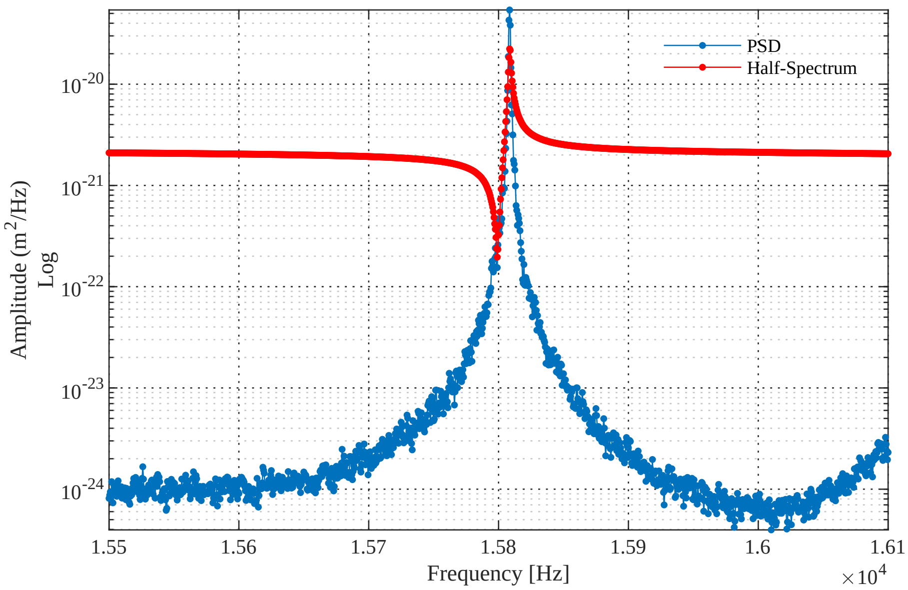


Figure I.14: Comparison between amplitude of displacement half-spectrum (in red) and amplitude of displacement full-spectrum (in blue), measured at the tip of the QTF.

used as experimental outcome to fine tune the theoretical model. A more traditional non-parametric spectrum estimate is the weighted averaged periodogram (also known as modified Welch's periodogram) [128]. A thorough discussion and a comparison between the correlogram and periodogram estimates can be found in [129–131].

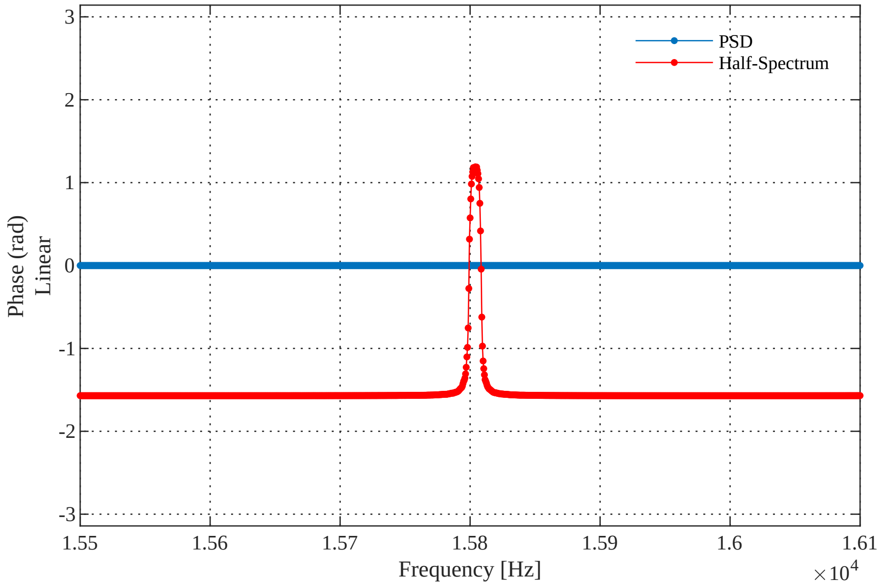


Figure I.15: Comparison between phase of displacement half-spectrum (in red) and phase of displacement full-spectrum (in blue), measured at the tip of the QTF.

After pre-processing output data into output spectra, the modal model has to be identified. By comparing Equation (I.50) with Equation (I.43), it is clear that FRFs and half spectra can be parameterised in exactly the same way. By consequence, the same modal parameter estimation methods can be used in both cases. PolyMAX (Polyreference Least Square Complex Frequency Domain) is such a method [126]. It allows one to build up a stabilisation diagram, assuming subsequently an increasing number of poles [132]. The stabilisation diagram gives a strong indication of the number of present physical modes and allows the selection of the best estimates for the corresponding physical poles. The interpretation of the stabilisation diagram yields, indeed, a set of stable poles and, hence, a set of eigenfrequencies and damping ratios and the corresponding operational reference factors.

Then, the mode shapes can be found, at last, by solving in a linear least square sense Equation (I.50), rephrased as

$$S_{UU}^{+} = \frac{LR}{\mathrm{i}\omega} + \sum_{i=1}^{n} \frac{\{v_i\} < g_i >}{\mathrm{i}\omega - \lambda_i} + \frac{\{v_i^*\} < g_i^* >}{\mathrm{i}\omega - \lambda_i^*} + \mathrm{i}\omega UR \tag{I.51}$$

in which all the present terms are $l \times m$ matrices, with $m$ the number of outputs selected as references and, in particular, LR, UR, respectively the lower and upper operational residuals, have been introduced to model the influence of the out-of-band modes in the considered frequency range. Since, during the experimental test campaign, single output acquistions have been performed, every single ac-

quired point is itself a reference and $m$ is equal to 1. An interesting and detailed discussion on the selection of the reference output can be found in [130].
A validation phase follows the identification, to evaluate the quality of the estimated modal model, by using validation tools, among which extremely powerful is the Modal Assurance Criterion (MAC) [132]. The MAC can be used to compare different sets of estimated mode shapes or to investigate the validity of the estimated modes belonging to a given set. In this last case it is generally referred to as autoMAC. It is useful to recall that when two estimates of the same physical mode are considered, the corresponding MAC value will approach the unity, because of the orthogonality condition of the mode shapes. The MAC value calculated considering two estimates of two different physical modes will be conversely low.
In the following, the results obtained by OMA-processing the time data acquired during the test campaign are discussed. By the experimental setup previously described in chapter I.3, a white noise acoustic field is generated by two speakers, in order to be as close as possible to OMA hypotheses, and the response of the structure is measured in seven points of one prong of the QTF by a LD vibrometer. The layout of these points is shown in Figure I.16. The weighted

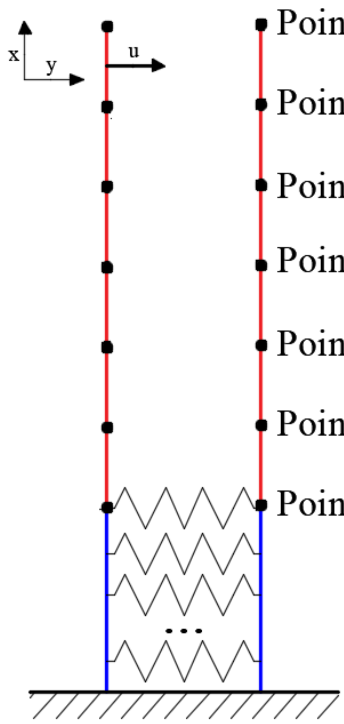


Figure I.16: Schematic layout of the measured points. All the points are equally spaced along the prong.

correlogram and the PolyMAX technique have been used, both implemented in the LMS Test.Lab Structure Analysis software. The time data, recorded at a maximum sampling frequency of 25 kHz, have been pre-processed to have the frequency resolution of the estimated output spectra equal to 0.5 Hz. For spectrum estimation, a maximum number of positive time lags equal to 102400 and a 1 % exponential window are employed. Regarding processing of output spectra aimed at modal parameter estimation, the frequency band used to build up the stabilisation diagram has been that from 12 kHz to 18 kHz, which correspond to the same frequency range of speaker generation of the white noise acoustic field. In Figure I.17 the stabilisation diagram obtained with the PolyMAX method is shown. The physical stable poles are related, from left to right, to the first in-plane symmetric flexural mode at 14.59 kHz, to the QEPAS mode at 15.808 kHz, and to a torsional mode at 16.170 kHz. The computed MAC values for the three

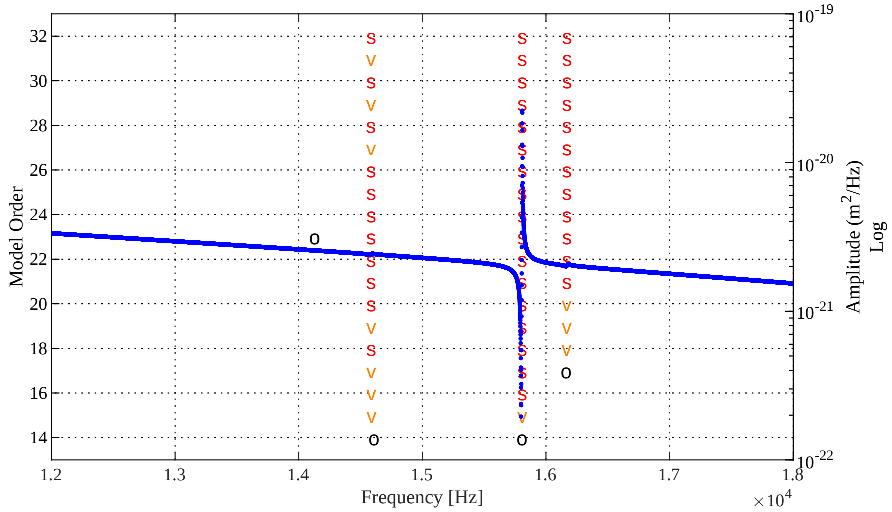


Figure I.17: Stabilisation diagram computed by applying the PolyMAX method to the displacement half-spectrum of the tip of the QTF.

identified modes in the stabilisation diagram, depicted in Figure I.18, allow to conclude that the identified mode sets can be considered autonomously validated. From the PolyMAX estimation of the poles, it is possible to extract the damping factor $\xi$ of the QEPAS mode for the displacement spectra at different points of the analysed prong of the QTF and, by recalling that $\xi = 1/(2Q)$, to obtain the corresponding quality factor. The results are shown in Table I.4.

In Table I.4, the quality factor of point 1, at the tip of the QTF, ends to be very similar to that obtained with the theoretical model and calculated with the FWHM method, equal to 13140, proving the correct implementation of OMA technique as identification method and the robustness and quality of the theoretical model. The low quality factor values of the last three points is due to low signal-to-noise ratio of these points, very close to the common base of the QTF, which is almost stationary with respect to the prong motion.

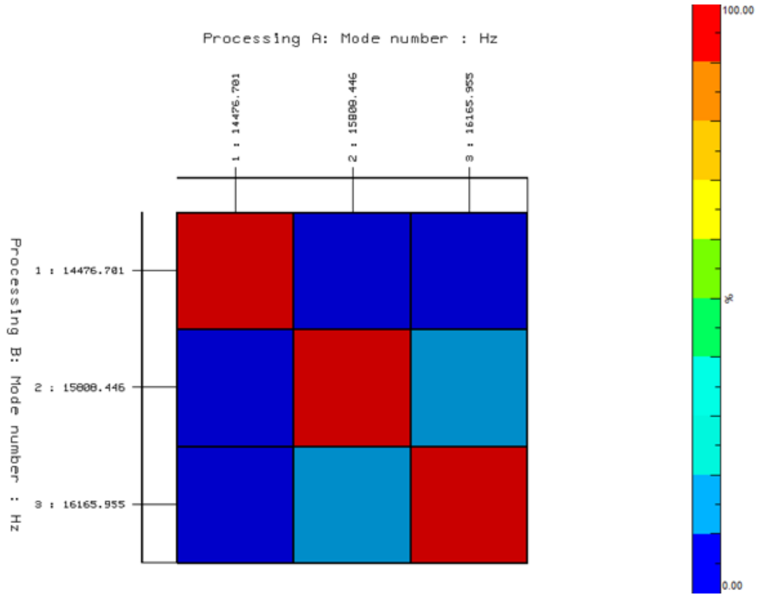


Figure I.18: MAC for the three identified modes in the stabilisation diagram.

| Points | $\xi$ | $Q$ |
|---|---|---|
| Point 1 | $3.66336e^{-5}$ | 13648.68 |
| Point 2 | $3.96944e^{-5}$ | 12596.23 |
| Point 3 | $3.59006e^{-5}$ | 13927.34 |
| Point 4 | $3.73249e^{-5}$ | 13395.88 |
| Point 5 | $4.41821e^{-5}$ | 11316.8 |
| Point 6 | $4.05295e^{-5}$ | 12336.69 |
| Point 7 | $5.25743e^{-5}$ | 9510.35 |

Table I.4: Damping factors and quality factors of the QEPAS mode for the seven points acquired in the experimental test campaign. The numbering of the points refers to Figure I.16.

Finally, the QEPAS mode shape of the studied prong of the QTF has been reconstructed and is plotted in Figure I.19.

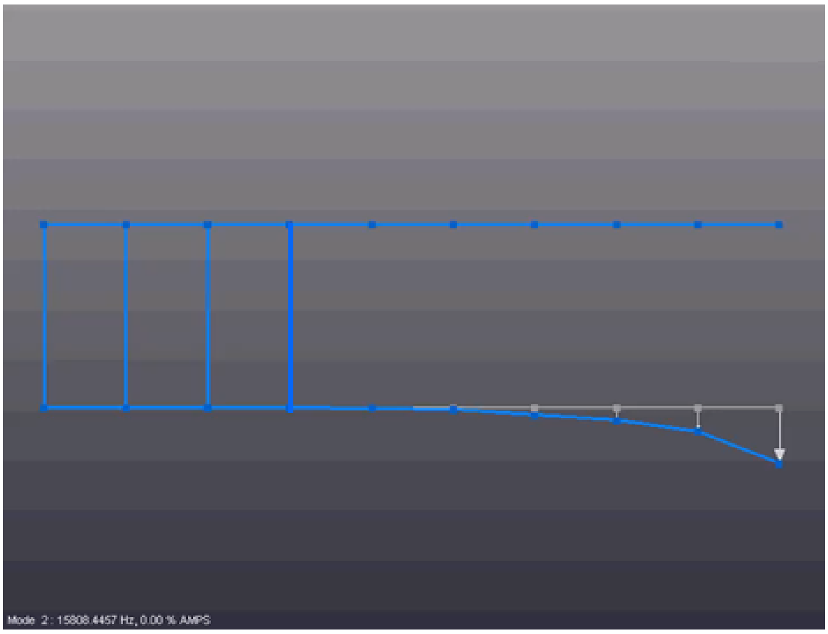


Figure I.19: QEPAS mode shape of a single prong of the QTF, reconstructed with the PolyMAX estimation technique.

# Chapter I.5

# Conclusions

In this first part of the thesis, a theoretical-experimental framework, relying on Boundary Element Methodology (BEM), is developed to study the dynamic analysis of a quartz tuning fork (QTF) vibrating in a fluid environment. In detail, the quartz tuning fork has been modelled as a pair of Euler-Bernoulli cantilevers coupled by distributed linear springs with constant stiffness. The model takes into account the interaction between the QTF and the surrounding fluid. This is crucial for an accurate estimation of the quality factor of the first skew-symmetric in-plane flexural vibrational mode, corresponding to the specific mode at which the QTF is excited when employed as resonator in a QEPAS sensor. To this aim, an innovative analytical model of the fluid-structure interaction has been proposed, accounting for the inertial, the purely viscous and the diffusive terms. Due to the system linearity, the force exerted by the liquid on the body is the sum of these three contributions. Finally, the dynamic analysis of the problem has been reduced to the solution of an integral equation based on a properly defined Green's function, which takes into account the aforementioned terms, related to the fluid, and the elasticity of the two coupled beams. In comparison with a Finite Element approach, such an integrated strategy offers a high computational efficiency and the possibility of understanding how each parameter of the system influences the overall dynamic response.

In order to tune the model, a proper vibro-acoustic experimental setup has been implemented: the in-plane flexural vibration of a custom QTF immersed in air and excited by a white noise source have been acquired. The experimental data have been perfectly fitted by means of the proposed BEM-based model in a range of frequency close to the flexural mode typically excited in the QEPAS application, i.e. the first in-plane skew-symmetric flexural mode. By corroborating the theoretical model with experimental results, the effect of the diffusive-velocity term, originally derived by Landau [4] for the in-plane motion in a viscous fluid of an infinite half-space, and the effect of the structural coupling term have been analysed and discussed. The first one is crucial to correctly estimate the system damping and, thus, the Q-factor; the second one, related to the structural coupling, is necessary to couple the two prongs and, thus, to be able to observe the skew-symmetric in-plane flexural mode. The value of the structural coupling stiffness affects only the position of the skew-symmetric peak and can be obtained by fitting the experimental data; alternatively, an approximate estimation of this value, based on theoretical considerations, leads to a still relatively good assessment of the skew-symmetric frequency and can make more predictive the model. However, the proposed methodology requires an experimental fit for retrieving fluid coefficients and, in particular, for the $\alpha$ parameter, which marks the diffusive regime that governs the fluid-solid interaction. At the same time, it is crucial to underline that the proposed approach provides direct insights on the overall performance of the QTF and, more generally, can be considered a reliable procedure to analyse the fluid-structure interaction of a generic micro-electrical-mechanical device.

# Part II

# FSI nonlinear problem: Nonlinear inextensible plate in low speed airflow

# Chapter II.1

# Introduction

Flutter is known as an aeroelastic instability, which occurs in a solid elastic structure interacting with a flow of gas or fluid at a definite frequency where energy is extracted from the stream by the motion of the structure and consists of violent vibrations of the structure with rapidly increasing amplitudes [5]. Such an event can occur in somewhat flexible structures, such as airplane wings, telegraph wires, bridges, and buildings and can rapidly lead to system failure [8–10, 133]. Some examples of fluttering systems are shown in Figures II.1 and II.2.

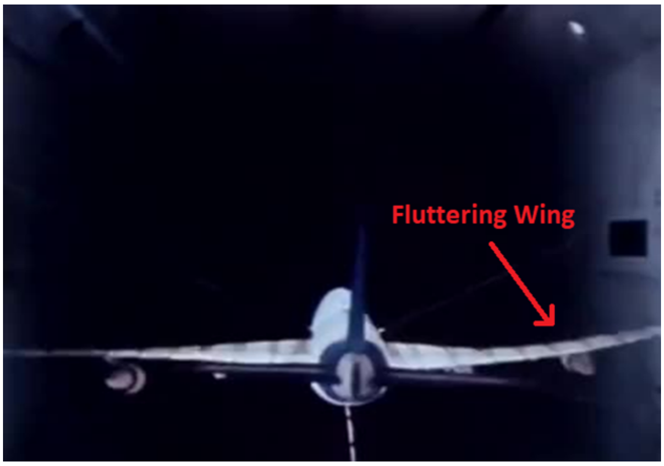


Figure II.1: An example of fluttering wing in a wind tunnel, Test to Destruction: "Aeroelasticity Matters", 1981 NASA Langley Wind Tunnel Tests

In a linear system, flutter point is the point at which the structure is undergoing simple harmonic motion (zero net damping) and so any further decrease in net damping will result in a self-oscillation and eventual failure; in a nonlinear system the response trajectories eventually settle onto the limit cycle and, as it attracts the solution, causes the system to respond periodically, in what is known as a Limit Cycle Oscillation (LCO). Net damping can be seen as the sum of the structure's natural positive damping and the negative damping of the aerodynamic force, thus both flutter and limit cycle oscillations necessitate an input of energy into the system. The only available source of energy is the free stream

Figure II.2: The iconic collapse of the Tacoma Narrows Bridge on November 7, 1940, as a result of aeroelastic flutter caused by a 42 mph (68 km/h) wind.

and, therefore, self-excited oscillations (of limited or unlimited amplitude) occur when an aeroelastic system extracts energy from the free stream. It follows, of course, that wind-off conditions can never lead to flutter or LCOs [5].
Therefore, there is an immense requirement of predicting the flutter speed and LCOs accurately and, over the past decades, an enormous engineering literature has been dedicated on analytical, computational, and experimental aspects of the flutter problem applied not only to wings and airfoils [73, 74], but also to a wide range of elastic structures moving in flow streams, such as as flutter in coupled beams [134], flutter in rotating blades [134], flutter in hard disk drives [134], flutter in suspension bridges [8–10], flutter of blood vessel walls [135] and so on.
In particular, the main goal of this thesis is to numerically investigate the Limit Cycle Oscillations (LCOs) of a cantilever flat plate in low speed airflows. This aeroelastic problem can be faced by coupling an aerodynamic modelling, for the calculation of the aerodynamic loads acting on the structure, and a structural modelling, for taking into account the motion of the structure.
Concerning the aerodynamics, there are analytical solutions for the unsteady aerodynamic loads acting on 2D airfoils, which can be easily incorporated into a nonlinear structural model. Furthermore, empirical separated flow aerodynamic models are all two dimensional. Despite the fact that the real world is three-dimensional, 2D models have wide ranging applications to slender structures, such as helicopter and wind turbine blades, power cables and bridge decks [136–138]. Nevertheless, most aircraft wings are less slender and feature sweep and/or taper, so that the airflow around them is significantly three-dimensional. There are few analytical solutions for 3D unsteady aerodynamics in the literature. For example, Jones [139] developed an analytical solution for the impulsively started flow around a 3D elliptical wing. Some authors have extended Prandtl's lifting line theory to unsteady aerodynamics, usually through coupling with Theodorsen's work [140–142], but such approaches end up being quasi-numerical. The standard

methods used for finite wing aeroelasticity are numerical unsteady panel formulations, such as the Doublet Lattice [77] or the Vortex Lattice techniques [78,79]. The Unsteady Vortex-Lattice Method provides a medium-fidelity tool for the prediction of non-stationary aerodynamic loads in low-speed with attached flow and constitutes an attractive solution for aircraft dynamics problems, where free-wake methods become a necessity because of geometric complexity, such as flapping-wing kinematics [80–82], rotorcraft [143,144], or wind turbines [84,85,145–148]. Of particular interest are applications to very flexible low-speed aircraft [149], such as sensorcraft and High Altitude Long Endurance planes, wind turbines [85,150] or even flapping wings [82,151]. Besides, the unsteady VLM is not computational demanding, being a perfect trade-off between model accuracy (and robustness) and computational cost as shown in Figure II.3, and it is suitable for parallelisation; even if, the method can still be constrained by computational power for large enough problems.

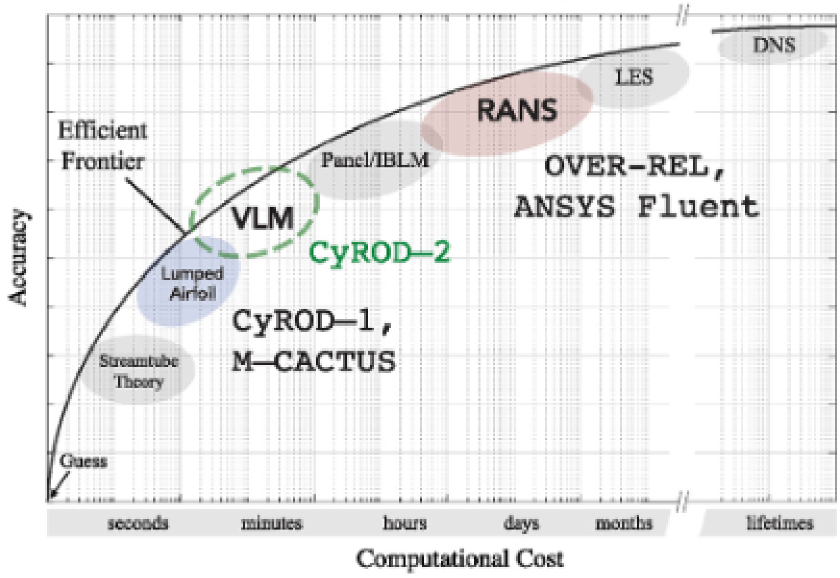


Figure II.3: Accuracy versus computational cost of different fluid modelling options (adapted from Ref. [83]).

In this thesis, a modal frequency domain version of the Vortex Lattice Method is proposed, leading to a modal Generalised Force matrix. The discussion here is a generalisation of the methodology described in Dimitriadis [5]. The resulting aeroelastic model can be solved using all the usual flutter analysis approaches, such as the k and p-k methods [152] or Rational Function Approximation [153]. Hence, the Vortex Lattice Method can be re-cast in the standard language of practical aeroelasticity.

Concerning the structure, in the classical linear theory of plates, there are two fundamental methods for the solution of both statics and dynamics problem. The first method was proposed by Cauchy [154] and Poisson [155], the second by Kirchhoff [156]. The method of Cauchy and Poisson is based on the expansion of displacements and stresses in the plate in power series of the distance z from the middle surface. Disputes concerning the convergence of these series and about

the necessary boundary conditions made this method unpopular. Moreover, the method proposed by Kirchhoff has the advantage of introducing physical meaning into the theory of plates. Von Kármán [92] extended this method to study finite deformation of plates, taking into account nonlinear geometrical terms. The nonlinear dynamic case was studied by Chu and Herrmann [157], who were the pioneers in studying nonlinear vibrations of rectangular plates. In order to deal with thicker and laminated composite plates, the Reissner-Mindlin theory of plates (first-order shear deformation theory) was introduced to take into account transverse shear strains.
The Von Kármán thin plate theory has been used in numerous application in aeroleasticity: Weiliang and Dowell [158] applied this theory to a cantilever rectangular plate oscillating in supersonic flow. Subsequent applications concerned low speed flows around both rectangular [159] and triangular [160] plates (Delta wings). [161] studied the convergence behaviour of Rayleigh-Ritz series solutions of the Von Kármán plate equations, finding that using in-plane mode shapes identical to those calculated from a finite element model for the out-of-plane displacements yielded the fastest convergence.
Attar et al. [162] showed that the effect of steady angle of attack on flutter speed is very small for low-speed Delta wings. In contrast, simulations based on Von Kármán plate theory showed that the flutter speed can decrease [163], increase [162] or remain relatively constant [162] with steady angle of attack. Furthermore, Korbahti et al. [164] presented experimental results showing that the instability onset airspeed of a Delta wing at low speeds decreases with steady angle of attack. In addition, aeroelastic model based on Von Kármán theory have shown a predicted limit cycle amplitude variation with airspeed different to the one measured experimentally, especially in the initial curvature of the limit cycle amplitude versus airspeed [87].
In 2014, Tang et al. developed the inextensible plate theory [91]. The work by Tang was motivated by the flow induced limit cycle oscillations in cantilever beams that have been observed by several investigators. A readable account of this work is contained in Paidoussis [89] and in Tang et al. [90]. In experiments, it was observed that indeed the limit cycle oscillations had deflections on the order of beam span for which the inextensible plate theory model would be applicable [90], since a higher accuracy order on the bending energy is used than other non linear plate models, such as Von Kármán. In [91] the formulation is based upon Hamilton's principle and Rayleigh–Ritz method. The computations and experiments for static deflection of a plate show that the inextensible theory produces results in excellent agreement with experiments. Moreover, the nonlinear motion equation of the inextensible plate are expressed in functions of a single unknown, i.e. the out-of-plane displacement of the plate; this is very attractive from an aeroelastic point of view since this structural model can be more readily combined with a fluid model to study fluid-structural interaction.
Thus, the mathematical models of the plate, presented in this dissertation, is developed using nonlinear inextensible plate theory [91] and a modal frequency-domain generalised force version of the unsteady Vortex Lattice method [86]. In particular, the applicability of inextensible plate theory [91] to the structural

modelling of this problem will be assessed. The emphasis is on predicting LCO amplitudes and frequencies with accuracy, as the VLM approach has already been demonstrated to yield good predictions of the instability onset conditions (flutter speed and frequency) [87]. The coupled fluid-structure interaction modal equations will be solved for the LCO amplitudes and frequencies using a numerical integration scheme [5]. The predictions of the model will be compared to estimates obtained from an earlier model that makes use of Von Kármán thin plate theory, which overpredicted the LCO amplitude [86].

# Chapter II.2

# Mathematical model formulation

## II.2.1 Structural modelling

The mathematical model used in this thesis consists of a combination of inextensible thin plate theory and the Vortex Lattice aerodynamic modelling method, as described by Dimitriadis [5]. Following the work of Tang et al. [91], this work uses the Rayleigh–Ritz methodology and the Lagrange's equations to derive the equations of motion.

Consider the cantilever plate of Figure II.4, built-in at $y = 0$ and free at $y = s$,

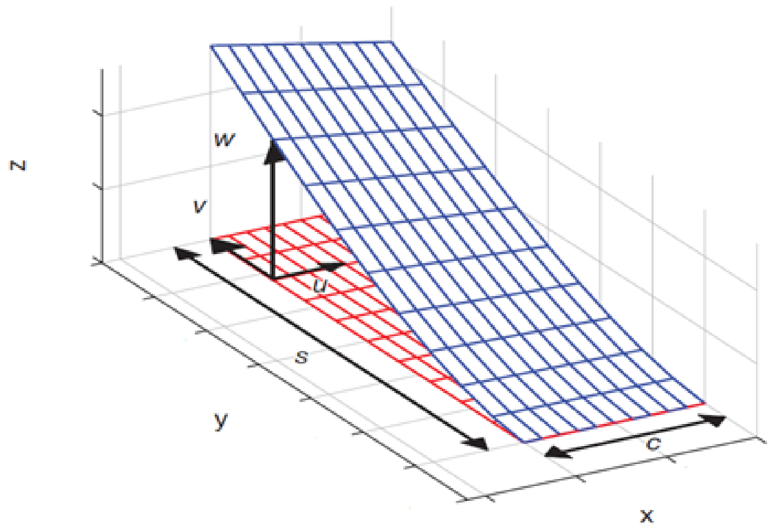


Figure II.4: Plate geometry and deformation (adapted from Ref. [5]).

where $s$ is the spanwise length of the plate, the potential energy of the plate is

$$U_p = \frac{1}{2}\frac{E}{1-\nu^2}\int_0^h \int_0^s \int_0^c \left[\epsilon_{xx}^2 + \epsilon_{yy}^2 + 2\nu\epsilon_{xx}\epsilon_{yy} + \frac{1-\nu}{2}\epsilon_{xy}^2\right] dxdydz \qquad \text{(II.1)}$$

where $c$ is the chord length of the plate, $h$ the thickness of the plate, $E$ the Young's modulus of the plate, and $\nu$ the Poisson's ratio of the plate. From Novozhilov [165]

$$\begin{aligned} \epsilon_{xx} &= \hat{\epsilon}_{xx} + z\kappa_{xx} \\ \epsilon_{yy} &= \hat{\epsilon}_{yy} + z\kappa_{yy} \\ \epsilon_{xy} &= \hat{\epsilon}_{xy} + z\kappa_{xy} \end{aligned} \tag{II.2}$$

or

$$\{\epsilon\} = \{\hat{\epsilon}\} + z\{\kappa\}$$

where $\{\hat{\epsilon}\}$ is the mid-plane strain of the plate and $\kappa$ is the middle surface curvature.
The inextensible plate theory is based on the following assumptions

$$\hat{\epsilon}_{xx} = \hat{\epsilon}_{yy} = \hat{\epsilon}_{xy} = 0, \quad \text{or} \quad \{\hat{\epsilon}\} = 0 \tag{II.3}$$

Now, substituting Equation (II.3) into Equation (II.1) and performing the integration with respect to $z$, the potential energy of the plate becomes

$$U_p \cong \frac{1}{2}\frac{Eh^3}{12(1-\nu^2)}\int_0^s\int_0^c \left[\kappa_{xx}^2 + \kappa_{yy}^2 + 2\nu\kappa_{xx}\kappa_{yy} + \frac{1-\nu}{2}\kappa_{xy}^2\right] dxdy \tag{II.4}$$

Using the inextensible plate theory, for the detailed derivation see Tang et al. [91], $\kappa_{xx}^2$, $\kappa_{yy}^2$, $\kappa_{xy}$ and $\kappa_{xx}\kappa_{yy}$ can be expressed as

$$\begin{aligned} \kappa_{xx}^2 &\cong \left(\frac{\partial^2 w}{\partial x^2}\right)^2 \left[1 + \left(\frac{\partial w}{\partial x}\right)^2 + \left(\frac{\partial w}{\partial y}\right)^2\right] \\ \kappa_{yy}^2 &\cong \left(\frac{\partial^2 w}{\partial y^2}\right)^2 \left[1 + \left(\frac{\partial w}{\partial x}\right)^2 + \left(\frac{\partial w}{\partial y}\right)^2\right] \\ \kappa_{xy}^2 &\cong 4\left(\frac{\partial^2 w}{\partial x\partial y}\right)^2 \left[1 + \left(\frac{\partial w}{\partial x}\right)^2 + \left(\frac{\partial w}{\partial y}\right)^2\right] \\ \kappa_{xx} &\cong -\left(\frac{\partial^2 w}{\partial x^2}\right)^2 \left(1 + \frac{1}{2}\left(\frac{\partial w}{\partial x}\right)^2 + \frac{1}{2}\left(\frac{\partial w}{\partial y}\right)^2\right) + HOT \\ \kappa_{yy} &\cong -\left(\frac{\partial^2 w}{\partial y^2}\right)^2 \left(1 + \frac{1}{2}\left(\frac{\partial w}{\partial x}\right)^2 + \frac{1}{2}\left(\frac{\partial w}{\partial y}\right)^2\right) + HOT \end{aligned} \tag{II.5}$$

where $HOT$ are negligible terms of higher order. Substituting Equation (II.5) in Equation (II.1), the potential energy of an inextensible plate is given by

$$\begin{aligned} U_p = \frac{D}{2}\int_0^s\int_0^c &\left[1 + \left(\frac{\partial w}{\partial x}\right)^2 + \left(\frac{\partial w}{\partial y}\right)^2\right]\left[\left(\frac{\partial^2 w}{\partial x^2}\right)^2 + \left(\frac{\partial^2 w}{\partial y^2}\right)^2 + 2\nu\frac{\partial^2 w}{\partial x^2}\frac{\partial^2 w}{\partial y^2} + \right. \\ &\left. + 2(1-\nu)\left(\frac{\partial^2 w}{\partial x\partial y}\right)^2\right] dxdy \end{aligned} \tag{II.6}$$

where $D = \dfrac{Eh^3}{12(1-\nu^2)}$ is the stiffness of the plate.
The kinetic energy of a plate can be written as

$$T_p = \frac{1}{2}\int_0^s \int_0^c m_m(\dot{u}^2 + \dot{v}^2 + \dot{w}^2)dxdy \tag{II.7}$$

where $m_m = \rho_m h$ is the mass per unit area and $\rho_m$ the material density of the plate. Recalling Equation (II.3), $u$ and $v$ can be calculated from

$$u(x,y,t) = -\frac{1}{2}\int_{c/2}^{x}\left(\frac{\partial w(\zeta,y,t)}{\partial \zeta}\right)^2 d\zeta$$
$$v(x,y,t) = -\frac{1}{2}\int_{0}^{y}\left(\frac{\partial w(x,\eta,t)}{\partial \eta}\right)^2 d\eta$$

and thus

$$\dot{u}(x,y,t) = -\int_{c/2}^{x}\frac{\partial w(\zeta,y,t)}{\partial \zeta}\frac{\partial^2 w(\zeta,y,t)}{\partial \zeta \partial t}d\zeta$$
$$\dot{v}(x,y,t) = -\int_{0}^{y}\frac{\partial w(x,\eta,t)}{\partial \eta}\frac{\partial^2 w(x,\eta,t)}{\partial \eta \partial t}d\eta$$

The expression for $u$ invokes symmetry for the in-plane deflection field. Note that for the rectangular cantilever plate $u$ at $x = c/2$ and $v = 0$ at $y = 0$. For a more general formulation see the work by McHugh et al. [166].
Therefore, the expression for the kinetic energy of an inextensible plate is given by

$$T_p = \frac{1}{2}\int_0^s \int_0^c m_m\left[\left(\int_{c/2}^{x}\frac{\partial w}{\partial \zeta}\frac{\partial^2 w}{\partial \zeta \partial t}d\zeta\right)^2 + \left(\int_{0}^{y}\frac{\partial w}{\partial \eta}\frac{\partial^2 w}{\partial \eta \partial t}d\eta\right)^2 + \dot{w}^2\right]dxdy \tag{II.8}$$

As shown in Equation (II.6) and in Equation (II.8), both the kinetic and potential energy of an inextensible plate are functions only of a single unknown, i.e. the transversal deflection $w$ of the plate, which can be expanded using a Rayleigh-Ritz approach

$$w(x,y,t) = \sum_{j=1}^{m_r} w_j(x,y)r_j(t) \tag{II.9}$$

where $w_j(x,y)$ are mode shapes of the transverse deflection of the plate and $r_j(t)$ are the generalised coordinates of the plate in the $z$ direction. The equations of motion for the problem can be derived using Lagrange's equations

$$\frac{d}{dt}\left(\frac{\partial L}{\partial \dot{r}_j}\right) - \frac{\partial L}{\partial r_j} = Q_i \tag{II.10}$$

for $i = 1, ...m_r$, where $L = T_p - U_p$ and $Q_i$ are the generalised forces in the out of plane directions, in this case the aerodynamic loads. The expression for these loads will be derived in the next section via VLM.

For any set of mode shapes, it can be shown that Lagrange's equations can be written in matrix form as

$$\mathbf{A}\ddot{\mathbf{r}} + \mathbf{E}\mathbf{r} + \mathbf{N}_s(\mathbf{r} \otimes \mathbf{r} \otimes \mathbf{r}) + \mathbf{N}_i\left[(\mathbf{r} \otimes \dot{\mathbf{r}} \otimes \dot{\mathbf{r}}) + (\mathbf{r} \otimes \mathbf{r} \otimes \ddot{\mathbf{r}})\right] = \mathbf{Q}(t) \qquad \text{(II.11)}$$

where $\mathbf{A}$ is the $m_r \times m_r$ mass matrix, $\mathbf{E}$ is the $m_r \times m_r$ stiffness matrix, $\mathbf{N}_s$ is a $m_r \times m_r^3$ matrix related to the nonlinear stiffness term and $\mathbf{N}_i$ is a $m_r \times m_r^3$ matrix related to the nonlinear inertial term. Furthermore, the symbol $\otimes$ denotes the Kronecker product of two vectors or matrices. The column vectors $\mathbf{r}$ contains $r_j$ generalised coordinates and the column vector $\mathbf{Q}$ contains the $r_j$ generalised forces. The equations of motion obtained with inextensible plate theory has the substantial advantage of being a function only of the $r$ generalised coordinate, unlike Von Kármán's plate theory for example, and can be more easily combined with a fluid model to study fluid–structural interaction.
The inextensible plate theory has been applied to a computational plate for a static and a dynamic case. An aluminium cantilever plate, with $E = 70.6 \times 10^9$ Pa and $\rho_m = 2960\,\mathrm{Kg/m^3}$, has been analysed. The plate has a constant chord length, $c$, of 2.85 cm, a constant span length, $s$, of 50.8 cm, and a constant thickness, $h$, of 1.8 mm. For the static bending deflection test, a gravity (mass) load is added to the plate at $x = c/2$ (chordwise direction) and $y = s$ (spanwise direction) and varies from 0 to 0.815 kg. The transverse deflection mode shapes $w_j(x, y)$, needed in the Rayleigh-Ritz expansion, have been approximated by the product of free-free beam modes, $m_x$, and cantilever beam modes, $n_y$. A good level of convergence is reached with $m_x \geqslant 2$ and $n_y \geqslant 2$. The nondimensional plate tip deflections normalized by plate span $w(c/2, s)/s$ in the $z$-direction are computed. The obtained results have been compared to experimental results published by Tang et al. [91] and numerical results obtained with Von Kármán's plate theory, as shown in Figure II.5. An excellent agreement between the computations, using the inextensible plate theory, and the experimental results is obtained. It is worth pointing out that the Von Kármán's plate model predictions on the static deflection, even if better than the linear ones, are still too far from experimental results; proving the improved accuracy on the bending energy of the inextensible plate model.
Since there is a substantial lack of experimental dynamic results for cantilever plates in the literature, a computational study of the dynamic deflection of the plate has been made and the obtained results have been compared with the numerical ones obtained by Tang et al. [91], in order to confirm the correct implementation of the inextensible plate theory as structural model. The dimensions and material properties of the plate are the same of those used in the static example. The exciting force is harmonic, with a constant amplitude of 0.025 kg and its frequency f varies from 3 Hz to 9 Hz, around the first flexural mode of the plate located at 5.5 Hz. The excitation point is at $x = c/2$ and $y = 0.7s$ and the response point is at $x = c/2$ and $y = s$. Modal structural damping ratio $\xi$ equal to 0.01 is considered for all structural modes. A good level of convergence is reached with $m_x \geqslant 2$ and $n_y \geqslant 2$. There are 31 frequencies from $f = 3$ Hz to 9 Hz with $\Delta f = 0.2$ Hz considered in the calculations. At each frequency, the time history is computed until the system achieves a steady state response. In general,

the time simulation is continued for about 40 s (a time step of $\Delta t = 1/4096$ s is used). For the next frequency (increasing $\Delta f$), the initial conditions are provided by the previous dynamic state. This process is continuous in time until the frequency increases to 9 Hz.
In Figure II.6, the rms dynamic amplitude divided by the span length, s, of the plate, versus frequency for the increasing frequency process is shown. In particular, in red are shown the results obtained with only the inertial nonlinear term, in blue are shown the results obtained with only the stiffness nonlinear term and in yellow are shown the results obtained with the full nonlinear model.
In Figure II.7, the same results are shown for the decreasing frequency process, which is the same as the above but with the excitation frequency that varies from 9 Hz to 3 Hz. It is interesting to note that the stiffness nonlinearity leads to an increase in the resonant frequency (hard nonlinearity) and the inertia nonlinearity leads to a decrease in the resonant frequency (soft nonlinearity) compared to the full nonlinear model, which is a dynamic balance between the stiffness and inertia nonlinearities. Furthermore, it is possible to observe that the dynamic response of the plate depending on whether the frequency is increasing or decreasing: in the increasing excitation frequency the hard nonlinearity is predominant on the soft nonlinearity, while the opposite happens in the decreasing excitation process. Both in Figure II.6 and II.7 the numerical results are in perfect agreement with those published by Tang et al. in [91] for the same dynamic test.

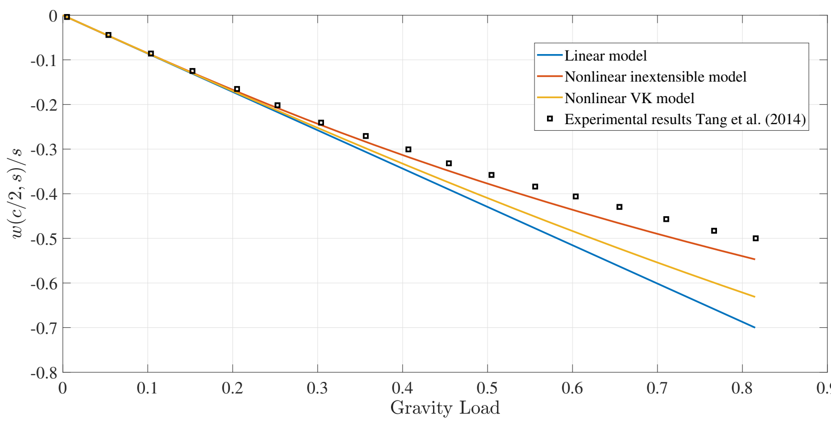


Figure II.5: Comparison between the static deflection of a cantilever plate obtained with (i) linear model (blue curve), (ii) nonlinear Von Kármán's plate model (brown curve), (ii) nonlinear inextensible plate model (red curve), (iii) experiments (black squared markers).

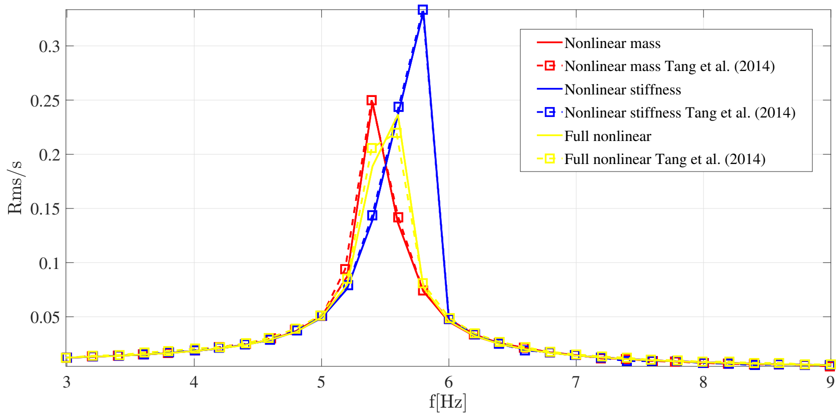


Figure II.6: Comparison between the numerical results obtained for the dynamic deflection of a cantilever plate with increasing excitation frequency using the inextensible plate model (solid curves) and those published by Tang et al. [91] for the same case (dashed curves and squared markers).

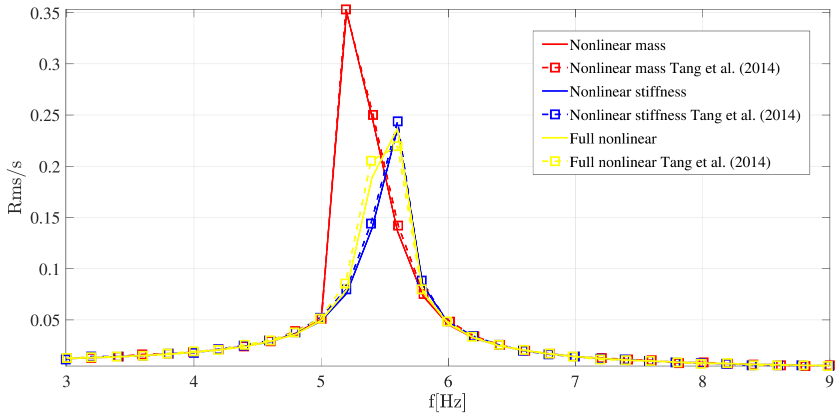


Figure II.7: Comparison between the numerical results obtained for the dynamic deflection of the plate with decreasing excitation frequency using the inextensible plate model (solid curves) and those published by Tang et al. [91] for the same case (dashed curves and squared markers).

## II.2.2 Aerodynamic modelling

Once the structural model has been defined, the generalised aerodynamic forces need to be computed. To this aim, the unsteady Vortex Lattice Method [78] is employed. The VLM models attached flow over thin wings and blades and considers the flow always attached to the surface. The strong nonlinearity given by flow separation cannot be modelled by the standard VLM. Another important principle of the VLM is that it models thin plates and wings, therefore it ignores their thickness and considers their camber surface, which is the mean of the upper surface and lower surface at each spanwise location. The first step is to collocate geometric panels on the mean (camber) surface of the plate. Vortex rings are anchored on them, such that the leading edge of each vortex ring corresponds with the quarter-chord line of each panel. The impermeability boundary condition is enforced on control points placed on the three-quarter-chord of each panel. The wake behind the plate is also discretized in vortex rings in order to overlap the leading edge of the first wake ring with the trailing edge of the last bound vortex ring. In Figure II.8, an example of a discretization scheme for a wing and its wake is shown. In our case, the wing will be replaced by a flat cantilever plate. Thus, the plate discretization is constituted by $m_v$ chordwise and $n_v$ spanwise panels and its wake is composed by $m_w$ chordwise and $n_v$ spanwise vortex rings. The plate is surrounded by a free stream with velocity $\mathbf{U}_\infty = [U\ V\ W]$, i.e. with airspeed $\mathbf{Q}_\infty = |\mathbf{U}_\infty|$ and direction $\hat{\mathbf{u}} = [U\ V\ W]\ /Q_\infty$. The wake is flat and spreads in the streamwise direction with the free stream airspeed. The chordwise spacing of the wake vortex rings is selected as $c/m_v$, where $c$ is the chord of the plate. In the VLM, the lattices of the plate and wake remain unchanged during all the time history. A downwash term is considered to take account of structural motion in the out-of-plane direction (in-plane motion and in-plane grid deformations are neglected). The impermeability boundary condition can now be expressed as [86]

$$Q_\infty \mathrm{diag}(\hat{\mathbf{U}}\mathbf{n}^{\mathrm{T}}) - U\mathbf{w}_x\mathbf{r}(t) - \mathbf{w}_x\dot{\mathbf{r}}(t) + \mathbf{A}_b\mathbf{\Gamma}_b(t) + \mathbf{A}_w\mathbf{\Gamma}_w(t) = 0 \qquad \text{(II.12)}$$

where $\hat{\mathbf{U}}$ is the $m_v n_v \times 3$ matrix whose rows are all equal to $\hat{\mathbf{u}}$, $\mathbf{n}$ is the $m_v n_v \times 3$ matrix of unit vectors normal to the surface of the panels (see Figure II.8), T denotes the transpose of a matrix, $U$ is the $x$-component of the free stream velocity, $\mathbf{w}$ is a $m_v n_v \times m_r$ matrix of out-of-plane mode shapes, $\mathbf{r}$ is the $m_r \times 1$ vector of generalised coordinates, $\mathbf{A}_b$ is the $m_v n_v \times m_v n_v$ influence coefficient matrix of the bound vorticity, $\mathbf{\Gamma_b}(t)$ is the $m_v n_v \times 1$ vector of the strengths of the bound vortex rings, $\mathbf{A}_w$ is the $m_w n_v \times m_w n_v$ influence coefficient matrix of the wake vorticity and $\mathbf{\Gamma_w}(t)$ is the $m_w n_v \times 1$ vector of the strengths of the wake vortex rings. In order to guarantee the Kutta condition, the trailing bound vortex ring is spread into the wake at the next time instance, such that the leading row of wake vortices at time $t$ has the magnitude of the trailing row of bound vortices

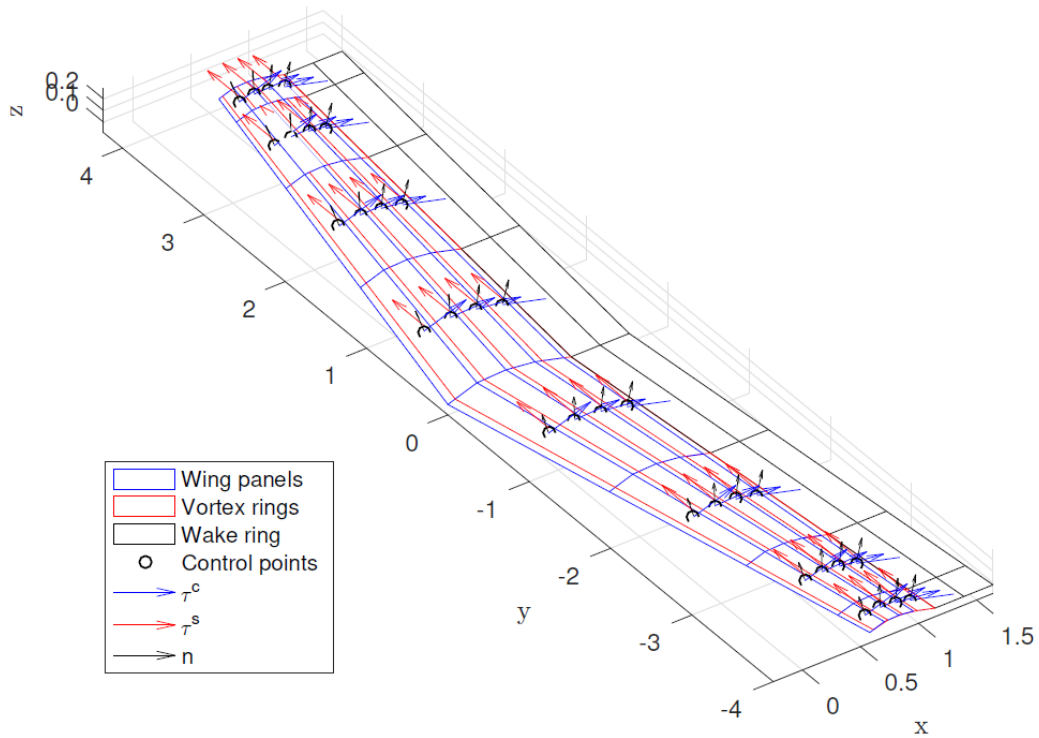


Figure II.8: Wing discretization for the Vortex Lattice method (adapted from Ref. [87]).

at time $t - \Delta t$. Accordingly, the wake vortex strength can be expressed as

$$\mathbf{\Gamma}_w(t) = \begin{pmatrix} \mathbf{P}_c\mathbf{\Gamma}_b(t-\Delta t) \\ \mathbf{P}_c\mathbf{\Gamma}_b(t-2\Delta t) \\ \vdots \\ \mathbf{P}_c\mathbf{\Gamma}_b(t-m_w\Delta t) \end{pmatrix} \tag{II.13}$$

where $\mathbf{P}_c$ is a $n_v \times m_v n_v$ matrix that is employed to select only the trailing spanwise bound vortex segments. The expression of $\mathbf{\Gamma_w}(t)$ is still not useful since values of the bound vorticity from previous time steps are included. This problem can be overcome by considering that the Fourier Transform of $\mathbf{\Gamma}_b(t-\Delta t)$ is $e^{-\mathrm{i}\omega\Delta t}\mathbf{\Gamma}_b(\omega)$, where $\omega$ is the frequency and i denotes the imaginary unit. Therefore, the expression of the wake vorticity can be evaluated as follows

$$\mathbf{\Gamma}_w(\omega) = \mathbf{P}_e(\omega)\mathbf{P}_c\mathbf{\Gamma}_b(\omega) \tag{II.14}$$

where

$$\mathbf{P}_e(\omega) = \begin{pmatrix} \mathbf{I}_n e^{-\mathrm{i}\omega\Delta t} \\ \mathbf{I}_n e^{-\mathrm{i}\omega 2\Delta t} \\ \vdots \\ \mathbf{I}_n e^{-\mathrm{i}\omega m_w\Delta t} \end{pmatrix} \tag{II.15}$$

Computing the Fourier Transform of Equation (II.12), substituting Equation (II.14) as expression of wake vorticity in the frequency domain, and solving for $\mathbf{\Gamma}_b(\omega)$ results in

$$\mathbf{\Gamma}_b(\omega) = -(\boldsymbol{A}_b + \boldsymbol{A}_w \mathbf{P}_e(\omega)\mathbf{P}_c)^{-1} \left( Q_\infty \mathrm{diag}(\hat{\mathbf{U}}\mathbf{n}^{\mathrm{T}})\delta(\omega) - (U\mathbf{w}_x - \mathrm{i}\omega\mathbf{w}_x\mathbf{r}(\omega)\right) \mathbf{r}(\omega) \tag{II.16}$$

where $\delta(\omega)$ is the Dirac delta function.
The value of $\mathbf{\Gamma}_b(\omega)$ now relies solely on the geometry of the plate and wake, the free flow airspeed and the downwash motion induced by the structural deformations. The aerodynamic normal load acting on the panels can be calculated from [78,168]

$$\begin{aligned} \mathbf{L} =& \rho \left( \mathrm{diag}\left( (Q_\infty \hat{\mathbf{U}} + \mathbf{U}_w)\boldsymbol{\tau}_c^{\mathrm{T}} \right) - \left( U\frac{\partial \mathbf{z}}{\partial x} + \frac{\partial \mathbf{z}}{\partial t} \right) \circ \boldsymbol{\tau}_{c_z} \right) \circ \mathbf{G}_c \mathbf{\Gamma}_b \\ &+ \rho \left( \mathrm{diag}\left( (Q_\infty \hat{\mathbf{U}} + \mathbf{U}_w)\boldsymbol{\tau}_s^{\mathrm{T}} \right) - \left( U\frac{\partial \mathbf{z}}{\partial x} + \frac{\partial \mathbf{z}}{\partial t} \right) \circ \boldsymbol{\tau}_{s_z} \right) \circ \mathbf{G}_s \mathbf{\Gamma}_b \\ &+ \rho \boldsymbol{G}_A \dot{\mathbf{\Gamma}}_b \end{aligned} \tag{II.17}$$

where $\mathbf{G}_w$ is a $m_v n_v \times 3$ vector of flow speeds induced by the wake, $\boldsymbol{\tau}_c$ and $\boldsymbol{\tau}_s$ s are $m_v n_v \times 3$ matrices containing the spanwise and chordwise tangential vectors, $\boldsymbol{\tau}_{c_z}$ and $\boldsymbol{\tau}_{s_z}$ are $m_v n_v \times 1$ vectors of the $z$-components only of the chordwise and spanwise tangent vectors and the $\circ$ symbol indicates the Hadamard product. The matrices $\mathbf{G}_c$ and $\mathbf{G}_s$, when post-multiplied by $\mathbf{\Gamma}_b$, give the products $(\Gamma_{i,j} - \Gamma_{i-1,j})A_{i,j}/\Delta c_{i,j}$ and $(\Gamma_{i,j} - \Gamma_{i,j-1})A_{i,j}/\Delta s_{i,j}$ for all panels in matrix form respectively. $A_{i,j}$ indicates the area of the panel $i, j$, $\Delta c_{i,j}$ denotes the panel chord spacing, and $\Delta s_{i,j}$ denotes the panel span spacing. Ultimately, $\mathbf{G}_A$ is a $m_v n_v \times m_v n_v$ diagonal matrix, filled with diagonal elements equal to $A_{i,j}$.

Equation (II.17) can be linearised (for all the technical details about linearisation see Ref. [86])

$$\mathbf{L} = \rho Q_\infty \left( \mathrm{diag}\left( \hat{\mathbf{U}}\boldsymbol{\tau}_c^{\mathrm{T}} \right) \circ \mathbf{G}_c \mathbf{\Gamma}_b(t) + \mathrm{diag}\left( \hat{\mathbf{U}}\boldsymbol{\tau}_s^{\mathrm{T}} \right) \circ \mathbf{G}_s \mathbf{\Gamma}_b(t) \right) + \rho \mathbf{G}_A \dot{\mathbf{\Gamma}}_b(t) \tag{II.18}$$

Computing the Fourier Transform of Equation (II.18) results in

$$\mathbf{L}(\omega) = \rho(Q_\infty \mathbf{G}_{cs} + \mathrm{i}\omega \mathbf{G}_A)\mathbf{\Gamma}_b(\omega) \tag{II.19}$$

where

$$\begin{aligned} \mathbf{G}_{cs} = & \left( \mathrm{diag}\left( \hat{\mathbf{U}}\boldsymbol{\tau}_c^{\mathrm{T}} \right) \mathrm{diag}\left( \hat{\mathbf{U}}\boldsymbol{\tau}_c^{\mathrm{T}} \right) \cdots \mathrm{diag}\left( \hat{\mathbf{U}}\boldsymbol{\tau}_c^{\mathrm{T}} \right) \right) \circ \mathbf{G}_c \\ & \left( \mathrm{diag}\left( \hat{\mathbf{U}}\boldsymbol{\tau}_s^{\mathrm{T}} \right) \mathrm{diag}\left( \hat{\mathbf{U}}\boldsymbol{\tau}_s^{\mathrm{T}} \right) \cdots \mathrm{diag}\left( \hat{\mathbf{U}}\boldsymbol{\tau}_s^{\mathrm{T}} \right) \right) \circ \mathbf{G}_s \end{aligned}$$

Ultimately, after substituting the expression of $\mathbf{\Gamma}_b(\omega)$ from Equation (II.16) and employing the definition of the reduced frequency $k = \omega b / Q_\infty$, where $b$ is the half-chord of the plate, the lift equation becomes

$$\mathbf{L}(k) = -\rho Q_\infty^2 (\mathbf{L}_0(k) - \mathbf{L}_1(k)\mathbf{r}_1(k)) \tag{II.20}$$

where

$$\mathbf{L}_0(k) = \left( \mathbf{G}_{cs} + \mathrm{i}\frac{k}{b}\mathbf{G}_A \right) (\mathbf{A}_b + \mathbf{A}_w \mathbf{P}_e(k)\mathbf{P}_c)^{-1} \mathrm{diag}\left( \hat{\mathbf{U}}\mathbf{n}^{\mathrm{T}} \right) \delta(k)$$

and

$$\mathbf{L}_1(k) = \left(\mathbf{G}_{cs} + \mathrm{i}\frac{k}{b}\mathbf{G}_A\right)(\mathbf{A}_b + \mathbf{A}_w\mathbf{P}_e(k)\mathbf{P}_c)^{-1}\left(\mathbf{w}_x + \mathrm{i}\frac{k}{b}\mathbf{w}\right)$$

where a small attack angle is considered, that is $U \approx Q_\infty$.

The generalised aerodynamic loads of Equation (II.11) can be evaluated as follows

$$Q_i(t) = \int_S \Delta p(x, y, t)\frac{\partial w}{\partial r_i}dS \tag{II.21}$$

where $\Delta p(x, y, t)$ is the pressure difference acting on point $(x, y)$ at time $t$ and $S$ is the total area of the plate. Considering that $\Delta pdS$ is an infinitesimal lift force and that the lift calculated by the VLM is constituted by the sum of each infinitesimal lift contribution, applied on the control point of each panel, the generalised forces can be written in matrix form as follows

$$\mathbf{Q}(k) = \left(\mathbf{L}(k)^{\mathrm{T}}\mathbf{w}\right)^{\mathrm{T}} \tag{II.22}$$

where $\mathbf{Q}(k)$ is the $m_r \times m_r$ generalised force matrix in the frequency domain, being $m_r$ the total number of out-of-plane modes. Substituting the lift expression of Equation (II.20) into Equation (II.22), the final form of the generalised force matrix becomes

$$\mathbf{Q}(k) = -\rho Q_\infty^2(\mathbf{Q}_0(k) - \mathbf{Q}_1(k)\mathbf{r}_1(k)) \tag{II.23}$$

where

$$\mathbf{Q}_0(k) = \left(\mathbf{L}_0(0)^{\mathrm{T}}\mathbf{w}\right)^{\mathrm{T}} \quad \text{and} \quad \mathbf{Q}_1(k) = \left(\mathbf{L}_1(k)^{\mathrm{T}}\mathbf{w}\right)^{\mathrm{T}} \tag{II.24}$$

The generalised force of Equation (II.22) is expressed in the frequency domain and cannot be inserted into Equation (II.11). Roger's rational function approximation (RFA) [153], also known as the Padé approximation, is used in order to transform $\mathbf{Q}(k)$ into the time domain.

Using the properties of the Dirac delta function, it is straightforward to conclude that the inverse Fourier Transform of $\mathbf{Q_0}(k)$ is the constant

$$\mathcal{F}^{-1}(\mathbf{Q}(k)) = \mathcal{F}^{-1}(\mathbf{Q}(\omega)) = \mathbf{Q}_0 = (\mathbf{L_0}(0)^{\mathrm{T}}\mathbf{w})^{\mathrm{T}}$$

where $\mathcal{F}^{-1}$ denotes the inverse Fourier Transform and

$$\mathbf{L}_0(0) = \mathbf{G}_{cs}(\mathbf{A}_b + \mathbf{A}_w\mathbf{P}_e(0)\mathbf{P}_c)^{-1}\mathrm{diag}\left(\hat{\mathbf{U}}\mathbf{n}^{\mathrm{T}}\right)$$

Unfortunately, there is no obvious analytical expression for the inverse Fourier Transform of $\mathbf{Q}_1(k)\mathbf{r}_1(k)$. Roger [153] suggested to expand $\mathbf{Q}_1(k)$ as follows

$$\mathbf{Q}_1(k) = \mathbf{S}_0 + \mathrm{i}k\mathbf{S}_1 + (\mathrm{i}k)^2\mathbf{S}_2 + \sum_{i=1}^{n_l}\mathbf{S}_{2+i}\frac{\mathrm{i}k}{\mathrm{i}k + \gamma_i} \tag{II.25}$$

where $\mathbf{S}_1$ are $m_r \times m_r$ real matrices. Roger's approximation includes $n_l$ aerodynamic lag terms designed to represent the memory effect of unsteady aerodynamics, that is, the vorticity stored in the wake. Each aerodynamic lag term is associated with a lag coefficient, $\gamma_i$. After substituting $k = \omega b/Q_\infty$, the following expression is obtained

$$\mathbf{Q}_1(\omega) = \mathbf{S}_0 + \mathrm{i}\omega\left(\frac{b}{Q_\infty}\right)\mathbf{S}_1 + (\mathrm{i}\omega)^2\left(\frac{b}{Q_\infty}\right)^2\mathbf{S}_2 + \sum_{i=1}^{n_l}\mathbf{S}_{2+i}\frac{\mathrm{i}\omega}{\mathrm{i}\omega + (Q_\infty/b)\gamma_i}$$

The inverse Fourier Transform can now be applied to $\mathbf{Q}_1(\omega)\mathbf{r}(\omega)$ using Roger's expression for $\mathbf{Q}_1(\omega)$. The inverse transformation results in

$$\begin{aligned}\mathcal{F}^{-1}(\mathbf{Q}(\omega)\mathbf{r}(\omega)) =& \mathbf{S}_0\mathbf{r}(t) + \left(\frac{b}{Q_\infty}\right)\mathbf{S}_1\dot{\mathbf{r}}(t) + \left(\frac{b}{Q_\infty}\right)^2\mathbf{S}_2\ddot{\mathbf{r}}(t) + \\ &+ \sum_{i=1}^{n_l}\mathbf{S}_{2+i}\int_0^t \dot{\mathbf{r}}(\tau)e^{-Q_\infty\gamma_i(t-\tau)/b}d\tau\end{aligned}$$

where $\tau$ is an integration variable. The integral terms in this expression are similar to the ones obtained from Wagner function aerodynamic modelling, described in detail in [5]. It is possible to define them as the aerodynamic states

$$\boldsymbol{\eta}_{\boldsymbol{i}}(t) = \int_0^t \dot{\mathbf{r}}(\tau)e^{-Q_\infty\gamma_i(t-\tau)/b}d\tau$$

Now a complete time domain expression for the generalised aerodynamic forces can be written, after substituting the inverse Fourier Transforms of $\mathbf{Q_0}(\omega)$ and $\mathbf{Q_1}(\omega)\mathbf{r}(\omega)$ into Equation (II.23), such that

$$\mathbf{Q}(t) = -\rho Q_\infty^2\mathbf{Q}_0 + \rho Q_\infty^2\mathbf{S}_0\mathbf{r}(t) + \rho Q_\infty b\mathbf{S}_1\dot{\mathbf{r}}(t) + \rho b^2\mathbf{S}_2\ddot{\mathbf{r}}(t) + \rho Q_\infty^2\sum_{i=1}^{n_l}\mathbf{S}_{2+i}\boldsymbol{\eta}_{\boldsymbol{i}}(t) \tag{II.26}$$

where $\mathbf{S}_0$ to $\mathbf{S}_{n_l}$ are aerodynamic stiffness, damping, mass and lag matrices, $\eta_i$ are aerodynamic lags and $n_l$ is the total number of lags retained in the approximation.

A complete set of time-domain aeroelastic equations can now be obtained by substituting Equation (II.26) into Equation (II.11)

$$\begin{aligned}(\mathbf{A} - \rho b^2\mathbf{S}_2)\ddot{\mathbf{r}} - (\rho Q_\infty b\mathbf{S}_1)\dot{\mathbf{r}} + (\mathbf{E} - \rho Q_\infty^2\mathbf{S}_0)\mathbf{r} + \rho Q_\infty^2\sum_{i=1}^{n_l}\mathbf{S}_{2+i}\boldsymbol{\eta}_i \\ + \mathbf{N}_s(\mathbf{r}\otimes\mathbf{r}\otimes\mathbf{r}) + \mathbf{N}_i\left[(\mathbf{r}\otimes\dot{\mathbf{r}}\otimes\dot{\mathbf{r}}) + (\mathbf{r}\otimes\mathbf{r}\otimes\ddot{\mathbf{r}})\right] = -\rho Q_\infty^2\mathbf{Q}_0 \\ \dot{\boldsymbol{\eta}}_i - \dot{\mathbf{r}} - \frac{U\gamma_i}{b}\boldsymbol{\eta}_i = \mathbf{0}\end{aligned} \tag{II.27}$$

where $\gamma_i$ are the aerodynamic lag coefficients and $\boldsymbol{\eta}$ the $n_l m_r \times 1$ aerodynamic state vector $\boldsymbol{\eta} = [\boldsymbol{\eta}_1^{\mathrm{T}} \; ... \; \boldsymbol{\eta}_{n_l}^{\mathrm{T}}]^{\mathrm{T}}$.

## II.2.3 Implementation and validation of linear model

An aluminium cantilever plate, with $E = 68.7 \times 10^9$ Pa and $\rho_m = 2770\,\mathrm{Kg/m^3}$, has been analysed. The plate has a constant chord length, $c$, of 20 cm, a constant span length, $s$, of 80 cm, and a constant thickness, $h$, of 1 mm, thus the aspect ratio of the plate, denoted by AR and defined as $s/c$, is equal to 4. For the out-of-plane displacement, the mode shapes can be obtained as products of free-free and cantilever beam modes [158,167]. The exact expressions for the beam modes are

$$\Phi_m(x) = -\mathrm{sinh}\beta_m x/c - \mathrm{sin}\beta_m x/c - \frac{\mathrm{sin}\beta_m - \mathrm{sinh}\beta_m}{\mathrm{cosh}\beta_m - \mathrm{cos}\beta_m}(\mathrm{cosh}\beta_m x/c + \mathrm{cos}\beta_m x/c)$$
$$\Psi_n(y) = -\frac{\mathrm{sinh}\alpha_n - \mathrm{sin}\alpha_n}{\mathrm{cos}\alpha_n + \mathrm{cosh}\alpha_n}(\mathrm{sin}\alpha_n y/s - \mathrm{sinh}\alpha_n y/s) + (\mathrm{cosh}\alpha_n y/s - \mathrm{cos}\alpha_n y/s) \tag{II.28}$$

where $\Phi_m(x)$ are free-free beam modes and $\Psi_n(y)$ are cantilever beam modes. Equations (II.28) are written for $m = 1, ..., m_x$, $n = 1, ..., n_y$ and

$$\beta_m = \begin{cases} 0 & \text{if } m = 1 \\ 4.730 & \text{if } m = 2 \\ 7.853 & \text{if } m = 3 \\ (2m-1)\pi/2 & \text{if } m > 3 \end{cases}, \quad \alpha_n = \begin{cases} 1.875 & \text{if } n = 1 \\ 4.693 & \text{if } n = 2 \\ 7.856 & \text{if } n = 3 \\ (2n-1)\pi/2 & \text{if } n > 3 \end{cases}$$

The complete 2D modes shapes are then given by

$$w_j(x, y) = \Phi_m(x)\Psi_n(y) \tag{II.29}$$

for $j = 1, ..., m_r$ where $m_r = m_x n_y$. The first free-free mode is a rigid body translation and all the higher modes are bending modes. There is no rigid body rotation mode to represent the first torsion mode of the plate. Weiliang and Dowell [158] introduced

$$\Phi_2(x) = 2\left(1 - 2\frac{x}{c}\right) \tag{II.30}$$

as the rigid body rotation mode shape. Figure II.9 plots the first four of these shapes (i.e. $m_x = 2$, $n_y = 2$), demonstrating that for $m = 1$ pure spanwise bending modes are obtained, while $m = 2$ results in torsion modes. The higher modes are combinations of spanwise and chordwise bending.

The mode shapes obtained from the Equation (II.29) were interpolated linearly on the control points of the VLM panels. However, as the flat plates are cantilevered on one end, a representative aerodynamic model can only be obtained if the plate is mirrored around its centreline so that a symmetric flowfield can be set up. Hence, the plates modelled with the VLM span from $-s$ to $s$ and are perfectly symmetrical.

Now, there are all the elements to calculate the flutter speed. To this aim, the Equation (II.11) can be rewritten after deleting the nonlinear terms

$$\mathbf{A}\ddot{\mathbf{r}} + \mathbf{E}\mathbf{r} = \mathbf{Q}(t) \tag{II.31}$$

Applying the Fourier Transform to Equation (II.31) and substituting from Equation (II.23) results in

$$\left(-\left(\frac{kQ_\infty}{b}\right)^2 \mathbf{A} + \mathbf{E} - \rho Q_\infty^2 \mathbf{Q}_1(k)\right)\mathbf{r}(k) = -\rho Q_\infty^2 \mathbf{Q}_0(0) \tag{II.32}$$

| $m_v$ | $n_v$ | $U_f$[m/s] | $m_v$ | $n_v$ | $U_f$[m/s] | $m_v$ | $n_v$ | $U_f$[m/s] |
|---|---|---|---|---|---|---|---|---|
| 10 | 10 | 17.8886 | 20 | 10 | 16.9225 | 30 | 10 | 16.6305 |
| 10 | 20 | 18.0188 | 20 | 20 | 17.0504 | 30 | 20 | 16.7575 |
| 10 | 30 | 18.0915 | 20 | 30 | 17.1225 | 30 | 30 | 16.8293 |
| 10 | 40 | 18.1328 | 20 | 40 | 17.1635 | 30 | 40 | 16.8702 |

Table II.1: Variation of flutter speed with number of chordwise and spanwise panels.

which is the classic frequency-domain linear aeroelastic equations obtained from the Vortex Lattice method for the aerodynamics and a modal model for the structure. For all other reduced frequencies, Equation (II.32) allows to define the flutter determinant

$$\det\left(-\left(\frac{k_f U_f}{b}\right)^2 \mathbf{A} + \mathbf{E} - \rho U_f^2 \mathbf{Q}_1(k_f)\right) = 0 \tag{II.33}$$

which can be solved for the flutter speed $U_f$ and flutter frequency $k_f$. The determinant in the above expression is known as the flutter determinant because it becomes equal to zero at the flutter condition. This condition can be obtained by substituting sinusoidal responses in the equation of motion, which can only occur when the damping is zero, that is, at flutter. The flutter determinant is complex, so that both its real and imaginary parts must be equal to zero. The system is nonlinear in both $k$ and $U_f$, so it must be solved iteratively.
It is now of interest to determine how the estimated flutter speed changes with number of panels. In Table II.1, the values of the flutter speed for different numbers of panels, calculated with $m_x = 4$ and $n_y = 4$, are reported. For the increasing of chordwise panels, indicated with $m_v$, the flutter speed decreases; while it is the opposite for the increasing of the spanwise panels, indicated with $n_v$. Clearly, increasing $m_v$ has a more pronounced effect than increasing $n_v$. The flutter experimental value, reported in [86] for the same plate, is equal to 17.1 m/s. Numerical predictions near to this value can be obtained for $m_v \geqslant 20$ and $10 \leq n_v \leq 40$. Increasing the length of the wake beyond $m_w = 10m_v$ has negligible effect on the flutter predictions.
Another interesting analysis concerns the variation of the flutter speed with number of modes. For these calculations, the plate has been discretized into $m_v = 20$ chordwise and $n_v = 40$ spanwise panels and $m_w = 10m_v$ wake panels. In Table II.2, the variation of the flutter speed with number of out-of-plane modes is presented. The table shows that the flutter predictions converge monotonically as the number of modes increases.

| $m_r$ | $m_x$ | $n_y$ | $U_f$[m/s] |
|---|---|---|---|
| 4 | 2 | 2 | 17.6186 |
| 9 | 3 | 3 | 17.4452 |
| 16 | 4 | 4 | 17.1635 |
| 25 | 5 | 5 | 17.1397 |

Table II.2: Variation of flutter speed with number out-of-plane modes.

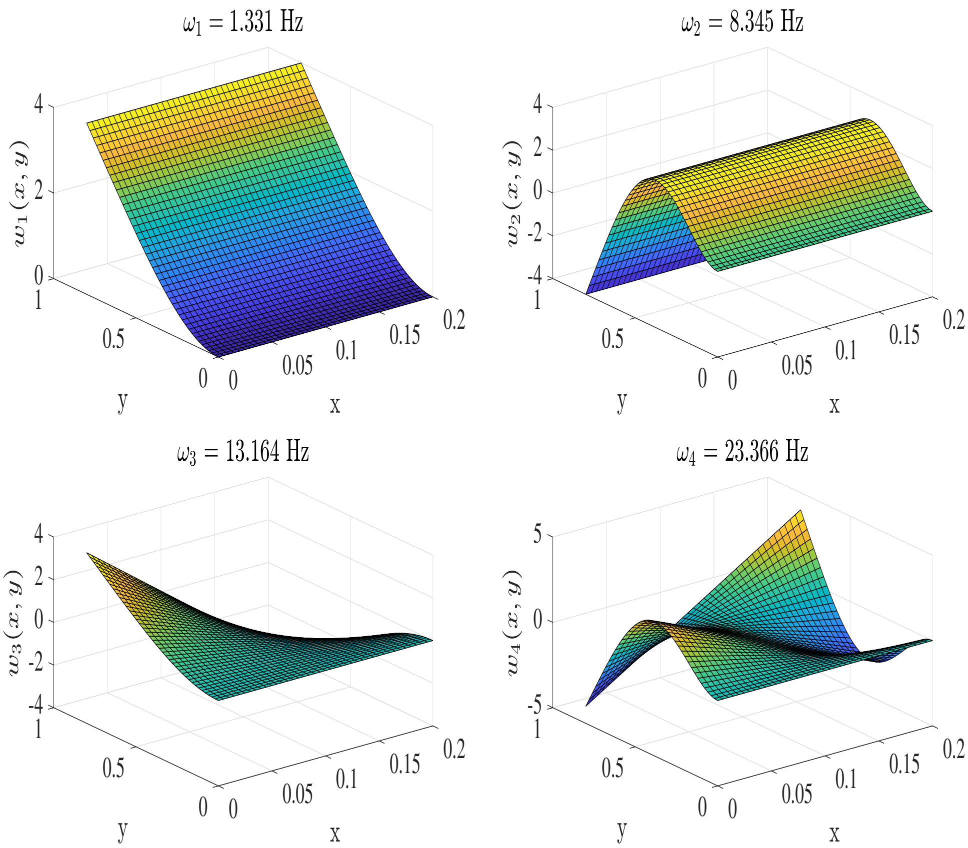


Figure II.9: First four out-of-plane mode shapes of the plate.

The Equations (II.27) can be written in first order form, after setting the nonlinear terms and the constant term equal to 0

$$\dot{\mathbf{x}} = \begin{pmatrix} -\overline{\mathbf{M}}^{-1}\overline{\mathbf{C}} & -\overline{\mathbf{M}}^{-1}\overline{\mathbf{K}} & -\overline{\mathbf{M}}^{-1}\overline{\mathbf{S}}_3 & -\overline{\mathbf{M}}^{-1}\overline{\mathbf{S}}_4 & \cdots & -\overline{\mathbf{M}}^{-1}\overline{\mathbf{S}}_{n_l} \\ \mathbf{I} & \mathbf{0} & \mathbf{0} & \mathbf{0} & \cdots & \mathbf{0} \\ \mathbf{I} & \mathbf{0} & -(U/b)\gamma_1\mathbf{I} & \mathbf{0} & \cdots & \mathbf{0} \\ \mathbf{I} & \mathbf{0} & \mathbf{0} & -(U/b)\gamma_2\mathbf{I} & \cdots & \mathbf{0} \\ \vdots & \vdots & \vdots & \vdots & \ddots & \vdots \\ \mathbf{I} & \mathbf{0} & \mathbf{0} & \mathbf{0} & \cdots & -(U/b)\gamma_{n_l}\mathbf{I} \end{pmatrix} \mathbf{x} \tag{II.34}$$

where $\mathbf{x} = [\dot{\mathbf{r}}^{\mathrm{T}} \ \mathbf{r}^{\mathrm{T}} \ \boldsymbol{\eta}^{\mathrm{T}}]^{\mathrm{T}}$ is the $2m_r + n_l m_r$ aeroelastic state vector. The total number of states is $2m_r + n_l m_r$ and the total mass, damping and stiffness matrices are defined as

$$\overline{\mathbf{M}} = \mathbf{A} - \rho b^2 \mathbf{S}_2, \quad \overline{\mathbf{C}} = -\rho U b \mathbf{S}_1, \quad \overline{\mathbf{K}} = \mathbf{E} - \rho U^2 \mathbf{S}_0$$

while

$$\overline{\mathbf{S}}_3 = -\rho U^2 \mathbf{S}_3, \quad \cdots, \quad \overline{\mathbf{S}} = -\rho U^2 \mathbf{S}_{n_l}$$

Before solving Equation (II.34), the matrices $\mathbf{S}_2$ to $\mathbf{S}_{n_l}$ needed to be evaluated. Recalling Roger's formulation of Equation (II.25), matrix $\mathbf{S}_0$ can be evaluated at $k = 0$, that is

$$\mathbf{S}_0 = \mathbf{Q}_1(0)$$

The other matrices can be computed from curve fitting $\mathbf{Q}_1(k)$ at several non-zero values of $k$, this fitting process is described in detail in [5]. The linear flutter problem can now be solved by evaluating the eigenvalues, $\lambda$, of the system matrix of Equation (II.34) and plotting them against airspeed.
Figure II.10 plots the natural frequencies, $\omega_n = |\lambda|$, and damping ratios, $\xi = -\Re(\lambda)/|\lambda|$, for the first three modes against airspeed. Figure II.10 seems to suggest that the flutter mechanism is binary between modes 1 and 2, respectively first and second bending. If either of these two modes is excluded from the model, flutter will not occur. At flutter the damping ratio of the second bending is zero, while that of the first bending is very high. This means that one pair of complex conjugate eigenvalues has zero real part, exactly as in the case of the Hopf bifurcation. Even if in this case, the natural frequencies of the two modes seems to approach each other and become identical, this is not always necessarily true. It can also happen that the two natural frequencies, involved in the flutter process, approach each other without becoming identical, as also exhaustively explained in [5]. The concept of the binary flutter mechanism, that is two modes combine with each other in order to cause flutter, despite is quite common in nonlinear aeroelasticity, it is still under investigation.

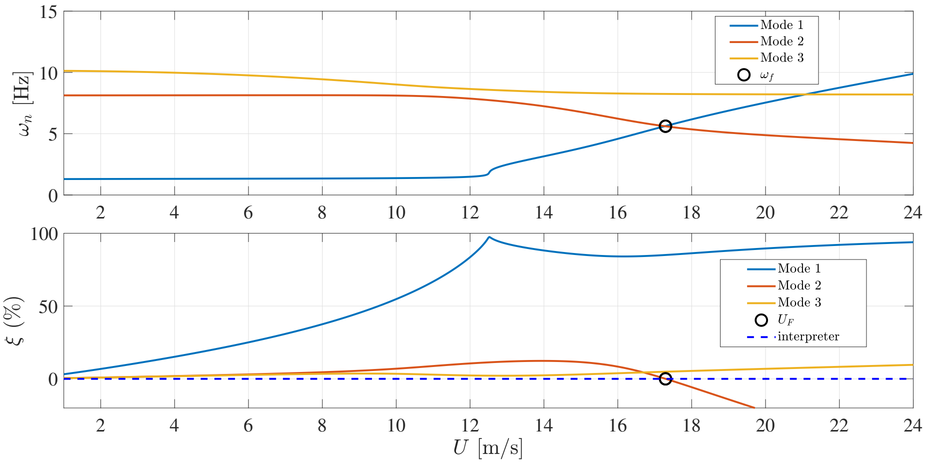


Figure II.10: Natural frequency and damping ratio variation with airspeed for the first three structural modes of the plate.

# Chapter II.3

# Nonlinear results

The complete nonlinear aeroelastic equations were solved using a numerical integration scheme based on the Runge–Kutta–Fehlberg scheme [5]. The solution procedure started at the linear flutter airspeed, where the limit cycle oscillations have zero amplitude and frequency equal to the flutter frequency. The next step was to integrate numerically Equation (II.27) at a slightly higher airspeed $U_f + \Delta_U$ until the response settled onto a steady-state condition and collect the maximum amplitude of the response. Then, the procedure was repeated for gradually higher values of the flow speed. The simulations were performed for $m_x = 4$, $n_y = 4$, $m_v = 20$ and $n_v = 40$.

In Figure II.11 are compared the limit cycle amplitude and period predictions obtained by inextensible plate theory and Von Kármán plate theory. There exist a substantial difference in the order of magnitude of the limit cycle amplitude between the two models. Furthermore, it can be noted that, right after the flutter point, the slope of the amplitude decreases with airspeed for the Von Kármán results while it increases for the inextensible theory predictions. The shape of the LCO amplitude curve obtained by inextensible plate theory is very similar to the one observed in experimental measurements [87], as shown in Figure II.12. The experimental LCO amplitude and the inextensible plate LCO numerical predictions can be compared only qualitatively but not quantitatively since they refer to slightly different flat plates (the experimental results of Figure II.12 refers to an aluminium plate with a sweep angle of 20°, but with the same chord length, span length and thickness).

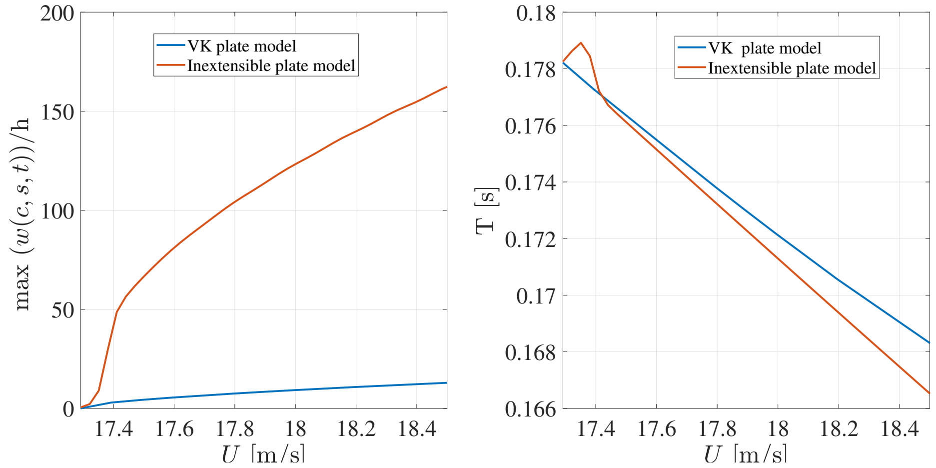


Figure II.11: Comparison between the limit cycle amplitude (left panel) and period (right panel) predictions obtained by inextensible plate theory and Von Kármán plate theory.

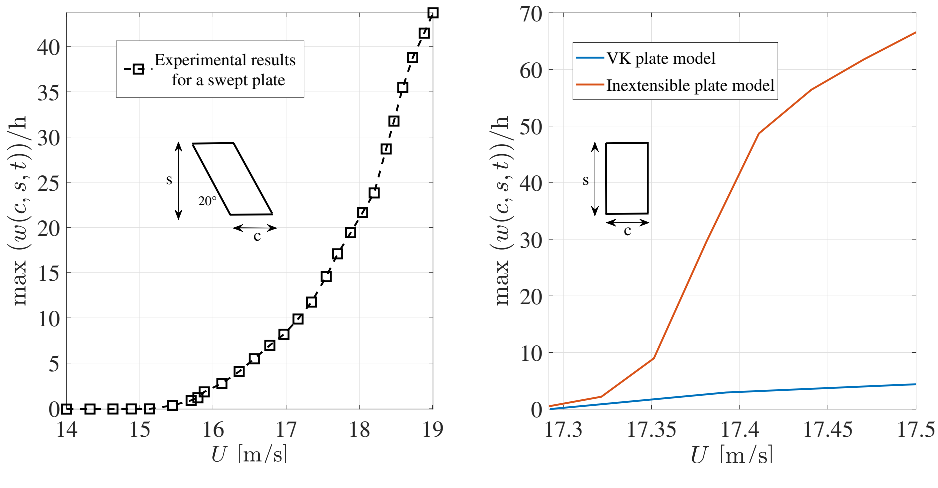


Figure II.12: Qualitative comparison between experimental LCO amplitude obtained for an aluminium swept plate (left panel) and numerical LCO amplitude predictions obtained by Von Kármán plate theory and inextensible plate theory for an unswept aluminium plate (right panel).

# Chapter II.4

# Conclusions

In this second part of the thesis, a closed form state-space model of the nonlinear aeroelastic response of a thin cantilever flat rectangular plate in low speed airflows is presented. The model is based on a combination of inextensible thin plate theory and a linearised continuous time vortex lattice aerodynamic model. Comparison to experimental measurements in a low speed wind tunnel shows that the model predicts the linear flutter airspeed and frequency with reasonable accuracy. The predicted limit cycle amplitude has a very peculiar feature, since the slope of the LCO amplitude vs airspeed curve increases just after the bifurcation point. This kind of behaviour in LCO amplitude was observed in experimental measurements and cannot be predicted employing Von Kármán plate theory as structural model. Unfortunately, reliable experimental tests on LCOs for rectangular cantilever thin plates are not available at the moment, however the results presented here are very encouraging for future experimental and numerical analysis. The model developed here can not only be used to predict LCO amplitudes and frequencies but may also shed light on the nature of the nonlinearities involved in the flutter phenomenon of flat plates or wings.
However, the limitations of the model should always be kept in mind. In order to develop a closed form time-domain set of equations of motion, the aerodynamic forces has been linearised, the fluid has been considered always attached and any viscous effect has been ignored. Thus, any kind of discrepancies between the model predictions and experimental results may be due to unmodelled physics, such as drag effects or stall flutter. Furthermore, the cantilever plate presented here is not a realistic wing or blade. Nevertheless, the methodologies demonstrated here can be extended to more realistic lifting surfaces and the analytical mode shapes, used in the presented work, can be substituted by mode shapes derived from a FE analysis, enabling the model to analyse any shape of plate or wing.

# Final remarks

In this doctoral dissertation, two fluid-structure interaction problems have been presented and analysed. The first linear fluid-structure interaction problem concerns the dynamic behaviour of a QEPAS tuning fork device immersed in a fluid medium, while the second nonlinear fluid-structure interaction problem examines the aeroelastic response of a thin cantilever plate in a low speed airflow. Thus, different modelling techniques have been employed: in the first linear case a novel theoretical-experimental model, based on a Green's function approach, is derived, enabling to easily recognize and control how each parameter of the model influences the overall dynamic behaviour of a quartz tuning fork device vibrating in a fluid environment, while in the second nonlinear case a numerical model, constituted by the combination of the inextensible plate theory and vortex lattice aerodynamic method, is developed in order to correctly predict the limit cycle oscillations of thin cantilever flat plate, after the instability flutter condition.
In the first part, the obtained results show that the proposed theoretical-experimental framework can satisfactorily fit the experimental data, providing a simple, reliable and not computational demanding procedure to characterize the dynamic response of a QTF device operating in a surrounding fluid and, more generally, to describe the fluid-structure interaction of a generic micro-electrical mechanical device. However, the presented methodology is still not fully predictive, since its parameters need to be assessed on experimental or numerical outcomes. As a subsequent step, in the attempt to increase the predictivity the model and allow an easier optimization phase in the design process of future devices, it is planned to analyse different QTF geometries, in order to estimate accurate trends of the model parameters.
In the second part, the simulated amplitude limit cycle, obtained by deploying the inextensible plate theory as structural model, shows an increase of the slope just after the bifurcation point, this peculiar feature has also been observed in experimental results and cannot be modelled with other nonlinear structural models, such as Von Kármán thin plate theory. Since, in literature, reliable experimental outcomes for cantilever rectangular plates are currently not available, only a qualitatively comparison has been made. However, the results here proposed are very promising for future experimental or numerical investigations. The following steps plan to implement FE eigenmodes of the plate, in order to model any kind of structure shape, to set up a proper experimental apparatus, in order to correctly measure the limit cycle oscillations of cantilever flat plates or wings, and to improve the model by considering less linear aerodynamic models which allow the aerodynamic grid and wake to deform and take account of viscous effects or

stall flutter.
Finally, it is possible to conclude that the two fluid structure-interaction problems here proposed, even if profoundly different and related to dissimilar technological applications, they both highlight the strong influence that the presence of a fluid, whether stationary or in motion, can have on the dynamic response of an elastic structure and put emphasis on the importance and increasing need to develop accurate, robust and reliable analytical, experimental and numerical methodologies to analyse the physics of the phenomena related to fluid-structure interaction in the most varied scientific applications.

# List of figures


I.1 QEPAS principle of operation. A QTF is immersed in a fluid and laser light is focused between two QTF prongs. Weak sound waves generated by photoacoustic effect deflect the prong in two opposite directions. . . . . . . . . . . . . . . . . . . . . . . . . . . . . 10

I.2 Reduction of the 3D QTF to a 1D Euler-Bernoulli model. . . . . . . . 13

I.3 Susceptibility function adopted notation. The susceptibility function comprises $G_{11}(x, \xi, \omega)$ and $G_{21}(x, \xi, \omega)$ in the case the unit impulse concentrated force is applied to a generic section $\xi$ of the left cantilever while the right one remains unloaded (left panel); $G_{12}(x, \xi, \omega)$ and $G_{22}(x, \xi, \omega)$ in the case the load is exerted on a section $\xi$ of the right cantilever with the left unforced (right panel). 19

I.4 Magnitudes and phase angles of susceptibility functions $G_{11}(L, L_b/2, \omega)$ (blue curve) and $G_{21}(L, L_b/2, \omega)$ (red curve) of the two cantilevers of QTF#S15, computed by employing as coefficients $\alpha = 2.341 \times 10^{-5}\,\mathrm{Pa\,s}^{3/2}$ and $k = 1.7865 \times 10^{9}\,\mathrm{Pa}$. . . . . . . . . . . . . . . . . . . . . . . . . 20

I.5 1D Euler-Bernoulli model of the fundamental problem. Fundamental problem with an impulsive force applied to a generic section $\xi$ of the left cantilever (left panel), reduction of the fundamental problem to an homogeneous problem (right panel). . . . . . . . . . . . . . 22

I.6 Schematic representation of the adopted experimental setup (left panel) and the real experimental setup (right panel). . . . . . . . . 28

I.7 Real-world constraint of the QTF sensor by two tin weldings (left panel) and adopted constraint by bracket joint (right panel). . . . 28

I.8 The experimentally estimated autoPSD of the displacement measured at the tip of one QTF prong and the mode shape of each detected peak. . . . . . . . . . . . . . . . . . . . . . . . . . . . . 30

I.9 Comparison between the simulated autoPSD of QTF tip displacement computed by using (i) the theoretically modelled external excitation (green curve) and (ii) the measured noise (yellow curve), and the experimental autoPSD of tip displacement (red curve). . . 31

I.10 Modelling of the elastic behaviour of the QTF inferior plate as a distribution of linear springs all subjected to only axial stress. . . 34

I.11 Comparison between the simulated autoPSD of QTF tip displacement computed, in the case $k = Eh/g$, by using (i) the theoretically modelled external excitation (green curve) and (ii) the measured noise (yellow curve), and the experimental PSD of tip displacement (red curve). . . . . . . . . . . . . . . . . . . . . . . . 34
I.12 Computational domain along with moving mesh regions and boundary conditions. . . . . . . . . . . . . . . . . . . . . . . . . . . . . 35
I.13 Real and imaginary parts of hydrodynamic function $\Gamma(\omega)$. Comparison between approximate expression (I.9) evaluated with fitted coefficients collected in Table I.3 (solid line) and CFD numerical results (squared markers). Single summands $\mu$ (dotted line), $\alpha\sqrt{\pi/(2\omega)}$ (dotted-dashed line), and $c/\omega$ (dashed line) of real and imaginary part are represented to elucidate their relative importance. The experimentally estimated PSD (solid dots) is reported to highlight the frequency location of the first QTF skew-symmetric in-plane flexural mode. . . . . . . . . . . . . . . . 37
I.14 Comparison between amplitude of displacement half-spectrum (in red) and amplitude of displacement full-spectrum (in blue), measured at the tip of the QTF. . . . . . . . . . . . . . . . . . . . . 40
I.15 Comparison between phase of displacement half-spectrum (in red) and phase of displacement full-spectrum (in blue), measured at the tip of the QTF. . . . . . . . . . . . . . . . . . . . . . . . . . 41
I.16 Schematic layout of the measured points. All the points are equally spaced along the prong. . . . . . . . . . . . . . . . . . . . . . 42
I.17 Stabilisation diagram computed by applying the PolyMAX method to the displacement half-spectrum of the tip of the QTF. . . . . . 43
I.18 MAC for the three identified modes in the stabilisation diagram. . 44
I.19 QEPAS mode shape of a single prong of the QTF, reconstructed with the PolyMAX estimation technique. . . . . . . . . . . . . . . 45

II.1 An example of fluttering wing in a wind tunnel, Test to Destruction: "Aeroelasticity Matters", 1981 NASA Langley Wind Tunnel Tests 49
II.2 The iconic collapse of the Tacoma Narrows Bridge on November 7, 1940, as a result of aeroelastic flutter caused by a 42 mph (68 km/h) wind. . . . . . . . . . . . . . . . . . . . . . . . . . . . . . . . . 50
II.3 Accuracy versus computational cost of different fluid modelling options (adapted from Ref. [83]). . . . . . . . . . . . . . . . . . . 51

II.4 Plate geometry and deformation (adapted from Ref. [5]). . . . . . . 54
II.5 Comparison between the static deflection of a cantilever plate obtained with (i) linear model (blue curve), (ii) nonlinear Von Kármán's plate model (brown curve), (ii) nonlinear inextensible plate model (red curve), (iii) experiments (black squared markers). . . 58

II.6 Comparison between the numerical results obtained for the dynamic deflection of a cantilever plate with increasing excitation frequency using the inextensible plate model (solid curves) and those published by Tang et al. [91] for the same case (dashed curves and squared markers). . . . . . . . . . . . . . . . . . . . . . . . . . . 59
II.7 Comparison between the numerical results obtained for the dynamic deflection of the plate with decreasing excitation frequency using the inextensible plate model (solid curves) and those published by Tang et al. [91] for the same case (dashed curves and squared markers). . . . . . . . . . . . . . . . . . . . . . . . . . . . . . . 59
II.8 Wing discretization for the Vortex Lattice method (adapted from Ref. [87]). . . . . . . . . . . . . . . . . . . . . . . . . . . . . . . 61
II.9 First four out-of-plane mode shapes of the plate. . . . . . . . . . . 67
II.10 Natural frequency and damping ratio variation with airspeed for the first three structural modes of the plate. . . . . . . . . . . . . 69
II.11 Comparison between the limit cycle amplitude (left panel) and period (right panel) predictions obtained by inextensible plate theory and Von Kármán plate theory. . . . . . . . . . . . . . . . . . . . . 71
II.12 Qualitative comparison between experimental LCO amplitude obtained for an aluminium swept plate (left panel) and numerical LCO amplitude predictions obtained by Von Kármán plate theory and inextensible plate theory for an unswept aluminium plate (right panel). . . . . . . . . . . . . . . . . . . . . . . . . . . 71

# List of tables

I.1 Dimensions of the QTF#S15 device used in this work, the nomenclature refers to Figure I.2. . . . . . . . . . . . . . . . . . . . . . . . 18

I.2 Values of fluid model coefficient and structural coupling stiffness which fit the experimental response. . . . . . . . . . . . . . . . . . . 31
I.3 Values of fluid model coefficients which fit the CFD numerical results. 36
I.4 Damping factors and quality factors of the QEPAS mode for the seven points acquired in the experimental test campaign. The numbering of the points refers to Figure I.16. . . . . . . . . . . . . . 44

II.1 Variation of flutter speed with number of chordwise and spanwise panels. . . . . . . . . . . . . . . . . . . . . . . . . . . . . . . . . . 66
II.2 Variation of flutter speed with number out-of-plane modes. . . . . 67

# Bibliography


[1] A. Campanale, C. Putignano, S. D. Carolis, P. Patimisco, M. Giglio, L. Soria, A theoretical-experimental framework for the analysis of the dynamic response of a QEPAS tuning fork device immersed in a fluid medium, *Mechanical Systems and Signal Processing*, 149, 107298, 2021.

[2] A. Campanale, L. Soria, G. Kerschen, G. Dimitriadis, Modelling the limit cycle oscillations of flat plate wings using inextensible plate theory and the vortex lattice method, *International Conference on Noise and Vibration Engineering ISMA 2020*, Leuven, Belgium, September 2020.

[3] Y. Bazilevs, K. Takizawa, T. E Tezduyar, *Computational fluid-structure interaction: methods and applications*, John Wiley & Sons, 2013.

[4] L. D. Landau, E. M. Lifshitz, *Fluid Mechanics*, 2nd ed., Pergamon Press, 1984.

[5] G. Dimitriadis, *Introduction to nonlinear aeroelasticity*, Chichester, West Sussex, UK: John Wiley & Sons, Inc., 2017.

[6] R. L. Campbell, E. G. Paterson, Fluid–structure interaction analysis of flexible turbomachinery, *Journal of Fluids and Structures*, 27(8), pp. 1376-1391, 2011.

[7] A. Castorrini, A. Corsini, F. Rispoli, K. Takizawa, T. E. Tezduyar, A stabilized ALE method for computational fluid–structure interaction analysis of passive morphing in turbomachinery, *Mathematical Models and Methods in Applied Sciences*, 29(5), pp. 967-994, 2019.

[8] T. Abbas, I. Kavarkov, G. Morgenthal, Methods for flutter stability analysis of long-span bridges: a review, *Bridge Engineering*, 170(4), pp. 271-310, 2017.

[9] S.Pourzeynali, K. T. Datta, Control of suspension bridge flutter instability using pole-placement technique, *Journal of Sound and Vibration*, 282, pp. 89-109, 2005.

[10] T. J. A. Agar, Aerodynamic flutter analysis of suspension bridges by a modal technique, *Engineering Structures*, 11(2), pp. 75-82, 1989.

[11] H. Suito, K. Takizawa, V. Q. H. Huynh, D. Sze, T. Ueda, FSI analysis of the blood flow and geometrical characteristics in the thoracic aorta, *Computational Mechanics*, 54, pp. 1035-1045, 2014.

[12] S. Basak, A. Raman, Dynamics of tapping mode atomic force microscopy in liquids: Theory and experiments, *Appl. Phys. Lett.*, 91, 064107, 2007.

[13] A. Stylianou, S. V. Kontomaris, C. Grant, E. Alexandratou, Atomic Force Microscopy on Biological Materials Related to Pathological Conditions, *Scanning*, 91, 845251, 2019.

[14] E. Pierro, F. Bottiglione, G. Carbone, Thermal fluctuations and dynamic modelling of a dAFM cantilever, *Advanced Theory and Simulations*, 2(5), 1900004, 2019.

[15] J. Hodgkinson, R. P. Tatam, Optical gas sensing: a review, *Meas. Sci. Technol.*, 24(1), 012004, 2013.

[16] J. E. Sader, *J. Appl. Phys*, 84, 64, 1998.

[17] M. Kimber, R. Lonergan, S. V. Garimella, *J. Fluids Struct.*, 5, 1334, 2009.

[18] C. Castille, I. Dufour, C. Lucat, *Appl. Phys. Lett.*, 96, 154102, 2010.

[19] M. Kimber, S. V. Garimella, A. Raman, *Trans. ASME, Ser. C: J. Heat-Transf.*, 129, 1168, 2007.

[20] P.Rojratsirikul, M.S.Genca, Z.Wang, I.Gursul, Flow-induced vibrations of low aspect ratio rectangular membrane wings, *Journal of Fluids and Structures*, 27(8), pp. 1296-1309, 2011, https://doi.org/10.1115/1.3265570.

[21] K. J. Sohn, J. H. Kim, Nonlinear thermal flutter of functionally graded panels under a supersonic flow, *Composite Structures*, 88(3), pp. 380-387, 2009.

[22] J. S. Park, J. H. Kim, S. H. Moon, Thermal post-buckling and flutter characteristics of composite plates embedded with shape memory alloy fibers, *Composites Part B: Engineering*, 36(8), pp. 626-636, 2005.

[23] A. Joly, S. Etienne, D. Pelletier, Galloping of square cylinders in cross-flow at low Reynolds numbers, *Journal of Fluid and Structures*, 28, pp. 232-243, 2012.

[24] I. Robertson, L. Li, S. J. Sherwin, P. W. Bearman, A numerical study of rotational and transverse galloping rectangular bodies, *Journal of Fluid and Structures*, 17(5), pp. 681-699, 2003.

[25] R. v. Loon, P. D. Anderson, F. N. v. d. Vosse, S.J.Sherwin, Comparison of various fluid–structure interaction methods for deformable bodies, *Computers and Structures*, 85(11-14), pp. 833-843, 2007, https://doi.org/10.1016/j.compstruc.2007.01.010.

[26] G. Hou, J. Wang, A. Layton, Numerical Methods for Fluid-Structure Interaction - A Review, *Communications in Computational Physics*, 12(2), pp. 337-377, 2012, https://doi.org/10.4208/cicp.291210.290411s.

[27] A. Nitti, J. Kiendl, A. Reali, M. D. de Tullio, An immersed-boundary/isogeometric method for fluid-structure interaction involving thin shells, *Computer Methods in Applied Mechanics and Engineering*, 364, 112977, 2020.

[28] E. O. Tuck, *J. Eng. Math.*, 3, 29, 1969.

[29] R. J. Clarke, S. M. Cox, P. M. Williams, O. E. Jensen, *J. Fluid. Mech.*, 545, 397, 2005.

[30] A.G. Bell, On the Production and Reproduction of Sound by Light, *Am. J. Sci.*, 20, 305, 1880.

[31] A.G. Bell, Upon the Production of Sound by Radiant Energy, *Philos. Mag.*, 11, 510, 1881.

[32] Y.H. Pao, Optoacoustic Spectroscopy and Detection (Academic, New York, 1977).

[33] S. Schäfer, A. Miklos, P. Hess, Progress in Photothermal and Photoacoustic Science and Technology (SPIE, Bellingham, WA, 1997), Vol. III.

[34] A.A. Kosterev, Y.A. Bakhirkin, R.F. Curl, F.K. Tittel, Quartz-enhanced photoacoustic spectroscopy, *Optics Letters*, 27 (21), pp. 1902-1904, 2002.

[35] A.A. Kosterev, F.K. Tittel, D.V. Serebryakov, A.L. Malinovsky, I.V. Morozov, Applications of quartz tuning forks in spectroscopic gas sensing, *Rev. Sci. Instrum.*, 76, 043105, 2005.

[36] A. Elia, P.M. Lugarà, C.D. Franco, V. Spagnolo, Photoacoustic Techniques for Trace Gas Sensing Based on Semiconductor Laser Sources, *Sensors*, 9, pp. 9616-9628, 2009.

[37] P. Patimisco, A. Sampaolo, L. Dong, F.K. Tittel, V. Spagnolo, Recent advances in quartz enhanced photoacoustic sensing, *Appl. Phys. Rev.*, 5, 011106, 2018.

[38] S. Borri, P. Patimisco, A. Sampaolo, H. E. Beere, D. A. Ritchie, M. S. Vitiello, G. Scamarcio, V. Spagnolo, Terahertz quartz enhanced photoacoustic sensor, *Appl. Phys. Lett.*, 103, 02110, 2013.

[39] P. Patimisco, G. Scamarcio, V. Spagnolo, Quartz-enhanced photoacoustic spectroscopy: a review, *Sensors*, 4, pp. 6165-6206, 2014.

[40] P. Patimisco, A. Sampaolo, H. Zheng, L. Dong, F.K. Tittel, V. Spagnolo, Quartz enhanced photoacoustic spectrophones exploiting custom tuning forks: a review, *Adv. Phys. X*, 2, pp. 169-187, 2017.

[41] M. Giglio, G. Menduni, P. Patimisco, A. Sampaolo, A. Elefante, V.M.N. Passaro, V. Spagnolo, Damping Mechanisms of Piezoelectric Quartz Tuning Forks Employed in Photoacoustic Spectroscopy for Trace Gas Sensing, *Phys. Status Solidi A*, 216, 1800552, 2019.

[42] P. Patimisco, A. Sampaolo, V. Mackowiak, H. Rossmadl, A. Cable, F. K. Tittel, V. Spagnolo, Loss Mechanisms Determining the Quality Factors in Quartz Tuning Forks Vibrating at the Fundamental and First Overtone Modes, *IEEE Transactions on Ultrasonics, Ferroelectrics, and Frequency Control*, 65(10), 2018.

[43] S. Kirstein, M. Mertesdorf, M. Schoenhoff, *J. Appl. Phys*, 84, 1782, 1998.

[44] A. Maali, C. Hurth, R. Boisgard, C. Jai, T. Cohen-Bouhacina, J.-P.Aime, *J. Appl. Phys*, 97, 074907, 2005.

[45] S. Basak, A. Raman, S. V. Garimella, Hydrodynamic loading of microcantilevers vibrating in viscous fluids, *J. Appl. Phys*, 99(11), 114906, 2006.

[46] M. Kimber, S. V. Garimella, *Int. J. Heat Mass Transf.*, 52, 4470, 2009.

[47] R. A. Bidkar, M. Kimber, A. Raman, A. K. Bajaj, S. V. Garimella, *J.Fluid Mech.*, 634, 269, 2009.

[48] P. Brunetto, L. Fortuna, S. Graziani, S. Strazzeri, *Smart Mater. Struct.*, 17, 025029, 2008.

[49] D. Akaydin, N. Elvin, Y. Andreopoulos, *J. Intell. Mater. Syst.Struct.*, 10, 1263, 2010.

[50] M. Aureli, C. Prince, M. Porfiri, and S. D. Peterson, *Smart Mater. Struct.*, 19, 015003, 2010.

[51] A. Giacomello and M. Porfiri, *Smart Mater. Struct.*, 109, 084903, 2011.

[52] R. J. Clarke, O. E. Jensen, J. Billingham, A. P. Pearson, P. M. Williams, *Phys. Rev. Lett*, 96, 050801, 2006.

[53] S. M. Han, H. Benaroya, *J. Sound Vib.*, 237, 837, 2000.

[54] S. M. Han, H. Benaroya, *J. Sound Vib.*, 237, 875, 2000.

[55] M. Aureli, M. Porfiri, *Appl. Phys. Lett.*, 96, 164102, 2010.

[56] M. Aureli, M. E. Basaran, M. Porfiri, *J. Sound Vib.*, 331, 1624, 2012.

[57] C. Intartaglia, L. Soria, M. Porfiri, Hydrodynamic coupling of two sharp-edged beams vibrating in a viscous fluid, *Proceedings of the Royal Society A: Mathematical, Physical and Engineering Sciences*, 470(2162), 20130397, 2014.

[58] F. Cellini, C. Intartaglia, L. Soria, M. Porfiri, Effect of hydrodynamic interaction on energy harvesting in arrays of ionic polymer metal composites vibrating in a viscous fluid, *Smart materials and structures*, 23(4), 045015, 2014.

[59] P. K. Banerjee, P. K. Banerjee, R. Butterfield, Boundary element methods in engineering science (McGraw-Hill Book Co, 1981).

[60] R. Lanzafame, M. Messina, Fluid dynamics wind turbine design: Critical analysis, *Renewable Energy*, 32(14), pp. 2391-2305, 2007.

[61] O. Czygan, O. V. Estorff, Fluid-structure interaction by coupling BEM and nonlinear FEM, *Engineering Analysis with Boundary Elements*, 26(9), pp. 773-779, 2002.

[62] R. N. Simpson, M. A. Scott, M. Taus, D. C. Thomas, H.Lian, Acoustic isogeometric boundary element analysis, *Computer Methods in Applied Mechanics and Engineering*, 269, pp. 265-290, 2014.

[63] D. Fritze, S. Marburg, H. J. Hardtke, FEM-BEM-coupling and structural–acoustic sensitivity analysis for shell geometries, *Computers and Structures*, 83(2-3), pp. 143-154, 2005.

[64] M. Chiampi, L. Zilberti, Induction of Electric Field in Human Bodies Moving Near MRI: An Efficient BEM Computational Procedure, *IEEE Transactions on Biomedical Engineering*, 58(10), pp. 2787-2793, 2011.

[65] A. Buffa, R. Hiptmair, Galerkin Boundary Element Methods for Electromagnetic Scattering, *Topics in Computational Wave Propagation*, 31, pp. 83-124, 2002.

[66] G. E. Bird, J.Trevelyan, C.E.Augarde, A coupled BEM/scaled boundary FEM formulation for accurate computations in linear elastic fracture mechanics, *Engineering Analysis with Boundary Elements*, 34(6), pp. 599-610, 2010.

[67] Y. Mi, M. H. Aliabadi, Dual boundary element method for three-dimensional fracture mechanics analysis, *Engineering Analysis with Boundary Elements*, 10(2), pp. 161-171, 1992.

[68] C. Putignano, G. Carbone, D. Dini, Theory of reciprocating contact for viscoelastic solids, *Phys. Rev. E*, 93(4), 043003, 2016.

[69] C. Putignano, Soft lubrication: A generalized numerical methodology, *Journal of the Mechanics and Physics of Solids*, 134, 103748, 2020.

[70] C. Putignano, J. Le Rouzic, T. Reddyhoff, G. Carbone, D. Dini, A theoretical and experimental study of viscoelastic rolling contacts incorporating thermal effects, Proceedings of the Institution of Mechanical Engineers, *Part J: Journal of Engineering Tribology*, 2014, https://doi.org/10.1177/1350650114530681.

[71] J. T. Katsikadelis, M. S. Nerantzaki, The boundary element method for nonlinear problems, *Engineering Analysis with Boundary Elements*, 23(5-6), pp. 365-373, 1999.

[72] M. Dehghan, R. Salehi, A meshless based numerical technique for traveling solitary wave solution of Boussinesq equation, *Applied Mathematical Modelling*, 36(5), pp. 1939-1956, 2012.

[73] Q. Ding, D. L. Wang, The flutter of an airfoil with cubic structural and aerodynamic non-linearities, *Aerospace Science and Technology*, 11(5), pp. 427-434, 2006.

[74] B. Gjerek, R. Drazumeric, Flutter behavior of a flexible airfoil: Multiparameter experimental study, *Aerospace Science and Technology*, 36(5), pp. 75-86, 2014.

[75] J. M. McCarthy, S. Watkins, A. Deivasigamani, S. J. John, Fluttering energy harvesters in the wind: A review, *Journal of Sound and Vibration*, 361, pp. 355-377, 2016.

[76] A. I. Aquino, J. K. Calautit, B. R. Hughes, Evaluation of the integration of the Wind-Induced Flutter Energy Harvester (WIFEH) into the built environment: Experimental and numerical analysis, *Applied Energy*, 207, pp. 61-77, 2017.

[77] E. Albano, W. P. Rodden, A doublet-lattice method for calculating lift distributions on oscillating surfaces in subsonic flows, *AIAA Journal*, 7(2), 1969.

[78] J. Katz, A. Plotkin, *Low Speed Aerodynamics*, Cambridge University Press, 2001.

[79] J. Murua, R. Palacios, J. M. R. Graham, Applications of the unsteady vortex-lattice method in aircraft aeroelasticity and flight dynamics, *Progress in Aerospace Sciences*, 55, pp. 46-72, 2012.

[80] T. E. Fritz, L. N. Long, Object-oriented Unsteady Vortex Lattice Method for flapping flight, *Journal of Aircraft*, 41(6), pp. 1275-1290, 2004.

[81] D. J. Willis, J. Peraire, J. K. White, A combined pFFT-multipole tree code, unsteady panel method with vortex particle wake, *International Journal for Numerical Methods in Fluids*, 53, pp. 1399-1422, 2007.

[82] B. K. Stanford, P. S. Beran, Analytical sensitivity analysis of an Unsteady Vortex Lattice Method for flapping wing optimization, *Journal of Aircraft*, 47(2), pp. 647-662, 2010.

[83] B. P. Eppsa, B. T. Roeslera, R. B. Medvitzb, Y. Chooa, J. McEntee, A viscous vortex lattice method for analysis of cross-flow propellersand turbines, *Renewable Energy*, 143, pp. 1035-1052, 2019.

[84] F. J. Simoes, J. M. R. Graham, Application of a free vortex wake model to a horizontal axis wind turbine, *Journal of Wind Engineering and Industrial Aerodynamics*, 39(1-3), pp. 129-138, 1992.

[85] S. D. Pesmajoglou, J. M. R. Graham, Prediction of aerodynamic forces on horizontal axis wind turbines in free yaw and turbulence, *Journal of Wind Engineering and Industrial Aerodynamics*, 86(1), pp. 1-14, 2000.

[86] G. Dimitriadis, N. F. Giannelis, G. A. Vio, A modal frequency-domain generalised force matrix for the unsteady Vortex Lattice method, *Journal of Fluids and Structures*, 76, pp. 216-228, 2018.

[87] G. N. Giannelis, G. A. Vio, G. Dimitriadis, Limit cycle oscillations of cantilever rectangular plates in a wind tunnel, *International Forum on Aeroelasticity and Structural Dynamics*, 2017.

[88] E. De Oro Fernandez, T. Andrianne, G. Dimitriadis, A database of flutter characteristics for simple low and medium aspect ratio wings at low speeds, *AIAA SciTech 2020, Orlando Florida*, January 2020.

[89] M. P. Paidoussis, Fluid-Structure Interactions: Slender Structures and Axial Flow, Vol. 2, Academic Press, New York, pp. 1137–1221, 2004.

[90] D. Tang, H. Yamamoto, E. H. Dowell, Flutter and Limit Cycle Oscillations of Two-Dimensional Panels in Three-Dimensional Flow, *Journal of Fluids and Structures*, 17(2), pp. 225–242, 2003.

[91] D. Tang, M. Zhao, E. H. Dowell, Inextensible Beam and Plate Theory: Computational Analysis and Comparison With Experiment, *Journal of Applied Mechanics*, 81(6), 051007, 2014.

[92] T. V. Kármán, "Festigkeitsprobleme in Maschinenbau", F. Klein (ed.) C. Müller (ed.), Encyklopädie der Mathematischen Wissenschaften, IV/4 , Teubner, pp. 311–385, 1910.

[93] P. Daukantas, Air-quality monitoring in the mid-infrared, *Opt. Photonics News*, 26(11), pp. 26-33, 2015.

[94] L. Zhang, G. Tian, J. Li, B. Yu, Applications of absorption spectroscopy using quantum cascade lasers, *Appl. Spectrosc.*, 68, pp. 1095-1107, 2014.

[95] M. Jahjah, W. Jiang, N.P. Sanchez, W. Ren, P. Patimisco, V. Spagnolo, S.C. Herndon, R.J. Griffin, F.K. Tittel, Atmospheric CH4 and N2O measurements near Greater Houston area landfills using a QCL based QEPAS sensor system during DISCOVER-AQ 2013, *Opt. Lett.*, 39, pp. 957-960, 2014.

[96] A. Sampaolo, S. Csutak, P. Patimisco, M. Giglio, G. Menduni, V. Passaro, F. K. Tittel, M. Daffenbaugh, V. Spagnolo, Methane, ethane and propane detection using a compact quartz enhanced photoacoustic sensor and a single interband cascade laser, *Sensors and Actuators B: Chemical*, 282, pp. 952-960, 2019.

[97] J. Mikołajczyk, Z. Bielecki, T. Stacewicz, J. Smulko, J. Wojtas, D. Szabra, L. Lentka, A. Prokopiuk, P. Magryta, Detection of gaseous compounds with different techniques, *Metrology and Measurement Systems*, 23, 205-224, 2016.

[98] T.D. Rossing, D.A. Russell, D.E. Brown, On the acoustics of tuning forks, *Am. J. Phys.*, 60, 620-626, 1992.

[99] L. Soria, E. Pierro, G. Carbone, T. Contursi, Tuning fork microgyrometers: narrow gap vs. wide gap design, *Journal of Sound and Vibrations*, 322 (1-2), pp. 78-97, 2009.

[100] F. R. Blom, S. Bouwstra, M. Elwenspoek, J. H. J. Fluitman, Dependence of the quality factor of micromachined silicon beam resonators on pressure and geometry, *J. Vac. Sci. Technol. B*, 10, 19, 1992.

[101] H. Hosaka, K. Itao, S. Kuroda, Damping Characteristics of Beam-Shaped Micro-Oscillators, *Sensors and Actuators A: Physical*, 49, pp. 87-95, 1995.

[102] K. Kokubun, H. Murakami, Y. Toda, M. Ono, A bending and stretching mode crystal oscillator as a friction vacuum gauge, *Vacuum*, 34, pp. 731-735, 1984.

[103] Y. Jimbo, K. Itao, Energy loss of a cantilever vibrator, *J. Horological Inst. Jpn*, 47, 1, 1968.

[104] D. M. Photiadis, J. A. Judge, Attachment losses of high Q oscillators, *Appl. Phys. Lett.*, 85, 482, 2005.

[105] Z. Hao, A. Erbil, F. Ayazi, An analytical model for support loss in micromachined beam resonators with in-plane flexural vibrations, *Sensors and Actuators A: Physical*, 109, 156-164, 2003.

[106] C. Zener, Internal friction in solids II. General theory of thermoelastic internal friction, *Phys. Rev.*, 53, pp. 90-99, 1938.

[107] P. Patimisco, A. Sampaolo, L. Dong, M. Giglio, G. Scamarcio, F. K. Tittel, V. Spagnolo, Analysis of the electro-elastic properties of custom quartz tuning forks for optoacoustic gas sensing, *Sensors and Actuators B: Chemical*, 227, pp. 539-546, 2016.

[108] E. G. Santos, D. Ramos, V. Pini, M. Calleja, J. Tamayo, Exponential tuning of the coupling constant of coupled microcantilevers by modifying their separation *Appl. Phys. Lett.*, 98, 123108, 2011.

[109] S. Inceloglu, M. Gurgoze, Bending Vibrations of Beams Coupled by a Double Spring-Mass System, *Journal of Sound and Vibration*, 243 (2), pp. 361-369, 2001.

[110] G. G. Stokes, On the Effect of the Internal Friction of Fluids on the Motion of Pendulums, *Transactions of the Cambridge Philosophical Society*, Part II, 9, 8-106, 1851.

[111] C. Y. Wang, Exact solutions of the steady-state Navier-Stokes equations, *Annual Review of Fluid Mechanics*, 23, 159-177, 1991.

[112] Y. Zeng and S. Weinbaum, Stokes problems for moving half-planes, *J. Fluid Mech.*, 287, 59-74, 1995.

[113] L. Rosenhead, Laminar boundary layers, *J. Fluid Mech.*, Oxford: Clarendon, 1963.

[114] R. P. Kanwal, *Z. Angew. Math. Mech*, 35, 17, 1955.

[115] A. Raman,J. Melcher, R. Tung, Cantilever dynamics in atomic force microscopy, *Nano Today*, 3(1-2), 20-27, 2008.

[116] C. A. V. Eysden, J. E. Sader, Frequency response of cantilever beams immersed in viscous fluids with applications to the atomic force microscope: Arbitrary mode order, *J. Appl. Phys*, 101, 044908, 2007.

[117] E. Grimaldi, M. Porfiri, L. Soria, Finite amplitude vibrations of a sharp-edged beam immersed in a viscous fluid near a solid surface, *Journal of Applied Physics*, 112 (10), 104907, 2012.

[118] L. Meirovitch, Fundamentals of Vibrations (McGraw-Hill, 1975).

[119] P. Patimisco, S. Borri, A.Sampaolo, H. E. Beere, D. A. Ritchie, M. S. Vitiello, G. Scamarcio, V. Spagnolo, A quartz enhanced photo-acoustic gas sensor based on a custom tuning fork and a terahertz quantum cascade laser, *Sensors and Actuators B: Chemical*, 139, 2079, 2014.

[120] R. Cox, J. Zhang, F. Josse, S. M. Heinrich, I. Dufour, L. A. Beardslee, O. Brand, Damping and mass sensitivity of laterally vibrating resonant microcantilevers in viscous liquid media, *Proceedings of the IEEE International Frequency Control Symposium and Exposition*, 2011.

[121] R. Cox, J. Zhang, F. Josse, S. M. Heinrich, O. Brand, I. Dufour, Characteristics of laterally vibrating resonant microcantilevers in viscous liquid media, *Journal of Applied Physics*, 111(1), 014907, 2012.

[122] M. Napoli, W. Zhang, K. Turner, Characterization of Electrostatically Coupled Microcantilevers, *Journal of Microelectromechanical Systems*, 14(2), 295, 2005.

[123] P. Patimisco, A. Sampaolo, M. Giglio, S. Dello Russo, V. Mackowiak, H. Rossmadl, A. Cable, F.K. Tittle, V. Spagnolo, Tuning forks with optimized geometries for quartz-enhanced photoacoustic spectroscopy, *Opt. Express*, 27, pp. 1401-1415, 2019.

[124] S. Dello Russo, M. Giglio, A. Sampaolo, P. Patimisco, G. Menduni, H. Wu, L. Dong, V. M. N. Passaro, V. Spagnolo, Acoustic Coupling between Resonator Tubes in Quartz-Enhanced Photoacoustic Spectrophones Employing a Large Prong Spacing Tuning Fork, *Sensors*, 19(19), 4109, 2019.

[125] F. Shen, M. Zheng, D. Feng Shi, F. Xu, Using the cross-correlation technique to extraction modal parameters pn response-only data, *Journal of Sound and Vibration*, 259(5), pp. 1163-1179, 2003.

[126] B. Peeters, H. V. d. Auweraer, PolyMAX: a revolution in operational modal analysis, *Proceedings of the 1st International Conference on Operational Modal Analysis*, Copenhagen, Denmark, 26-27 April 2005.

[127] L. Soria, B. Peeters, J, Anthonis, H. V. d. Auweraer, Operational Modal Analysis and the performance assessment of vehicle suspension systems, *Shock and Vibration*, 19, pp. 1099–1113, 2012.

[128] A.V. Oppenheim, R.W. Schafer, *Discrete-Time Signal Processing*, Prentice-Hall, 1999.

[129] L. Hermans, H. V. d. Auweraer, P. Guillaume, A frequency-domain maximum likelihood approach for the extraction of modal parameters from output-only data, *Proceedings of ISMA 23*, 367-376, Leuven, Belgium, 16–18 September 1998.

[130] E. Parloo, *Application of frequency-domain system identification techniques in the field of operational modal analysis, PhD thesis*, Dept. of Mechanical Engineering, Vrije Universiteit Brussel, Belgium, 2003.

[131] B. Cauberghe, *Applied frequency-domain system identification in the field of experimental and operational modal analysis*, PhD thesis, Department of Mechanical Engineering, V.U.Brussel, Belgium, 2004.

[132] W. Heylen, S. Lammens, P. Sas, *Modal Analysis Theory and Testing*, K.U.Leuven, Belgium, 2007.

[133] L. Schouveiler, F. Chermette, Flutter instability of freely hanging articulated pipes conveying fluid, *Physics of Fluids*, 30(3), 034105, 2018.

[134] M. Shubov, Flutter Phenomenon in Aeroelasticity and Its Mathematical Analysis, *Journal of Aerospace Engineering*, 19(1), 2006.

[135] M. Shubov, Mathematical Modeling and Analysis of Flutter in Long-Span Suspension Bridges and in Blood Vessel Walls, *Journal of Aerospace Engineering*, 17(2), 2004.

[136] R. F. Feria, E. S. Rojas, Comparison of aerodynamic models for two-dimensional pitching foils with experimental data, *Physics of Fluids*, 31, 057104, 2019.

[137] C. W. Stammers, The Flutter of a Helicopter Rotor Blade in Forward Flight, *The Aeronautical Journal*, 21(1), pp. 18-48, 1970.

[138] X. Chen, A. Kareem, Advances in Modeling of Aerodynamic Forces on Bridge Decks, *Journal of Engineering Mechanics*, 328(11), 1193-1205, 2002.

[139] B. Jones, *Elements of Practical Aerodynamics*, UK: John Wiley & Sons, Inc., 1939.

[140] M. Drela, Integrated Simulation Model for Preliminary Aerodynamic, Structural, and Control-Law Design of Aircraft, AIAA Paper 99-1394; AIAA: Reston, VA, USA, 1999.

[141] E. Reissner, Effect of finite span on the airload distributions for oscillating wings. I - Aerodynamic theory of oscillating wings of finite span, NACA TN 1194, 1947.

[142] E. Reissner, J. E. Stevens, Effect of finite span on the airload distributions for oscillating wings. II - Methods of calculation and examples of application, NACA TN 1195, 1947.

[143] A. Röttgermann, R. Behr, Schöttl, S. Wagner, Calculation of blade-vortex interaction of rotary wings in incompressible flow by an Unsteady Vortex Lattice Method including free wake analysis, *Notes on numerical fluid mechanics*, 33, pp. 153-166, 1992.

[144] S. Y. Wie, S. Lee, D. J. Lee, Potential panel and time-marching free-wake coupling analysis for helicopter rotor, *Journal of Aircraft*, 46(3), pp. 1030-1041, 2009.

[145] F. N. Coton, T. Wang, The prediction of horizontal axis wind turbine performance in yawed flow using an unsteady prescribed wake model, *Journal of Power and Energy*, 213, pp. 33-43, 1999.

[146] I. Grant, M. Mo, X. Pan, P. Parkin, J. Powell, H. Reinecke, K. Shuang, F. Coton, D. Lee, An experimental and numerical study of the vortex filaments in the wake of an operational, horizontal-axis, wind turbine, *Journal of Wind Engineering and Industrial Aerodynamics*, 85(2), 177-189, 2000.

[147] K. Rados, G. Larsen, R. Barthelmie, W. Schlez, B. Lange, G. Schepers, T. Hegberg, M. Magnisson, Comparison of wake models with data for offshore wind farms, *Wind Engineering*, 25(5), pp. 271-280, 2001.

[148] M. O. L. Hansen, J. N. Sørensen, S. Voutsinas, N. Sørensen, H. A. Madsen, State of the art in wind turbine aerodynamics and aeroelasticity, *Progress in Aerospace Science*, 42(4), pp. 285-330, 2006.

[149] R. Palacios, J. Murua, R. Cook, Structural and aerodynamic models in nonlinear flight dynamics of very flexible aircraft, *AIAA J.*, 48, pp. 2648-2659, 2010.

[150] C. S. Prasad, Q.-Z. Chen, O. Bruls, F. D'Ambrosio, G. Dimitriadis, Aeroservoelastic simulations for horizontal axis wind turbines, *Proc. IMechE Part A: J. Power Energy*, 231, pp. 103-117, 2017.

[151] G. Dimitriadis, J. D. Gardiner, and P. G. Tickle, J. Codd, R. L. Nudds, Experimental and numerical study of the flight of geese, *Aeronaut. J.*, 119, pp. 1-30, 2015.

[152] W. P. Rodden, E. Dean Bellinger, Aerodynamic lag functions, divergence, and the british flutter method, *J. Aircr.*, 19, pp. 596–598, 1982.

[153] K. L. Roger, Airplane math modelling methods for active control design, AGARD, Report AGARD-CP-228, 1977.

[154] A. L. Cauchy, Exercices de Mathematiques (1828), Kessinger Publishing, 2010.

[155] S. D. Poisson, Mémoire sur l'équilibre et le Mouvement des Corps élastiques, Mémoires de l'Académie Royal des Sciences de l'Institut de France, 8, pp. 357-570, 1829.

[156] G. Kirchoff, Über das Gleichgewicht and die Bewegung einer elastischen Scheibe, Journal für reine und angewandte Mathematik, 40, pp. 51-88, 1850.

[157] H. N. Chu, G. Herrmann, Influence of large amplitude on free flexural vibrations of rectangular elastic plates, *Journal of Applied Mechanics and Technical Physics*, 41(12), pp. 532-540, 1956.

[158] Y. Weiliang, E. H. Dowell, Limit cycle oscillation of a fluttering cantilever plate, *AIAA Journal*, 29(11), 1991.

[159] D. Tang, E. H. Dowell, K. C. Hall, Limit cycle oscillations of a cantilevered wing in low subsonic flow, *AIAA Journal*, 37(3), pp. 364-371, 1999.

[160] D. Tang, J. K. Henry, E. H. Dowell, Limit cycle oscillations of delta wing models in low subsonic flow, *AIAA Journal*, 37(3), pp. 1355–1362, 1999.

[161] P. J. Attar, Cantilevered plate Rayleigh-Ritz trial function selection for Von Kármán's plate equations, *Journal of Aircraft*, 44(2), pp. 654–661, 2007.

[162] P. J. Attar, E. H. Dowell, D. Tang, A theoretical and experimental investigation of the effects of a steady angle of attack on the nonlinear flutter of a delta wing plate model, *Journal of Fluids and Structures*, 17(2), pp. 243-259, 2003.

[163] D. Tang, E. H. Dowell, Effects of angle of attack on nonlinear flutter of a delta wing, *AIAA Journal*, 39(1), pp. 15-21, 2001.

[164] B. Korbahti, E. Kagambage, T. Andrianne, et al., Subcritical, nontypical and period-doubling bifurcations of a delta wing in a low speed wind tunnel, *Journal of Fluids and Structures*, 27(3), pp. 408-426, 2011.

[165] V. V. Novozhilov, *Foundations of the Nonlinear Theory of Elasticity*. Rochester, NY: Graylock Press, 1953.

[166] K. McHugh, E. H. Dowell, Equations of Motion for an Inextensible Beam Undergoing Large Deflections, *Journal of Applied Mechanics*, 83(5), 061009, 2016.

[167] S. S. Rao, *Mechanical Vibrations*. 4th edn. Pearson Prentice Hall, International Edition, 2004.

[168] R. J. S. Simpson, R. Palacios, J. Murua Induced-drag calculations in the unsteady vortex lattice method, *AIAA Journal*, 51(7), 2013.